Università degli Studi di Ferrara

DOTTORATO DI RICERCA IN SCIENZE CHIMICHE

COORDINATORE PROF. GASTONE GILLI

MULTIREFERENCE PERTURBATION THEORIES FOR THE ACCURATE CALCULATION OF ENERGY AND MOLECULAR PROPERTIES

DOTTORANDO
DOTT. MARIACHIARA PASTORE

TUTORE
PROF. RENZO CIMIRAGLIA

XX° CICLO

ANNI 2006 - 2008

Con la certezza che ciò che è stato "costruito" in questi anni resterà anche dopo la fine di questa esperienza, vorrei ringraziare

il Professor Renzo Cimiraglia, supervisore attento e presente della mia attività di ricerca. Lo ringrazio per la stima e la fiducia che ho sempre percepito e per avermi dato tutti gli strumenti, le opportunità e l'autonomia per crescere, non solo preofessionalmente

Celestino, per essere stato un amico, prima ancora che uno dei miei punti di riferimento professionali

Maurizio perchè fortunatamente va a dormire sempre tardi

Stefano Evangelisti, Jean-Paul Malrieu, tutte le persone con cui ho lavorato e il *cassoulet* per aver reso indimenticabili i miei soggiorni a Toulouse

Sasha, per tutto il lavoro fatto insieme e per quella birra in quella squallida birreria della periferia di Stoccarda

Un grazie, poi, ai miei genitori e a mio fratello, per il loro costante supporto

Ringrazio Massimo per essermi accanto nei momenti complicati e nelle scelte importanti e per essere una fonte inesauribile di entusiasmo e di energia

Grazie, infine, ad i miei amici più cari. Grazie ad Eva, Martina, Silvia, Letizia, Ludovico e Roberto.

Contents

Preface

Quantum Chemistry has become an important and powerful tool to investigate a great deal of chemical and physical phenomena. Nowadays, the rapid growth of the computational power along with the corresponding development of methodologies, tailored to approach large scale systems, allows to treat problems of increasing size and complexity.

A large domain of application of rigorous quantum mechanics calculations is the accurate prediction of excitation energies and other spectroscopic parameters valuable for the interpretation of the experimental measurements. The description of electronically excited states represents a severe task for approximated theoretical approaches, even in the case of small-sized molecules. In such cases, the simple one-determinant approximation (the well-known Hartree-Fock theory) turn out to be defective and a multireference wavefunction, accounting for all the relevant electronic configurations, should be used. An important field of applications of the Multireference Perturbation Theories (MRPTs) is just the calculation of the electronically excited states of molecules, where the strong differential correlation effects and the possible multireference nature of the wavefunctions can be, in principle, successfully handled by a "variational plus perturbation" scheme.

This Ph.D. thesis deals with the development and the applications of N-Electron Valence State Perturbation Theory (NEVPT), a novel form of MRPT put forward in collaboration between the theoretical chemistry groups of the universities of Ferrara and Toulouse.

After a first general overview on the basic mathematical tools and theoretical methods (Chap. 1), in Chapter 2 we will introduce the NEVPT philosophy and present the major development effort accomplished during the Ph.D: the implementation of the third order correction to the energy in the so called "partially contracted" scheme. Then, the large part devoted to the applications follows. Part I concerns the calculation of electronically excited states. Different issues will be addressed: on the one hand the treatment of small aromatic molecules, Pyrrole, Furan and Thiophene (Chap. 3), whose description is complicated by the possible interaction with

low-lying Rydberg states and by the ionic nature of some valence states, extremely sensitive to the so-called dynamical $\sigma - \pi$ polarization; on the other hand the case of a large-sized aromatic molecule, Free-Base Porphin (Chap. 4), for which the crucial problem is the choice of a balanced variational space to accurately describe the wavefunctions of the ground and of the excited states. Finally, Chap. 5 is devoted to the description, by means of MRPT, of the Electron Transfer (ET) process in Mixed-Valence systems. The investigation is carried out on a model spiro $\pi - \sigma - \pi$ compound, for which the ET reaction is simulated using a simplified one-mode two-state model. The inadequacy of a standard second order MRPT approach will be shown and the application of an alternative and effective computational strategy will be discussed.

Chapter 1

Mathematical tools and methods

1.1 Complete set expansions

Let $f(x)$ be a function defined in the interval (a, b) and let $\Phi = \{\phi_1, \phi_2, \ldots, \phi_n\}$ be a set of functions defined in the same interval. One can express the function $f(x)$ as a linear combination, with properly chosen coefficients, of ϕ_i

$$f(x) \simeq f_n(x) = \sum_{i=1}^{n} c_i \phi_i \tag{1.1}$$

where the coefficients c_i are determined through minimization of the mean-square deviation of $f_n(x)$ from $f(x)$. The accuracy of such expansion depends on the completeness of the set of basis functions and at the limit of an infinite set ($n \to \infty$) we have $f_n(x) \to f(x)$.

It is possible to generalize these considerations to functions of several variables. To this purpose we consider the case of a wavefunction depending on the coordinates of n electrons $\Psi_{el}(x_1, x_2, \ldots, x_n)$. Given a complete set of one-electron spin-orbitals, $\{\psi_1, \psi_2, \ldots, \psi_n \ldots\}$, if the coordinates of $n-1$ electrons are considered fixed, the resulting function can be expanded in the form

$$\Psi_{el}(x_1, x_2, ..., x_n) = \sum_{i=1}^{+\infty} c_i(x_2, x_3, ..., x_n)\psi_i(x_1) \tag{1.2}$$

where the coefficients c_i, being actually functions themselves, hold the dependence on the coordinates of the remaining $n-1$ electrons.

Again, considering fixed $x_3, x_4, \ldots, x_n$, the coefficients c_i, which are now functions of a single variable, x_2, can be expanded on the same basis of spin-orbitals as

$$c_i = \sum_{j=1}^{+\infty} d_j \psi_j(x_2) \tag{1.3}$$

Repeating such procedure for the coordinates of the remaining $n-2$ electrons, one can have the exact expansion of the electronic wavefunction over the given set of spin-orbitals:

$$\Psi_{el}(x_1, x_2, \ldots, x_n) = \sum_{i,j,\ldots,p} c_{i,j\ldots,p}\psi_i(x_1)\psi_j(x_2)\ldots\psi_p(x_n), \tag{1.4}$$

where the indices $i, j, \ldots, p$ run over all possible choices of the spin-orbitals belonging to the basis set.

1.2 Antisymmetry: Slater's formalism

As above stated, equation (1.4) gives the exact expansion of a many-particle wavefunction over a complete set of monoelectronic spin-orbitals; however, a natural law imposes a severe restriction to a fermionic wavefunction: the *antisymmetry property*. In other terms, for a n-electron wavefunction $\Psi_{el}(x_1, x_2, \ldots, x_n)$ the following relationship must be satisfied:

$$P\Psi_{el}(x_1, x_2, \ldots, x_n) = \sigma_P\Psi_{el}(x_1, x_2, \ldots, x_n) \tag{1.5}$$

where P performs any permutation of the spin-coordinates $x_1, x_2, \ldots, x_n$ and σ_P equals ± 1 according as the permutation is given by an even or odd number of transpositions.

To overcome the difficulties of building an antisymmetric many-electron wavefunction, a possible strategy is to perform an expansion over a set of *antisymmetrized spin-orbital products*, the Slater determinants:

$$\Psi_{el}(x_1, x_2, \ldots, x_n) = \sum_I C_I\Phi_I \tag{1.6}$$

with

$$\Phi_I = \frac{1}{\sqrt{n!}}\begin{vmatrix} \psi_{i_1}(1) & \psi_{i_2}(1) & \cdots & \psi_{i_n}(1) \\ \psi_{i_1}(2) & \psi_{i_2}(2) & \cdots & \psi_{i_n}(2) \\ \vdots & \vdots & \vdots & \vdots \\ \psi_{i_1}(n) & \psi_{i_2}(n) & \cdots & \psi_{i_n}(n) \end{vmatrix} = \frac{1}{\sqrt{n!}}\mathrm{det}\,|\psi_{i_1}(1)\psi_{i_2}(2)\ldots\psi_{i_n}(n)| \tag{1.7}$$

Here the basis set has been chosen as *orthonormal* ($\langle\psi_i|\psi_j\rangle = \delta_{ij}$) and, consequently, the resulting set of Slater determinants turns out to be *orthogonal* ($\langle\Phi_K|\Phi_L\rangle = 0$ for $K \neq L$).

The use of Slater determinants automatically guarantees the antisymmetry of the wavefunction, since the sign of the determinant of the matrix (1.7) changes upon swapping of two columns (permutation of the spin-coordinates of two electrons).

Furthermore, in the case of a one-determinant approximation to the wavefunction, the quantum-mechanical form of the Pauli's principle directly follows, since the determinant in eq. (1.7) vanishes when two columns have the same value (two identical spin-orbitals).

1.2.1 Configuration Interaction Approach

Within the *Born-Oppenheimer* approximation (*fixed nuclei model*), in which the electronic and nuclear motions can be decoupled and two separate equations can be solved, the electronic *time-independent* Schrödinger equation has the form

$$\hat{\mathcal{H}}_{el}\Psi_{el}(X;Q) = E_{el}(Q)\Psi_{el}(X;Q) \tag{1.8}$$

where the electronic wavefunction posseses a parametric dependence on the nuclear coordinates Q. Substitution of (1.6) in equation (1.8) gives:

$$\sum_I \hat{\mathcal{H}}_{el}\Phi_I c_I = E_{el}\sum_I \Phi_I c_I \tag{1.9}$$

By application of the "bra" vector $\langle\Phi_J|$ to both sides of equation (1.6) one has

$$\sum_I \langle\Phi_J|\,\hat{\mathcal{H}}_{el}\,|\Phi_I\rangle\, c_I = E_{el}c_J \tag{1.10}$$

which can be put in matrix form

$$\mathbf{Hc} = E\mathbf{c} \tag{1.11}$$

where the matrix $\mathbf{H}$ has elements $H_{JI} = \langle\Phi_J|\,\hat{\mathcal{H}}_{el}\,|\Phi_I\rangle$ and the coefficients c_J have been collected in the column vector $\mathbf{c}$.
We note that the problem of solving the electronic Scrhödinger equation has been reduced to a purely algebraic problem of diagonalizing the Hamiltonian matrix $\mathbf{H}$.

Expression (1.11) is known as the full *Configuration Interaction* (FCI) expansion and provides the exact solution to the electronic Scrhödinger equation within a given one-electron basis set. The number of determinants in a FCI expansion, obtained distributing n electrons into N orbitals, is given by

$$\begin{pmatrix} N \\ n \end{pmatrix} = \frac{N!}{n!(N-n)!} \tag{1.12}$$

This factorial dependence of the number of Slater determinants on the number of spin-orbitals and electrons makes the FCI approach practically applicable only to very small molecular systems [1,2]. However, in those cases in which FCI calculations can be carried out, the results serve as useful benchmarks for evaluating the accuracy of other theoretical methods.

Slater's rules

Here, resorting to the well-known Slater's rules for one- and two-electron operators, we shall illustrate a fast way to evaluate the Hamiltonian matrix elements H_{JI}.

Given a one-electron operator $\hat{F} = \sum_{i=1}^{n} \hat{f}(i)$, only two cases in which the matrix elements give a non zero result are possible:

- if the two determinants are identical, $\Phi_J = \Phi_I$, one has

$$H_{II} = \sum_{j=1}^{n} \langle \psi_{i_j} | \hat{f} | \psi_{i_j} \rangle \tag{1.13}$$

- if the two determinants have a single spin-orbital difference ($\Phi_J \neq \Phi_I$, with $\psi_{j_k} \neq \psi_{i_k}$) the result is

$$H_{JI} = \langle \psi_{j_k} | \hat{f} | \psi_{i_k} \rangle \tag{1.14}$$

Clearly, all the matrix elements between Slater determinants differing for more than one spin-orbital are zero. In a similar way, for a two-electron operator

$$\hat{G} = \frac{1}{2} \sum_{i \neq j}^{n} \hat{g}(i,j) \tag{1.15}$$

the following three possibilities occur:

- if $\Phi_J = \Phi_I$ one has

$$G_{II} = \frac{1}{2} \sum_{k,l=1}^{n} \left(\langle \psi_{i_k} \psi_{i_l} | \hat{g} | \psi_{i_k} \psi_{i_l} \rangle - \langle \psi_{i_k} \psi_{i_l} | \hat{g} | \psi_{i_l} \psi_{i_k} \rangle \right) \tag{1.16}$$

- if $\Phi_J \neq \Phi_I$ for a single spin-orbital difference ($\psi_{j_k} \neq \psi_{i_k}$)

$$G_{JI} = \sum_{l=1}^{n} \left(\langle \psi_{j_k} \psi_{i_l} | \hat{g} | \psi_{i_k} \psi_{i_l} \rangle - \langle \psi_{i_k} \psi_{i_l} | \hat{g} | \psi_{i_l} \psi_{i_k} \rangle \right) \tag{1.17}$$

- if $\Phi_J \neq \Phi_I$ for two spin-orbital differences ($\psi_{j_k} \neq \psi_{i_k}$ and $\psi_{j_l} \neq \psi_{i_l}$)

$$G_{JI} = \langle \psi_{j_k} \psi_{j_l} | \hat{g} | \psi_{i_k} \psi_{i_l} \rangle - \langle \psi_{j_k} \psi_{j_l} | \hat{g} | \psi_{i_l} \psi_{i_k} \rangle \tag{1.18}$$

We should stress that in the above expressions we have implicitly assumed that the equal spin-orbitals appear in the same order in the two determinants; if, instead, the order is different, the possible change in sign due to the permutations must be taken into account.

1.3 An alternative approach: second quantization

1.3.1 The Fock space

The formalism we present in this section is known as *second quantization*; it was first developed in physics (field theory) and later widely used also in quantum chemistry (see Ref. [3]).

In the second quantization language there is a one-to-one correspondence between the electronic wavefunction $\Psi_{el}(x_1, x_2, \ldots, x_n)$, in which the spin-orbitals $\psi_i, \psi_j, \ldots, \psi_p$ are occupied by electrons and a *state vector (ket)* $|\mathbf{k}\rangle$, where only the *occupation numbers* (0 or 1) of the whole set of spin-orbitals are given, that is

$$|\mathbf{k}\rangle = |k_1, k_2, \ldots, k_N\rangle\,, k_i = \begin{cases} 1 & \text{if } \psi_i \text{ is occupied} \\ 0 & \text{if } \psi_i \text{ is unoccupied.} \end{cases} \tag{1.19}$$

The linear vector space spanned by basis vectors including all possible kets (1.19), obtained distributing n electrons in N spin-orbitals, is known as the *Fock Space*. Thereby, each Slater determinant has its corresponding *occupation number* vector in the Fock space and *vice versa*:

$$|ij\ldots p\rangle = \frac{1}{\sqrt{n!}} \begin{vmatrix} \psi_i(x_1) & \psi_j(x_1) & \ldots & \psi_p(x_1) \\ \psi_i(x_2) & \psi_j(x_2) & \ldots & \psi_p(x_2) \\ \vdots & \vdots & \vdots & \vdots \\ \psi_i(x_n) & \psi_j(x_n) & \ldots & \psi_p(x_n) \end{vmatrix}$$

Due to the antisymmetry property, the order in which the spin-orbitals appear (the labels in the ket vectors) is important and one has

$$|ji\ldots p\rangle = \frac{1}{\sqrt{n!}} \begin{vmatrix} \psi_j(x_1) & \psi_i(x_1) & \ldots & \psi_p(x_1) \\ \psi_j(x_2) & \psi_i(x_2) & \ldots & \psi_p(x_2) \\ \vdots & \vdots & \vdots & \vdots \\ \psi_j(x_n) & \psi_i(x_n) & \ldots & \psi_p(x_n) \end{vmatrix} = -\,|ij\ldots p\rangle$$

therefore, each vector is multiplied by σ_P $(= \pm 1)$ under label permutation.
A particular vector of the Fock space is the "*vacuum*" vector, representing the situation in which no particles are present

$$|vac\rangle = |0_1, 0_2, \ldots, 0_N\rangle\,. \tag{1.20}$$

1.3.2 Creation and annihilation operators

In order to connect vectors with different number of electrons, we define two operators, called *creation* and *annihilation* operators. The creation operator, a_r^+, is such

that

$$a_r^+ |ij\dots p\rangle = \begin{cases} |rij\dots p\rangle & \text{if } r \notin (ij\dots p) \\ 0 & \text{if } r \in (ij\dots p). \end{cases} \tag{1.21}$$

Therefore, if the ket does not include the occupation number of the spin-orbital ψ_r then a particle is added and an $(n+1)$-electron wavefunction is obtained, $\Phi(x_1, x_2, \dots, x_n, x_{n+1})$; otherwise, if r is already occupied in the associate Slater determinant, upon application of a_r^+ it vanishes, as a consequence of the antisymmetry requirement (two identical columns).

Similarly, one may define the annihilation operator, a_r, such that

$$a_r |rij\dots p\rangle = \begin{cases} |ij\dots p\rangle & \text{if } r \in (ij\dots p) \\ 0 & \text{if } r \notin (ij\dots p). \end{cases} \tag{1.22}$$

where the second case expresses the impossibility of annihilating an electron in a unoccupied spin-orbital.

Concluding, we note that all state vectors can be generated by application of the proper "string" of creation operators to the vacuum state

$$a_i^+ a_j^+ \dots a_p^+ |vac\rangle = |ij\dots p\rangle$$

and that the antisymmetry property of the basis vectors is ensured by the anticommutative properties of these operators:

$$\boxed{\begin{aligned} a_i^+ a_j^+ + a_i^+ a_j^+ = \left[a_i^+, a_j^+\right]_+ &= 0 \\ a_i a_j + a_i a_j = \left[a_i, a_j\right]_+ &= 0 \\ a_i a_j^+ + a_j^+ a_i = \left[a_i, a_j^+\right]_+ &= \delta_{ij} \end{aligned}}$$

1.3.3 Representation of one- and two-electron operators

The form of a one-electron operator in *first quantization* is

$$\hat{F}^{fq} = \sum_{i=1}^{n} f(i) \tag{1.23}$$

where the sum runs over the number of electrons n of the system. Recalling Slater's rules, illustrated in section (1.2.1), this operator gives null matrix elements when the Slater determinants differ for more than one spin-orbital. The *second quantization* analogue of (1.23) can be expressed as a linear combination of products of creation and annihilation operators:

$$\hat{F}^{sq} = \sum_{r,s} f_{rs} a_r^+ a_s, \tag{1.24}$$

where the indices r and s run over the whole set of spin-orbitals and the the matrix $\mathbf{F}$ is hermitian with $f_{rs} = f^*_{sr}$. As can be easly proved (see for instance Ref. [4]), by comparison with Slater's rules for a one-electron operator (section 1.2.1), choosing

$$f_{rs} = \int \psi^*_r(x_i)\hat{f}(x_i)\psi_s(x_i)dx_i \tag{1.25}$$

the first quantization one-electron operator $\hat{F}$ in (1.23) is equivalent to the second quantization form in (1.24).

We shall now consider the case of a two-electron operator, such as, for instance, the interelectronic repulsion term of the electronic Hamiltonian; as known, in first quantization it is expressed as

$$\hat{G}^{fq} = \frac{1}{2}\sum_{i,j}^{n}{}' g(x_i, x_j). \tag{1.26}$$

We recall that for a two-electron operator the matrix elements between two Slater determinants are non zero only if the determinants contain at least two electrons and if they do not differ by more than two spin-orbitals.
Analogously, in second quantization a two-electron operator has the following form:

$$\hat{G}^{sq} = \frac{1}{2}\sum_{rstu} g_{rs,tu} a^+_r a^+_s a_u a_t \tag{1.27}$$

where the matrix $\mathbf{G}$ is hermitian ($g_{rs,tu} = g^*_{tu,rs}$) and the symmetry property $g_{rs,tu} = g_{sr,ut}$ is imposed.

One can easly demonstrate that the first (1.26) and second quantization (1.27) forms become identical if the parameter $g_{rs,tu}$ are properly chosen as

$$g_{rs,tu} = \int\int \psi^*_r(x_1)\psi^*_s(x_2)g(x_1,x_2)\psi_t(x_1)\psi_u(x_2)dx_1dx_2 \tag{1.28}$$

Making use of the above presented results for generic two- and one-electron operators, we may now get the second quantization representation of the electronic Hamiltonian within the Born-Oppenheimer approximation:

$$\hat{H}_{el} = \sum_{r,s} \langle\psi_r|\, h\, |\psi_s\rangle\, a^+_r a_s + \frac{1}{2}\sum_{rstu} \left\langle \psi_r\psi_s \left| \frac{1}{r_{12}} \right| \psi_t\psi_u \right\rangle a^+_r a^+_s a_u a_t \tag{1.29}$$

Concluding, it is worthwhile summarizing the relevant characteristics of operators in first and second quantization formalisms. The first important difference between the two representations concerns the dependence on the number of electrons: whereas the first quantization operators (1.23) and (1.26) make explicit reference to the number of electrons, their second quantization analogues (1.24) and (1.27) do not have such dependence. Furthermore, the two languages have dissimilar ways of incorporating

the basis set dependence. In particular, in first quantization the determinants depend on the spin-orbital basis, while the operators are invariant with respect to the choice of the basis. On the contrary, in the second quantization representation, the state vectors do not have any reference to the spin-orbitals and this information is, instead, contained in the operators through the f_{rs} (1.25) and $g_{rs,tu}$ (1.28) parameters.

1.3.4 The spin-traced replacement operators

A useful simplification in the evaluation of the matrix elements of one- and two electron operators can be obtained through the definition of so-called spin-free operators. Given a set of spin-orbitals $(\psi_i, \psi_j, \ldots \psi_p)$, originated from the same set of spatial orbitals $(\phi_i, \phi_j \ldots \phi_p)$ with α and β occupations, for a spinless one-electron operators one has

$$\hat{F} = \sum_{rs} \langle \phi_r | \, t \, | \phi_s \rangle \, (a^+_{r\alpha} a_{s\alpha} + a^+_{r\beta} a_{s\beta}) \tag{1.30}$$

were we note that the summation runs just over the spatial orbitals. The spin-traced replacement operator is defined as

$$E_{rs} = a^+_{r\alpha} a_{s\alpha} + a^+_{r\beta} a_{s\beta} \tag{1.31}$$

The commutation rule for two spin-traced operators is

$$[E_{rs}, E_{tu}] = \delta_{st} E_{ru} - \delta_{ru} E_{ts} \tag{1.32}$$

and an important property of such operators is that they commute with the total spin momentum S^2 and with its z component, S_z.

Following the above schemae one arrives at the definition of a spinless two-electron operator:

$$\hat{G} = \frac{1}{2} \sum_{rstu} \langle \phi_r \phi_s | \, g \, | \phi_t \phi_u \rangle \, (E_{rs} E_{tu} - \delta_{ts} E_{ru}). \tag{1.33}$$

So, finally, using expressions (1.30), (1.31) and (**??**), the electronic Hamiltonian can be written as

$$\hat{H} = \sum_{rs} h_{rs} E_{rs} + \frac{1}{2} \sum_{rstu} \left\langle \phi_r \phi_s \left| \frac{1}{r_{12}} \right| \phi_t \phi_u \right\rangle (E_{rs} E_{tu} - \delta_{ts} E_{ru}). \tag{1.34}$$

1.4 One-determinant approximation: Hartree-Fock theory

Among the simplest approximations to the electronic wavefunction, one can quote the Hartree-Fock theory, where only one Slater determinant

$$\Psi(x_1, x_2, ..., x_n) = \|\psi_1 \psi_2 ... \psi_n\| \tag{1.35}$$

is considered and where the spin-orbitals ψ_i are optimized by minimizing the expectation value of the electronic energy $\left\langle \Psi \left| \hat{H} \right| \Psi \right\rangle$. The Hartree-Fock method can be applied to the description of the ground state as well as to that of the lowest-energy state of any given spatial or spin symmetry. This simple and apparently rough approximation is, however, able to provide, particularly in closed shell systems near their equilibrium geometry, electronic energies that are in error by less than 1%, and a number of molecular properties (dipole moments, force constants etc...) with a reasonable accuracy. Due to its low computational cost, the Hartree-Fock method is routinely used for qualitative studies of large molecular systems. For accurate quantitative studies, instead, the Hartree-Fock wavefunction represents the starting point for more sophisticated approaches, like the perturbative Møller-Plesset (MP) corrections and the coupled-cluster (CC) method ([4], [5]).

1.4.1 Self-Consistent Field (SCF) theory

Given the one-determinant expansion of the electronic wavefunction

$$\Psi(x_1, x_2, \ldots, x_n) = (n)^{-1/2} \mathrm{d}et|\psi_1 \psi_2 \ldots \psi_n| \tag{1.36}$$

the central point of the Hartee-Fock theory is to find the "best" spin-orbitals $(\psi_1, \psi_2, \ldots, \psi_n)$ to use in the Slater determinant. As is well-known, these optimal spin-orbitals are the eigenfunctions of a one-electron eigenvalue equation

$$\hat{F}\psi = \epsilon\psi \tag{1.37}$$

where $\hat{F}$, termed the *Fock operator*, is an operator of a single electron which takes account of an "effective field" due to the presence of the nuclei and of the remaining $n-1$ electrons. The Hartee-Fock method is a particular form of the independent-particle model (IPM), where the electronic interactions are evaluated by means of an "effective potential" through the Fock operator and the wavefunction is expressed as an antisymmetric product of one-electron functions.

In order to obtain equation (1.37), we start expressing the variational energy approximation of the one-determinant wavefunction (1.36)

$$E = \left\langle \Psi \left| \hat{H} \right| \Psi \right\rangle = \sum_i^n \langle \psi_i \left| h \right| \psi_i \rangle + \frac{1}{2} \sum_{i,j}^n \langle \psi_i \psi_j \left|\right| \psi_i \psi_j \rangle \tag{1.38}$$

where we have used a shorter notation, indicating

$$\langle \psi_i \psi_j \left|\right| \psi_i \psi_j \rangle = \langle \psi_i \psi_j \left| g \right| \psi_i \psi_j \rangle - \langle \psi_i \psi_j \left| g \right| \psi_j \psi_i \rangle \tag{1.39}$$

Let we choose an orthonormalized set of spin orbitals, such that $\langle \psi_i \left| \psi_j \right| = \rangle \delta_{ij}$. At the stationary point, for any infinitesimal variation $\psi_i = \psi_i + \delta\psi_i$ the condition

$\delta E = 0$ must be fulfilled. Such an infinitesimal variation of the spin orbital basis can be obtained applying the unitary operator $\hat{U} = e^{\hat{T}}$ to the wavefunction Ψ , where $\hat{T}$ is an antihermitian operator, that in second quantization can be expressed as

$$\hat{T} = -\hat{T}^{+} = \sum_{r,s} t_{rs} a_r^{+} a_s \tag{1.40}$$

with $t_{rs} = -t_{sr}$.

Upon opportune manipulations, one arrives at

$$\delta E = \sum_{i=1}^{n} \sum_{a>n} t_{ai} \langle \Psi | \hat{\mathcal{H}} | \Psi_i^a \rangle + c.c. \tag{1.41}$$

where "c.c." indicates the complex coniugate of the first term and the convention of indicating with indices $i, j \ldots$ the occupied spin-orbitals and with $a, b, \ldots$ the virtual ones has been adopted The relation $t_{ai} = -t_{ia}^{*}$ has been used and we also have introduced the shorter notation $|\Psi_i^a\rangle$ to indicate the Slater determinant in which the spin-orbital ψ_i has been replaced by ψ_a.

Equation 1.41 directly leads to the well-known form of the *Brillouin Theorem* [6,7]

$$\langle \Psi_i^a | \hat{\mathcal{H}} | \Psi \rangle = 0 \tag{1.42}$$

which states that the "best" spin-orbitals to use are such that the interaction between Ψ and any singly excited determinant Ψ_i^a is zero.

Resorting to Slater's rules (section 1.2.1) and introducing two auxiliary operators, $\hat{J}$ (*Coulomb operator*)

$$\langle \psi_r | \hat{J} | \psi_s \rangle = \sum_{j=1}^{n} \langle \psi_r \psi_j | \frac{1}{r_{12}} | \psi_s \psi_j \rangle$$

and $\hat{K}$ (*Exchange operator*)

$$\langle \psi_r | \hat{K} | \psi_s \rangle = \sum_{j=1}^{n} \langle \psi_r \psi_j | \frac{1}{r_{12}} | \psi_j \psi_s \rangle$$

one can write the *generalized Hartree-Fock equations*

$$\hat{F} | \psi_i \rangle = \sum_{j=1}^{n} | \psi_j \rangle \epsilon_{ji} \tag{1.43}$$

where we have defined the *Fock operator* $\hat{F} = \hat{h} + \hat{J} - \hat{K}$ and $\epsilon_{ji} = \langle \psi_j | \hat{F} | \psi_i \rangle = \langle \psi_i | \hat{F} | \psi_j \rangle^{*}$.

We can exploit the hermiticity of ϵ, considering the unitary transormation $\mathbf{U}^{+} \epsilon \mathbf{U}$

which diagonalizes ϵ and noting that changing the spin-orbitals according to the transformation

$$\psi'_i = \sum_{j=1}^{n} \psi_j U_{ji}$$

the Fock operator remains invariant under such transformation. So from the generalized equations (1.43) one arrives at the *canonical Hartree-Fock equations*:

$$\hat{F}\psi'_i = \epsilon_i \psi'_i \tag{1.44}$$

We recall that, since $\hat{F}$ depends on its eigenfunctions ψ_i, eq. (1.44) cannot be solved in a single step. An iterative method must instead be used, starting from a guess of spin-orbitals, building an approximated $\hat{F}$, diagonalizing it and proceeding until convergence is reached (*self consistency*).

1.4.2 Koopmans' Theorem

The eigenvalues of the canonical Fock equations (1.44) are termed "orbital energies" and have a direct physical interpretation, since $-\epsilon_i$ represents a first approximation to the Ionization Potential (IP), namely the energy needed to remove an electron from the spin-orbital ψ_i. Analogously, $-\epsilon_r$ is a first approximation to the Electron Affinity (EA) of the neutral molecule. This result is known as Koopmans' Theorem [8] and an interesting discussion can be found in Ref. [9].

Let us consider the ionized system obtained by removing an electron from the spin-orbital ψ_i in the Hartree-Fock determinant Ψ. The energy of the $n-1$ determinant is

$$E_i^+ = \left\langle a_i\Psi \left| \hat{\mathcal{H}} \right| a_i\Psi \right\rangle = \left\langle \Psi \left| a_i^+ \hat{\mathcal{H}} a_i \right| \Psi \right\rangle \tag{1.45}$$

$$= E + \left\langle \Psi \left| [a_i^+, \hat{\mathcal{H}}] a_i \right| \Psi \right\rangle . \tag{1.46}$$

Equation (1.46) can be easily manipulated exploiting the commutation rules between creation and annihilation operators (see section 1.3.2) and one promptly arrives at the formulation of the Koopmans' Theorem for the ionization energy:

$$\left\langle \Psi \left| [a_i^+, \hat{\mathcal{H}}] a_i \right| \Psi \right\rangle = -h_{ii} - (J_{ii} - K_{ii}) = -\epsilon_i \tag{1.47}$$

An analogous expression can be derived for the Electron Affinity $E - E_k^- = -\epsilon_k$

This approximation is based on a simple model for the open-shell ionized system, where the ionic wavefunction is not allowed to relax upon the ionization process (*relaxation energy*) but it is instead built from the "frozen" MOs of the neutral molecule; as a consequence, too large IPs and too small EAs are attained. In addition to these orbital relaxation effects, the HF method also neglects the correlation energy; however, while for the IPs, the KT approximation yields reasonable results, due to a sort of cancellation of errors, for the EAs it generally fails.

1.5 The Electron correlation problem

1.5.1 Electron distribution: density functions and density matrices

In order to better discuss the problem of the electron correlation energy, which represents one of the central issues in the electronic structure theory, here, we shall introduce the concepts of *density functions* and *density matrices* [10–13]. The great advantage of using this functions basically arises from their relative simplicity, particularly when compared to the complexity of sophisticated wavefunctions, and from the prompt insight they give about the physical content of the electron distribution.

Let us consider a n-electron wavefunction $\Psi(x_1, x_2, \ldots, x_n)$, the probability of finding electron 1 in x_1 and at the same time electron 2 in x_2 etc. is given by

$$dP(x_1, x_1 + dx_1; \ldots; x_n, x_n + dx_n) = \Psi(x_1, x_2, \ldots, x_n)\Psi^*(x_1, x_2, \ldots, x_n)dx_1\ dx_2. \tag{1.48}$$

Then, the probability on any of n electron in dx_1 is expressed as

$$dP(x_1, x_1 + dx_1) = dx_1 \int \Psi(x_1, x_2, \ldots, x_n)\Psi^*(x_1, x_2, \ldots, x_n)\ dx_2\ dx_3 \ldots\ dx_n \tag{1.49}$$

By multiplying eq.(1.49) by the number of electrons, n, we obtain the amount of charge in volume dx_1. We write this probability as $\rho(x_1)dx_1$ where we have introduced the *density function* $\rho(x_1)$ defined as

$$\rho(x_1) = n \int \Psi(x_1, x_2, \ldots, x_n)\Psi^*(x_1, x_2, \ldots, x_n)dx_2 dx_3 \ldots dx_n \tag{1.50}$$

We should stress that x_1 on the left of eq. (1.50) does not indicate the coordinates of electron 1 but the "point 1" of the whole space in which the density is evaluated. By integration over the spin coordinates, it is then possible to obtain the probability of finding an electron at point 1 regardless of its spin:

$$P(r_1) = \int \rho(dx_1)ds_1. \tag{1.51}$$

Such definitions given for a single electron can be easily extended to two or more particles; so, in the case of two electrons, the *pair density function* becomes

$$\rho(x_1, x_2) = n(n-1) \int \Psi(x_1, x_2, \ldots, x_n)\Psi^*(x_1, x_2, \ldots, x_n)dx_3 dx_4 \ldots dx_n \tag{1.52}$$

and its spinless counterpart is

$$P(r_1, r_2) = \int \rho(x_1, x_2)ds_1 ds_2. \tag{1.53}$$

Let $\hat{F} = \sum_{i=1}^{n} f(x_i)$ be a one-electron multiplicative operator and $\Psi(x_1, x_2, \ldots, x_n)$ a n-electron wavefunction, the expectation value of $\hat{F}$ is

$$\begin{aligned} \langle F \rangle &= \sum_{i=1}^{n} \int \Psi^*(x_1, x_2, \ldots, x_n) f(x_i) \Psi(x_1, x_2, \ldots, x_n)\ dx_1\ dx_2 \ldots\ dx_n \\ &= n \int \Psi^*(x_1, x_2, \ldots, x_n) f(x_1) \Psi(x_1, x_2, \ldots, x_n)\ dx_1\ dx_2 \ldots\ dx_n. \end{aligned} \quad (1.54)$$

Since $f(x_1)$ is just a multiplier, expression (1.54) can be rearranged, using the definition of density function given in eq. (1.50), to obtain

$$\langle F \rangle = \int f(x_1) \rho(x_1)\ dx_1. \quad (1.55)$$

We note that in the more general case of non-multiplicative operator $f(x_1)$, eq. (1.54) cannot be simply put in the form (1.55), since $\Psi^*(x_1, x_2, \ldots, x_n)$ cannot be shifted to the right of the operator. However, a simple mathematical trick can be used: since $f(x_1)$ works only on functions of x_1, Ψ^* can be made exempt from the action of $f(x_1)$ just changing the name of the variable from x_1 to x_1'; then, upon the action of $f(x_1)$ on Ψ we can change back $x_1' \rightarrow x_1$ and proceed to the integration. Practically, the expectation value becomes

$$\langle F \rangle = \int_{x_1' = x_1} f(x_1) \rho(x_1, x_1')\ dx_1. \quad (1.56)$$

where the the *density matrix*

$$\rho(x_1; x_1') = n \int \Psi(x_1, x_2, \ldots, x_n) \Psi^*(x_1', x_2, \ldots, x_n)\ dx_2\ dx_3 \ldots\ dx_n \quad (1.57)$$

has been introduced.

For two-electron operators, the *two-particle density matrix* can be defined

$$\rho(x_1, x_2; x_1', x_2') = n(n-1) \int \Psi(x_1, x_2, \ldots, x_n) \Psi^*(x_1', x_2', \ldots, x_n)\ dx_3\ dx_4 \ldots\ dx_n \quad (1.58)$$

and hence the expectation value of a generic two-electron operator

$$\hat{G} = \frac{1}{2} \sum_{i \neq j = 1}^{n} \hat{g}(x_i, x_j)$$

can be obtained simply evaluating

$$\langle G \rangle = \frac{1}{2} \int_{\substack{x_1' = x_1 \\ x_2' = x_2}} \hat{g}(x_1, x_2)\ \rho(x_1, x_2; x_1', x_2')\ dx_1\ dx_2 \quad (1.59)$$

Integrating over the spin coordinates, the *spinless density matrices* analogous of the spinless density functions (1.51) and (1.53) are defined:

$$\rho(r_1; r_1') = \int\limits_{s_1'=s_1} \rho(x_1; x_1')\ ds_1 \tag{1.60}$$

and

$$\rho(r_1, r_1'; r_2, r_2') = \int\limits_{\substack{s_1'=s_1 \\ s_2'=s_2}} \rho(x_1, x_1'; x_2, x_2')\ ds_1\ ds_2 \tag{1.61}$$

Obviously, following the same formalism, density matrices for three or more particles can be defined.

Finally, it is worthwhile to point out that the density matrix $\rho(x_1; x_1')$ does not have an actual physical meaning in itself but only its diagonal part $\rho(x_1; x_1)$, which coincides with the density function $\rho(x_1)$.

Then, given a complete set of orthonormal basis functions $\{\psi_1, \psi_2, \ldots\}$, we may expand the one and two-particle density matrices in the forms

$$\rho(x_1; x_1') = \sum_{i,j} R_{ij} \psi_i(x_1) \psi_j^*(x_1') \tag{1.62}$$

and

$$\rho(x_1, x_2; x_1', x_2') = \sum_{i,j,k,l} R_{ij;kl} \psi_i(x_1) \psi_j(x_2) \psi_k^*(x_1') \psi_l^*(x_2') \tag{1.63}$$

where the coefficients R_{ij} and $R_{ij;kl}$ are numerical factors.
Finally, the expectation values of one- and two-electron operators can be evaluated respectively as

$$\hat{F} = \int\limits_{x_1'=x_1} \hat{f}(x_1) \rho(x_1; x_1')\ dx_1 = \sum_{i,j} R_{ij} F_{ji} \tag{1.64}$$

and

$$\hat{G} = \frac{1}{2} \int\limits_{\substack{x_1'=x_1 \\ x_2'=x_2}} \hat{g}(x_1, x_2) \rho(x_1, x_1'; x_2, x_2')\ dx_1\ dx_2 = \frac{1}{2} \sum_{i,j,k,l} R_{ij;kl} G_{kl;ij} \tag{1.65}$$

where the matrices $\mathbf{F}$ and $\mathbf{G}$ have elements

$$F_{ji} = \langle \psi_j \left| f(x_1) \right| \psi_i \rangle \tag{1.66}$$

and

$$G_{kl;ij} = \langle \psi_k \psi_l \left| g(x_1, x_2) \right| \psi_i \psi_j \rangle \tag{1.67}$$

1.5.2 The one-determinant approximation case

In the case of a one-determinant n-electron wavefunction

$$\Psi(x_1,\ldots,x_n) = \frac{1}{\sqrt{n!}}\|\psi_1\psi_2\ldots\psi_n\|$$

the forms of the one- and two-particle density matrices can be obtained comparing the above expressions (1.64) and (1.65) with the expectation value of the electronic Hamiltonian in Slater's formalism (see section 1.2.1)

$$\begin{aligned} E &= \left\langle \Psi \left| \hat{H} \right| \Psi \right\rangle \\ &= \sum_i \langle \psi_i \left| h \right| \psi_i \rangle + \frac{1}{2}\sum_{ij}(\langle \psi_i\psi_j \left| g \right| \psi_i\psi_j \rangle - \langle \psi_i\psi_j \left| g \right| \psi_j\psi_i \rangle) \end{aligned} \tag{1.68}$$

For the one-electron part of $\hat{H}$ we have that the following equality must be satisfied

$$R_{ij} = \delta_{ij} \rightarrow \rho(x_1;x_1') = \sum_{i=1}^{n} \psi_i(x_1)\psi_i^*(x_1') \tag{1.69}$$

with both i and j occupied; for the two-electron component, we obtain the relations

$$\begin{cases} R_{ij;ij} = 1 \\ R_{ij;ji} = -1 \\ R_{ii;ii} = 0 \end{cases}$$

again with i and j occupied and thus

$$\rho(x_1,x_2;x_1',x_2') = \sum_{i,j=1}^{n}(\psi_i(x_1)\psi_j(x_2)\psi_i^*(x_1')\psi_j^*(x_2') - \psi_i(x_1)\psi_j(x_2)\psi_j^*(x_1')\psi_i^*(x_2')). \tag{1.70}$$

An important result is that eq. (1.70) can be expressed in terms of one-electron density matrix

$$\rho(x_1,x_2;x_1',x_2') = \rho(x_1;x_1')\rho(x_2;x_2') - \rho(x_2;x_1')\rho(x_1;x_2') \tag{1.71}$$

and, more generally, for any n-electron density matrix it may be shown that

$$\rho_n(x_1,\ldots,x_n;x_1',\ldots,x_n') = \begin{vmatrix} \rho(x_1;x_1') & \rho(x_1;x_2') & \cdots & \rho(x_1;x_n') \\ \rho(x_2;x_1') & \rho(x_2;x_2') & \cdots & \rho(x_2;x_n') \\ \vdots & \vdots & \vdots & \vdots \\ \rho(x_n;x_1') & \rho(x_n;x_2') & \cdots & \rho(x_n;x_n') \end{vmatrix} \tag{1.72}$$

Recalling the definition given of the spinless density matrices (1.60, 1.61) and differentiating the spin-orbitals according to their spin factor, for a closed-shell determinant we can write

$$\begin{aligned}\rho(x_1;x_1') &= \sum_{i_\alpha=1}^{n/2}\phi_i(r_1)\phi_i^*(r_1')\alpha(s_1)\alpha^*(s_1') + \sum_{i_\beta=1}^{n/2}\phi_i(r_1)\phi_i^*(r_1')\beta(s_1)\beta^*(s_1') \\ &= P_1^{\alpha\alpha}\alpha(s_1)\alpha(s_1') + P_1^{\beta\beta}\beta(s_1)\beta(s_1') \qquad (1.73)\end{aligned}$$

and integrating over the spin we obtain the spinless density matrix

$$P_1(r_1;r_1') = P_1^{\alpha\alpha} + P_1^{\beta\beta} \qquad (1.74)$$

with $P_1^{\alpha\alpha} = P_1^{\beta\beta}$.

We now turn to the pair density matrix; as can be shown, for a wavefunction of definite spin, it consists of six components ($\alpha\alpha\alpha\alpha$, $\beta\beta\beta\beta$, $\alpha\beta\alpha\beta$, $\beta\alpha\beta\alpha$, $\alpha\beta\beta\alpha$ and $\beta\alpha\alpha\beta$), which reduce to four after integration over the spin

$$P_2(r_1,r_1';r_2,r_2') = P_2^{\alpha\alpha\alpha\alpha} + P_2^{\beta\beta\beta\beta} + P_2^{\alpha\beta\alpha\beta} + P_2^{\beta\alpha\beta\alpha} \qquad (1.75)$$

Recalling that in the one-determinant case the two-particle density matrix can be factorized in terms of the one-particle density matrices (1.71), the following expressions are obtained for the pair functions (imposing $r_1' = r_1$ and $r_2' = r_2$)

$$\begin{aligned}P_2^{\alpha\alpha}(r_1,r_2) &= P_1^{\alpha}(r_1)P_1^{\alpha}(r_2) - P_1^{\alpha}(r_1;r_2)P_1^{\alpha}(r_2;r_1) \qquad (1.76)\\ P_2^{\beta\beta}(r_1,r_2) &= P_1^{\beta}(r_1)P_1^{\beta}(r_2) - P_1^{\beta}(r_1;r_2)P_1^{\beta}(r_2;r_1) \qquad (1.77)\\ P_2^{\alpha\beta}(r_1,r_2) &= P_1^{\alpha}(r_1)P_1^{\beta}(r_2) \qquad (1.78)\\ P_2^{\beta\alpha}(r_1,r_2) &= P_1^{\beta}(r_1)P_1^{\alpha}(r_2) \qquad (1.79)\end{aligned}$$

From these expressions, indicating the probability of finding electrons simultaneously at two point in space with a given spin configuration, we can get a prompt understanding of the electron correlation problem. As is apparent, the motion of electrons with the same spin, $\alpha\alpha$ (2.5) or $\beta\beta$ (1.77), is described by *correlated* functions and $P_2^{\alpha\alpha}(r_1,r_2)$ vanishes as $r_2 \to r_1$. This type of correlation, known as *Fermi correlation*, avoids electrons of parallel spin being at the same point of space and directly arises from the antisymmetry property of a fermionic wavefunction. On the contrary, from eqs. (1.78) and (1.79), we see that there is *no correlation* between the motion of electrons with opposite spin, since the probability of finding them in r_1 and r_2 at the same time is given just by the product of the probabilities of the each of two independent events. This lack of correlation (*Coulomb correlation*) is clearly a serious defect in the one-determinant model, since the mutual repulsion between pairs of electrons is not properly taken into account and the probability of finding them close together does not decrease as the distance decreases.

1.5.3 Statical and Dynamical Correlation

From a "quantitative" point of view, the correlation energy is defined (Löwdin, 1955) as the difference between the "exact" energy (practically the energy of FCI wavefunction) and the energy of the Hartree-Fock wavefunction

$$E_{corr} = E_{exact} - E_{H-F}$$

within a given basis set approximation. Although in itself it represents a very small fraction of the electronic energy, its accurate treatment is essential when dealing with energy differences which are of the same order of magnitude of the correlation energy (chemical reactivity, excitation energies etc.).

Actually, two different effects of electronic correlation exist:

- the *statical correlation*, which is associated with the problems of the multiconfigurational character of the wavefunction;
- the *dynamical correlation*, which is, instead, related to the effects of the interelectronic interactions.

Referring the the Hartree-Fock description of the H_2 molecule dissociation, the distinction between the statical and the dynamical effects becomes clear. At the equilibrium geometry, the wavefunction is qualitatively well described by the closed-sell Hartree-Fock determinant and the correlation energy essentially arises from the dynamical effects of the interelectronic repulsions. On the other hand, at the dissociation limit, where there is no coulomb repulsion between the two electrons, the failure of the one-determinant approximation is due to the need to take into account the near-degeneracy between the σ_g^2 and σ_u^2 configurations.

1.6 Handling the Statical Correlation: MCSCF Theory

As above stated, in many chemical and physical phenomena, such as the rupture or formation of chemical bonds, or the description of electronically excited states, the one-determinant approximation dramatically fails due to the intrinsic multireference nature of the problem. These statical correlation effects can be properly taken into account resorting to a multideterminant expansion of the wavefunction, in which a simultaneous variational optimization of spin-orbitals and expansion coefficients is performed: such strategy is called *Multiconfigurational Self-Consistent Field* (MCSCF) approach.

Starting from a truncated CI expansion

$$\Psi = \sum_{K=1}^{N} C_K \Phi_K, \tag{1.80}$$

in order to build a MCSCF wavefunction we need to impose that the energy variation with respect to an infinitesimal variation of both orbitals ($\phi' = \phi + \delta\phi$) and coefficients ($C'_K = C_K + \delta C_K$) is zero.

The optimization can be performed resorting to both a single-step Newton-Rahpson technique and a two-step approach (*Super CI*), where first the coefficients C_K and then the orbitals are iteratively optimized until self-consistency is reached.

Following the procedure presented in section (1.4.1) for the Hartree-Fock theory, the self-consistency condition is here expressed as

$$\sum_{rs} t_{rs} \left(\langle \Psi | \hat{\mathcal{H}} | E_{rs} \Psi \rangle - \langle E_{sr} \Psi | \hat{\mathcal{H}} | \Psi \rangle \right) = 0 \tag{1.81}$$

and it is satisfied by the *Extended-Brillouin Theorem* [14]

$$\langle \Psi | \hat{\mathcal{H}} | (E_{rs} - E_{sr}) \Psi \rangle = 0 \tag{1.82}$$

In other terms, when the energy is stationary, the contracted single excitations $\Psi^r_s = (E_{rs} - E_{sr})\Psi$ do not interact with the optimized MCSCF wavefunction. The *Super CI* method is practically based upon an iterative procedure, which consists in building an improved wavefunction

$$\Psi' = \Psi + \sum_{r>s} c_{rs} \Psi^r_s \tag{1.83}$$

diagonalizing the CI matrix and then using the coefficients of the single-excited functions, c_{rs}, for constructing the matrix $\mathbf{T}$, which operates the unitary orbital transformation ($\mathbf{U} = e^{\mathbf{T}}$).

1.6.1 Complete Active Space (CAS)

The key issue in the construction of a reduced CI space in which to expand the MC wavefunction is essentially how to select a limited number of electronic configurations able to properly take into account the statical correlation energy effects. In the present work we shall adopt a particular and largely used type of MCSCF wavefunction, known as Complete Active Space Self-Consistent Field (CASSCF) wavefunction [15]. As we shall widely discuss in the next chapter, this function represents the zero order wavefunction, $\Psi^{(0)}$, in our perturbative approach.

The idea of *Active Space* provides a useful "precept" to choose the relevant configurations of the CI expansion (1.80). It is based upon the partitioning of the spin-orbitals into three classes:

1. **core** (i, j, ...), which have occupation number equal to 1 in all the determinants Φ_K;

2. **active** (a, b, ...), with all the possible occupation number from 0 to 1;

3. **virtual** (r, s, ...), which are never occupied in any determinant Φ_K.

The CASSCF wavefunction is built by performing a Full CI expansion within the active orbitals subspace and then optimizing coefficients and orbitals until self-consistency. However, it is important to stress that the CASSCF approach is not a "black-box" method and there is not a recipe to select the "right" active space. However, it should be always carefully chosen in order to include all the orbitals that are thought to be involved in some measure in the chemical and physical process under consideration.

Chapter 2

N-electron Valence State Perturbation Theory

Multireference perturbation theories (MRPT) represent a powerful and relatively inexpensive tool for the treatment of electronic correlation in molecules. As discussed in the previous chapter (section 1.5.3), in many molecular phenomena such as the breaking of a chemical bond or the electronic transition to an excited state, a single reference wavefunction does not suffice to provide a good approximation to the solution of the time independent Schrödinger equation; many electronic configurations can be important and a zero order description of the electronic structure of the molecule may not leave out of consideration such quasidegenerate configurations. The inclusion of the quasidegenerate configurations accounts for what is called the *statical correlation* (section 1.6); the *dynamical component* could be dealt with perturbationally with a suitable MRPT. A key issue in MRPT concerns the definition of a proper zero order Hamiltonian H_0. In the early theories, which were developed at the beginning of the 1970's, such as CIPSI [16], H_0 was defined in terms of a one–electron, Fock–like, operator and the zero order functions (*perturbers*), used to build the first order correction to the wavefunction, were simple Slater determinants. The idea that H_0 should be based on a one–electron operator still persists in most modern MRPT's. For instance in CASPT2 [17,18], one of the most successful forms of MRPT, H_0 is a projected generalized Fock operator and the perturbers are built in terms of internally contracted excitations (*vide infra*). Dyall [19] showed that the usage of correction functions deriving from a one–electron operator introduces a bias in the energy calculation since the zero order reference wavefunction properly takes into consideration the bielectronic interactions occurring among the active electrons whereas the correction functions are not allowed to do so. In order to obviate such difficulty Dyall proposed the use of a model Hamiltonian, partially bielectronic. In 2001, based on Dyall's work, the "n–electron valence state perturbation theory"

(NEVPT) [20–25] was developed, in collaboration between the theoretical chemistry groups of the universities of Ferrara and Toulouse. The chapter has the following structure: a brief résumé of the Rayleigh-Schrödinger Perturbation Theory (RSPT) and of the Møller-Plesset Theory will be proposed in section 2.1 and 2.2 respectively. Then we shall present the second order NEVPT approach in its single-state (section 2.3) and quasidegenerate (section 2.6) formulations; section 2.7 is instead devoted to the third order NEVPT and Internally Contracted CI method, whose "partially contracted" version implementation takes a central part in the present research work.

2.1 Rayleigh-Schrödinger Perturbation Theory

The basic idea of the perturbative methods is to express the true Hamiltonian $\hat{H}$ as the sum of an "unperturbed" Hamiltonian (*model Hamiltonian*), $\hat{H}_0$, and of a *perturbation operator*,$\hat{V}$,

$$\hat{H} = \hat{H}_0 + \lambda\hat{V} \tag{2.1}$$

where λ gives the extent of the perturbation. Supposing to be in a non-degenerate case, the eigenstates and the associated eigenvalues of the unperturbed Hamiltonian $\hat{H}_0$ are known

$$\hat{H}_0\Psi_n^0 = E_n^0\Psi_n^0 \quad n = 0, 1, 2, \ldots \tag{2.2}$$

Due to the effect of the perturbation, which is however supposed to be small, the eigenfunctions and the eigenvalues of $\hat{H}$ will change as a function of the parameter λ. In the Rayleigh-Schrödinger (RS) scheme, the energy and the wavefunction are expanded in Taylor's series to obtain

$$E_n = E_n^{(0)} + \lambda E_n^{(1)} + \lambda^2 E_n^{(2)} + \ldots \tag{2.3}$$

$$\Psi_n = \Psi_n^{(0)} + \lambda\Psi_n^{(1)} + \lambda^2\Psi_n^{(2)} + \ldots \tag{2.4}$$

To simplify the derivation, we suppose that the eigenstates of $\hat{H}_0$ are normalized ($\langle\Psi_n^{(0)}|\Psi_n^{(0)}\rangle = 1$); moreover, we also impose the *intermediate normalization* condition $\langle\Psi_n^0|\Psi_n\rangle = 1$. By substitution of expressions (2.3) and (2.4) into the Schrödinger equation $\hat{\mathcal{H}}\Psi_n = E_n\Psi_n$, we obtain

$$\begin{aligned} & \lambda^0(\hat{H}_0\Psi_n^{(0)} - E_n^{(0)}\Psi_n^{(0)}) \\ + \; & \lambda^1(\hat{H}_0\Psi_n^{(1)} + \hat{V}\Psi_n^{(0)} - E_n^{(0)}\Psi_n^{(1)} - E_n^{(1)}\Psi_n^{(0)}) \\ + \; & \lambda^2(\hat{H}_0\Psi_n^{(2)} + \hat{V}\Psi_n^{(1)} - E_n^{(0)}\Psi_n^{(2)} - E_n^{(1)}\Psi_n^{(1)} - E_n^{(2)}\Psi_n^{(0)}) \\ + \; & \ldots = 0 \end{aligned} \tag{2.5}$$

We see that eq. (2.5) is satisfied only if the terms inside parenthesis are zero, then the equations obtained for the different orders can be manipulated and one arrives

to the following expression for the generic contribution of k order correction to the energy:

$$E_n^{(k)} = \left\langle \Psi_n^{(0)} \right| \hat{V} \left| \Psi_n^{(k-1)} \right\rangle . \tag{2.6}$$

For the first and the second order one has

$$E_n^{(1)} = \left\langle \Psi_n^{(0)} \right| \hat{V} \left| \Psi_n^{(0)} \right\rangle \tag{2.7}$$

$$E_n^{(2)} = \left\langle \Psi_n^{(0)} \right| \hat{V} \left| \Psi_n^{(1)} \right\rangle \tag{2.8}$$

with $\Psi_n^{(1)}$ given by

$$\Psi_n^{(1)} = -R_n \hat{V} \Psi_n^{(0)} \tag{2.9}$$

where R_n (termed the "resolvent operator"), in absence of degeneracy of $\Psi_n^{(0)}$, has the form

$$R_n = \sum_{k \neq n} \frac{\left| \Psi_k^0 \right\rangle \left\langle \Psi_k^0 \right|}{E_k^0 - E_n^0} \tag{2.10}$$

Equation (2.9) can be substituted into eq. (2.8) to obtain:

$$E_0^{(2)} = -\sum_{k \neq 0} \frac{\left| \left\langle \Psi_n^{(0)} \right| \hat{V} \left| \Psi_k^{(0)} \right\rangle \right|^2}{E_k^{(0)} - E_n^{(0)}} \tag{2.11}$$

For the third order correction, instead, one has

$$E_n^{(3)} = \left\langle \Psi_n^{(0)} \right| \hat{V} \left| \Psi_n^{(2)} \right\rangle$$

which becomes

$$E_n^{(3)} = \left\langle \Psi_n^{(1)} \right| \hat{V} \left| \Psi_n^{(1)} \right\rangle + E_n^{(1)} \| \Psi_n^{(1)} \|^2 \tag{2.12}$$

2.2 Møller-Plesset Theory

In the Møller-Plesset theory [26] the model Hamiltonian is a n-particle operator, also called the *Fockian*, which in second quantization has the form:

$$\hat{\mathcal{F}} = \sum_r \epsilon_r a_r^+ a_r. \tag{2.13}$$

The perturbation operator, $\hat{V}$ (also termed *fluctuation* potential) is given by the difference

$$\hat{V} = \hat{H} - \hat{\mathcal{F}}. \tag{2.14}$$

The zero order wavefunction is the Hartree-Fock determinant $|\Psi_0\rangle$ built up with n spin-orbitals ψ_i, which are solutions of the canonical Hartree-Fock equations $\hat{f}\psi_i = \epsilon_i \psi_i$; the zero order energy is $E_0 = \sum_{i=1}^n \epsilon_i$.

However, we note that any other determinant $|\Psi_k\rangle$, built with n arbitrary spin-orbitals ψ_i, is an eigenfunction of $\hat{\mathcal{F}}$ with eigenvalue $E_k^{(0)} = \sum_{i=1}^{n} \epsilon_{k_i}$, thus the first and second order contribution to the energy are respectively

$$E_0^{(1)} = \langle \Psi_0 | \hat{\mathcal{H}} - \hat{\mathcal{F}} | \Psi_0 \rangle = E_0^{H-F} - \sum_{i=1}^{n} \epsilon_i \tag{2.15}$$

and

$$E_0^{(2)} = -\sum_{k \neq 0} \frac{\left| \langle \Psi_0 | \hat{\mathcal{H}} | \Psi_k \rangle \right|^2}{E_k^{(0)} - E_0^{(0)}} \tag{2.16}$$

As is evident from equation (2.15), the first order contribution (MP1) does not bring about any correction to the Hartree-Fock energy ($E_0^{(0)} + E_0^{(1)} = E_0^{H-F}$). Instead, for the second order correction (MP2), from eq. (2.16) comes that only the doubly-excited determinants will give a contribution, since the singly-excited determinants do not interact with the HF wavefunction as stated by Brillouin's theorem. Indicating with $\left| \Psi_{ij}^{ab} \right\rangle$ the determinant in which two occupied spin-orbitals (i, j) have been substituted by two virtual ones (a, b), eq. (2.16) becomes:

$$E_0^{(2)} = -\sum_{i<j}^{occ} \sum_{a<b}^{virt} \frac{|\langle \psi_a \psi_b | \, | \psi_i \psi_j \rangle|^2}{\epsilon_a + \epsilon_b - \epsilon_i - \epsilon_j} \tag{2.17}$$

2.3 NEVPT2 philosophy

Multireference perturbation theories can be classified, according to the strategy adopted to obtain the corrected energies and wavefunctions, into two categories:

- "*perturb then diagonalize*", where an effective Hamiltonian is perturbatively built in a model space and then diagonalized;
- "*diagonalize then perturb*", where the perturbation is performed upon a zero order wavefunction obtained by diagonalization of the Hamiltonian in a given determinant space.

As above mentioned, in the NEVPT approach, which belongs to the *diagonalize then perturb* methods, a CASSCF (or CASCI) reference wavefunction is employed and the zero order Hamiltonian is built by means of Dyall's Hamiltonian [19]

$$\hat{H}^D = \hat{H}_i + \hat{H}_v + C, \tag{2.18}$$

where $\hat{H}_i$ is a one–electron operator defined in terms of orbital energies and creation/destruction pairs

$$\hat{H}_i = \sum_{i}^{core} \epsilon_i E_{ii} + \sum_{r}^{virt} \epsilon_r E_{rr}, \tag{2.19}$$

H_v is a two–electron operator confined to the active orbital space

$$H_v = \sum_{ab}^{act} h_{ab}^{eff} E_{ab} + \frac{1}{2} \sum_{abcd}^{act} \langle ab|cd\rangle (E_{ac}E_{bd} - \delta_{bc}E_{ad}), \tag{2.20}$$

and C is a suitable constant assuring that $\hat{H}^D$ is equivalent to $\hat{H}$ within the CAS space ($C = 2\sum_i^{core} h_{ii} + \sum_{ij}^{core}(2\langle ij|ij\rangle - \langle ij|ji\rangle) - 2\sum_i^{core} \epsilon_i$.) The quantities h_{ab}^{eff} appearing in eq.(2.20) are the usual one–electron matrix elements h_{ab}, where the contribution deriving from the effective field of the core electrons ($h_{ab}^{eff} = h_{ab} + \sum_j^{core}(2\langle aj|bj\rangle - \langle aj|jb\rangle)$) is added. The energies of the core, ϵ_i, and virtual, ϵ_r, orbitals are usually chosen as those which result from the diagonalization of the generalized Fock matrix (*canonical orbitals*).

The zero order wave functions external to the CAS-CI space and differing from $\Psi_m^{(0)}$ for a well-defined pattern of the inactive orbitals are referred to as "perturber functions" (or "perturbers"). The perturbers are indicated as $\Psi_{l,\mu}^{(k)}$ and the space they belong to as $S_l^{(k)}$, where "l" is the occupation pattern of the inactive orbitals,"k" is the number of electrons promoted (removed) to (from) the active space and "μ" simply enumerates the various perturbers. There are only eight typologies of $S_l^{(k)}$ subspaces: $S_{ij,rs}^{(0)}$ with two core orbitals substituted by two virtuals, $S_{i,r}^{(0)}$ with one core orbital substituted by one virtual, $S_{ij,r}^{(+1)}$ with one core substituted by one virtual and one core electron added to the active space, $S_i^{(+1)}$ with one core electron added to the active space, $S_{i,rs}^{(-1)}$ with one core orbital substituted by one virtual and one active electron excited into a virtual, $S_r^{(-1)}$ with one active electron excited into a virtual, $S_{ij}^{(+2)}$ with two core electrons excited to the active space, $S_{rs}^{(-2)}$ with two active electrons excited to the virtual space (see Fig. 2.1).

If the full dimensionality of such subspaces is exploited, diagonalizing the true Hamiltonian or the model Dyall's Hamiltonian within each $S_l^{(k)}$ spaces, one has the so-called "*totally uncontracted*" NEVPT2 [25]. However, such formulation, not yet implemented, would be feasible for CAS of small and medium size; it is practically not applicable for CAS spaces greater than few thousands configurations, which is common practice in nowadays calculations.

2.4 Internally contracted approach

The prohibitive computational cost of the *totally uncontracted* formalism can be considerably reduced if the perturbers are built as *internally contracted* (IC) functions. This leads to the "*partially contracted*" NEVPT2 and to its further simplification, the "*strongly contracted*" NEVPT2.

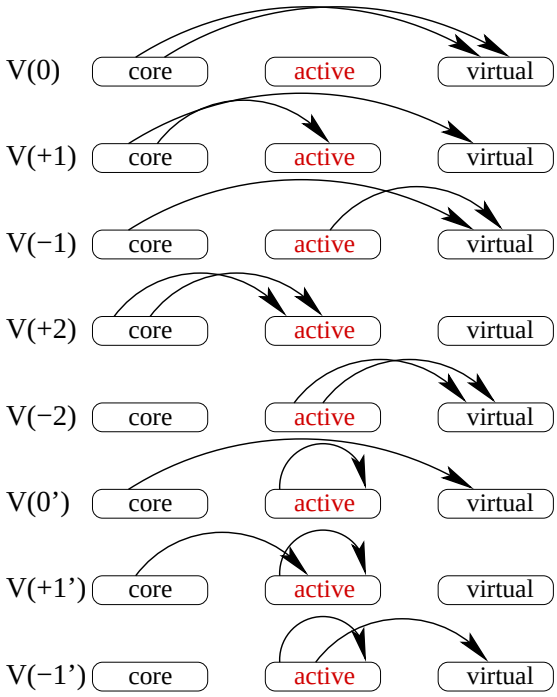

Figure 2.1: Graphical representation of the eight typologies of $S_l^{(k)}$ spaces.

Let Φ be a function external to the CAS space interacting with the reference wavefunction $\Psi_m^{(0)}$, then it has been shown [27,28] that

$$\left\langle \Psi_m^{(0)} \middle| \hat{H} \middle| \Phi \right\rangle = \left\langle \Psi_m^{(0)} \middle| \hat{H} \middle| \hat{P}_{IC}\Phi \right\rangle \tag{2.21}$$

where $\hat{P}_{IC}$ performs a projection onto the "internally contracted" first order space generated by all the functions, external to the CAS, obtained by application of proper strings of spin-traced excitation operators to the reference wavefunction, $E_{wx}E_{yz}\Psi_m^{(0)}$. It follows that the first order corrected wavefunction, $\Psi_m^{(1)}$, which has to be built to compute the second order correction to the energy $E_m^{(2)} = \left\langle \Psi_m^{(0)} \middle| V \middle| \Psi_m^{(1)} \right\rangle$, can be restricted to belong to the IC first order interacting space. Consequently, the dimensionality of the eight $S_l^{(k)}$ subspaces will be now substantially reduced since they will be only spanned by the IC functions $E_{wx}E_{yz}\Psi_m^{(0)}$. Nevertheless, we should stress that the $E_{wx}E_{yz}\Psi_m^{(0)}$ functions are not orthogonal and, generally, not even linearly independent, so that care has to be taken in removing the possible linear dependencies.

2.4.1 The Partially Contracted NEVPT2

The *partially contracted* NEVPT (PC-NEVPT2) approach consists in building the perturbers as multireference wavefunctions belonging to a subspace $\bar{S}_l^{(k)}$ of the vari-

ous IC $S_l^{(k)}$ spaces. One possibility would be to diagonalize the true Hamiltonian H within each such space

$$P_{S_l^{(k)}} \hat{\mathcal{H}} P_{S_l^{(k)}} \Psi_{l,\mu}^{(k)} = E_{l,\mu}^{(k)} \Psi_{l,\mu}^{(k)}$$

but this would be computationally too expensive. Actually, we have adopted the more convenient choice of diagonalizing the model Hamiltonian $\hat{H}^D$. Indeed, it is worthwhile to notice that within a given $S_l^{(k)}$ space

- the active part of $\hat{H}^D$ ($\hat{H}_v$) has matrix elements which do not depend on the inactive orbital pattern l (independent of the specific inactive orbital indices chosen);
- the inactive part $\hat{H}_i$ only gives rise to an energy shift within $S_l^{(k)}$, which is equal to the difference between the orbital energies of the virtual and core orbitals involved in the excitation process.

Thus, for each of the eight typologies of $S_l^{(k)}$, only one single diagonalization has to be performed to get all the eigenfunctions (perturbers) and eigenvalues of $\hat{H}^D$. The general form of the eigenvalues is:

$$E_{l,\mu}^{(k)} = E_m^{(0)} + \Delta\epsilon_l + e_\mu \tag{2.22}$$

where $\Delta\epsilon_l$ equals the difference of the virtual and core orbital energies involved in the definition of $S_l^{(k)}$ and where $E_m^{(0)} + e_\mu$ is the μ-th eigenvalue of the projection of $\hat{H}_v$ onto the IC $S_l^{(k)}$; e_μ is independent of the inactive orbitals and represents a physical process occurring in the active space. In particular, in the $S_{ij,r}^{(+1)}$ subspaces, e_μ approximates an electron affinity due to an electron passing from the core to the active space, in the $S_{ij}^{(+2)}$ subspaces the eigenvalues e_μ approximate an energy of double ionization and so on for the other subspaces.

The zero order Hamiltonian of PC-NEVPT can be written as follows:

$$\hat{H}_0^{\mathrm{PC}} = P_{\mathrm{CAS}} \hat{H} P_{\mathrm{CAS}} + \sum_{l,k} P_{S_l^{(k)}} \hat{H}^D P_{S_l^{(k)}} \tag{2.23}$$

where $P_{S_l^{(k)}}$ is the projector onto the $S_l^{(k)}$ space defined above. It should be remarked that the PC-NEVPT2 has exactly the same degree of contraction of CASPT2 [17,18]; the difference between the two approaches is that PC-NEVPT2 uses multireference correction functions $\Psi_{l,\mu}^{(k)}$ which are eigenfunctions of a simplified two–electron Hamiltonian ($\hat{H}^D$) taking into due account the bielectronic interactions among the active electrons.

For each of the eight $S_l^{(k)}$ spaces, with the exception of the one-dimensional $S_{ij,rs}^{(0)}$ space, the partially contracted perturbation functions are expressed as

$$\Psi_{l,\mu}^{(k)} = |\mathbf{\Phi}\rangle \, \mathbf{C} \tag{2.24}$$

where the $\mathbf{C}$ matrix is obtained by diagonalization of $\hat{\mathcal{H}}^D$ in $S_l^{(k)}$. The first order correction to the wave function is then expressed as linear combination of the perturbation functions

$$\Psi^{(1)}(S_l^{(k)}) = \sum_{\mu} \Psi_{l,\mu}^{(k)} C_{l,\mu}^{(k)(1)} \tag{2.25}$$

where the coefficients $C_{l,\mu}^{(k)(1)}$ have the form

$$C_{l,\mu}^{(k)(1)} = -\frac{\left\langle \Psi_{l,\mu}^{(k)} \middle| \hat{\mathcal{H}} \middle| \Psi_m^{(0)} \right\rangle}{E_{l,\mu}^{(k)} - E_m^{(0)}} \tag{2.26}$$

and the functions are assumed to be normalized.

A schematic analysis of the eight $S_l^{(k)}$ spaces is proposed in Appendix A, focusing attention above all on the form of perturbation functions $\Psi_l^{(k)}$ and of the perturbative coefficients $C_{l,\mu}^{(k)(1)}$, which will be used in the following for the formulation of the PC-NEVPT3.

2.4.2 The Strongly contracted NEVPT2

A further simplification of the NEVPT2 approach can be achieved selecting a single perturber $\Psi_l^{(k)}$ from each IC $S_l^{(k)}$ subspace. $\Psi_l^{(k)}$ is chosen by the following projection:

$$\Psi_l^{(k)} = P_{S_l^{(k)}} \hat{H} \Psi_m^{(0)}. \tag{2.27}$$

In this way a set of orthogonal (but not normalized) correction functions $\Psi_l^{(k)}$ is obtained; their energies are computed as

$$E_l^{(k)} = \frac{\left\langle \Psi_l^{(k)} \left| H \right| \Psi_l^{(k)} \right\rangle}{\langle \Psi_l^{(k)} | \Psi_l^{(k)} \rangle} \tag{2.28}$$

where the use of the Dyall's Hamiltonian guarantees, as usual, a further simplification. This formulation is called *strongly contracted* NEVPT2 (SC-NEVPT2) and is the first approach that has been practically implemented [21,22].

The zero order Hamiltonian of SC-NEVPT2 can be expressed as a spectral decomposition:

$$H_0^{\mathrm{SC}} = P_{\mathrm{CAS}} \hat{H} P_{\mathrm{CAS}} + \sum_{l,k} \left| \Psi_l^{(k)\prime} \right\rangle E_l^{(k)} \left\langle \Psi_l^{(k)\prime} \right| \tag{2.29}$$

where $\Psi_l^{(k)\prime} = \Psi_l^{(k)}/\|\Psi_l^{(k)}\|$ are the normalized perturbers. The second order contribution to the energy, as shown in Ref. [22], can be expressed as

$$E_m^{(2)} = \sum_{l,k} \frac{\|\Psi_l^{(k)}\|^2}{E_m^{(0)} - E_l^{(k)}}. \tag{2.30}$$

The detailed treatment of the various contributions can be found in Ref. [22]. Despite the low number of correction functions employed, the SC-NEVPT2 usually yields results very close to those of the more elaborated PC-NEVPT2. An interesting inequality was proved in Ref. [22], showing that, for each $S_l^{(k)}$ subspace, the contribution to the second order correction to the energy of PC-NEVPT2 is always lower (negative and larger in absolute value) than that of SC-NEVPT2. Cases of consistent discrepancies between SC- and PC-NEVPT2 are usually indicative of some defect in the zero order wavefunction $\Psi_m^{(0)}$ [24, 29–31].

2.5 Major NEVPT2 properties

2.5.1 Absence of intruder states

A well-known problem in MRPTs based on a monoelectronic zero order Hamiltonian is the appearance of the so-called *intruder states*. These are perturbation functions (eigenfunctions of $\hat{H}_0$) with an energy very close to the energy of the reference wavefunction $E_m^{(0)}$, thus producing near divergences in the perturbation summation. This phenomenon is basically related to the improper description of the two-electron interactions between the perturber functions. The intruder state problem affects, for instance, the CASPT2 calculations, where an *ad hoc* unphysical level shift [32] can be used in the denominators to prevent the occurrence of such divergences. Both NEVPT2 variants are practically exempt from the intruder state problem: the energy of the perturbers are always well separated from that of the reference wavefunction. Considering, for instance, the partially contracted approach with Dyall's Hamiltonian we have that the energy of the correction functions $\Psi_{l,\mu}^{(k)}$ are given by

$$E_{l,\mu}^{(k)} = E_m^{(0)} + \Delta\epsilon_l^{(k)} + e_\mu \tag{2.31}$$

where $\Delta\epsilon_l^{(k)}$ and e_μ are both positive quantities, avoiding too small denominators $(E_{l,\mu}^{(k)} - E_m^{(0)})$. We should stress that, however, the $S_r^{(-1)}$ subspace, where an active electron is excited to the virtual space and the other excitation takes place within the active space, could be, in principle and only for highly excited states, liable to the possibility of intruder states. In fact, in presence of extremely diffuse virtual orbitals, ϵ_r is close to zero and e_μ, which refers to an ionization process in the active space, could be very small. Neverthless, in the calculations carried out up to now, we have never observed intruder state problems.

2.5.2 Invariance under orbital rotations

As each $S_l^{(k)}$ subspace is a complete active space, it is clearly invariant under an arbitrary rotation of the active orbitals; this invariance is guaranteed in the three formulations of the method. On the contrary, of course, all the NEVPT methods are not invariant under rotations between active and inactive orbitals, so that attention has to be paid to the choice of the active space in order to avoid possible exchanges of the orbital identities. Moreover, we should stress that the form of Dyall's Hamiltonian of eq. (2.18) is also not invariant under rotations of core and virtual orbitals and *canonical* inactive orbitals (those that diagonalize the Fock matrix) have to be used. Actually, using canonical orbitals is not always possible, like for instance when *a priori* localized orbitals are adopted, so a noncanonical PC-NEVPT2 approach has also been implemented in our laboratory. In this case a modified Dyall's Hamiltonian can be used such that this invariance property is fulfilled; the inactive part of $\hat{H}^D$ is rewritten as

$$\hat{H}'_i = \sum_{ij}^{core} f_{ij} E_{ij} + \sum_{rs}^{virt} f_{rs} E_{rs} \tag{2.32}$$

where f_{ij} and f_{rs} are elements of generalized Fock matrices:

$$f_{ij} = -\left\langle a_i \Psi_m^{(0)} \middle| \hat{H} \middle| a_j \Psi_m^{(0)} \right\rangle + \delta_{ij} E_m^{(0)} \tag{2.33}$$

$$f_{rs} = \left\langle a_r^+ \Psi_m^{(0)} \middle| \hat{H} \middle| a_s^+ \Psi_m^{(0)} \right\rangle - \delta_{rs} E_m^{(0)} \tag{2.34}$$

The zero order Hamiltonian is then defined as

$$H_0 = P_{\mathrm{CAS}} \hat{H} P_{\mathrm{CAS}} + \sum_{\substack{l,k \\ l'k'}} P_{S_l^{(k)}} \hat{H}^D P_{S_{l'}^{(k')}} \tag{2.35}$$

The perturbation equations are solved using a system of linear equations

$$\Psi_m^{(1)} = \sum_{l,k,\mu} c_{l\mu}^{(k)} \Psi_{l,\mu}^{(k)}$$

$$\sum_{l'k'\mu'} c_{l'\mu'}^{(k')} \left\langle \Psi_{l,\mu}^{(k)} \middle| \hat{H}_0 - E_m^{(0)} \middle| \Psi_{l',\mu'}^{(k')} \right\rangle = -\left\langle \Psi_{l,\mu}^{(k)} \middle| \hat{V} \middle| \Psi_m^{(0)} \right\rangle$$

where the $\Psi_{l,\mu}^{(k)}$ functions are obtained by a preliminary PC–NEVPT2 calculation making use of only the diagonal elements of the Fock matrices.

2.5.3 Size consistence

The property of *size consistence*, in the form of *strict separability* directly derives from the above discussed invariance under rotation of the active orbitals (see Ref. [20] for

more details). We recall that the strict separability property assures that, at the limit of non-interaction, the energy of a system A–B is equal to the sum of the energies of the two subsystems A and B calculated separately.

2.6 Quasidegenerate NEVPT2

A well-known defect of the MRPTs belonging to the "diagonalize then perturb philosophy" consists in the fact that the first order correction to the wavefunction does not bring modification to the reference function. Such defect turns out to be rather consistent in cases where the mixing of the configurations in the zero order wavefunction is not properly described due to strongly different correlation effects; typical examples are the avoided crossing between ionic and covalent states or excited states with a mixed valence-Rydberg nature. The reorganization of the determinant coefficients in the zero order wavefunction can be obtained by applying a quasidegenerate perturbative approach [33–35], where an effective Hamiltonian is diagonalized within a configurational space of limited dimension. The quasidegenerate formalism has been implemented for both the strongly and partially contracted (QD-SCNEVPT2 and QD-PCNEVPT2) approaches using the model Dyall's Hamiltonian and is presented in Ref. [23].

In the QD-NEVPT2 approach a model space is built by choosing as basis set a few solutions of the CAS–CI problem $\{\Psi_1^{(0)}, \Psi_2^{(0)}, \ldots, \Psi_g^{(0)}\}$ with $P_{\mathrm{CAS}}\hat{H}P_{\mathrm{CAS}}\Psi_m^{(0)} = E_m^{(0)}\Psi_m^{(0)}$. The purpose of the QD formalism is to provide the true eigenvalues of the Hamiltonian and the projections of the true eigenfunctions onto the model space with the use of an effective Hamiltonian

$$H_{\mathrm{eff}}\widetilde{\Psi}_m = E_m\widetilde{\Psi}_m, \tag{2.36}$$

where $\widetilde{\Psi}_m = P\Psi_m$, $P = \sum_{k=1}^{g} \left|\Psi_k^{(0)}\right\rangle \left\langle\Psi_k^{(0)}\right|$ and E_m is the true eigenvalue associated to the true eigenfunction Ψ_m. Introducing the wave operator, $\Omega\widetilde{\Psi}_m = \Psi_m$, the effective Hamiltonian can be written as $\hat{H}_{\mathrm{eff}} = P\hat{H}\Omega$ and Ω is obtained by solving the generalized Bloch equation

$$\Omega P\hat{H}\Omega - \hat{H}\Omega = 0. \tag{2.37}$$

Adopting a partition of the Hamiltonian, $\hat{H} = \hat{H}_0 + \hat{V}$, with $\hat{H}_0\Psi_m^0 = E_m^0\Psi_m^0$ and expanding Ω and $\hat{H}_{\mathrm{eff}}$ in a perturbation series

$$\Omega = P + \Omega^{(1)} + \Omega^{(2)} + \cdots \tag{2.38}$$

$$\hat{H}_{\mathrm{eff}} = \hat{H}_{\mathrm{eff}}^{(0)} + \hat{H}_{\mathrm{eff}}^{(1)} + \hat{H}_{\mathrm{eff}}^{(2)} + \cdots \tag{2.39}$$

one promptly arrives at the first-order term of Ω

$$\left[\Omega^{(1)}, H_0\right] = QVP \tag{2.40}$$

and to the following terms of $\hat{H}_{\text{eff}}$

$$\hat{H}_{\text{eff}}^{(0)} = P\hat{H}_0 P; \tag{2.41}$$

$$\hat{H}_{\text{eff}}^{(1)} = P\hat{V}P = 0; \tag{2.42}$$

$$\hat{H}_{\text{eff}}^{(2)} = P\hat{V}\Omega^{(1)}. \tag{2.43}$$

Since NEVPT2 is a *state-specific* method with $\hat{\mathcal{H}}_0$ depending on a specific reference function $\Psi_m^{(0)}$, in order to solve the ambiguity about the perturbation functions to use, the multipartitioning technique by Zaitsevski and Malrieu [36] is adopted. Such approach consists in the use of different partitions of the Hamiltonian according to the various wavefunctions $\Psi_m^{(0)}$ of the model space

$$\hat{H} = \hat{H}_0(m) + \hat{V}(m) \tag{2.44}$$

with

$$\hat{H}_0(m) = P_{\text{CAS}}\hat{H}P_{\text{CAS}} + \sum_{l,k,\mu} \left|\Psi_{l,\mu}^{(k)}(m)\right\rangle E_{l,\mu}^{(k)} \left\langle\Psi_{l,\mu}^{(k)}(m)\right|, \tag{2.45}$$

where the perturbation functions $\Psi_{l,\mu}^{(k)}(m)$ are IC functions generated by applying the excitation operators to $\Psi_m^{(0)}$. The matrix elements of $\hat{H}_{\text{eff}}$ up to second order are given by:

$$\left\langle \Psi_n^{(0)} \left| \hat{H}_{\text{eff}} \right| \Psi_m^{(0)} \right\rangle = E_m^{(0)}\delta_{mn} + \sum_{l,k,\mu} \frac{\left\langle \Psi_n^{(0)} \left| \hat{H} \right| \Psi_{l,\mu}^{(k)}(m) \right\rangle \left\langle \Psi_{l,\mu}^{(k)}(m) \left| \hat{H} \right| \Psi_m^{(0)} \right\rangle}{E_m^{(0)} - E_{l,\mu}^{(k)}(m)}. \tag{2.46}$$

The approximate projections $\widetilde{\Psi}_m$ and the corresponding eigenvalues E_m are then obtained by diagonalization of the H_{eff} matrix. We should note that the $\hat{H}_{\text{eff}}$ operator is not hermitian but, if desired, a hermitian matrix can be written using a similarity transformation [37]

$$H'_{\text{eff}} = T^{-1}H_{\text{eff}}T, \tag{2.47}$$

where T is $S^{\frac{1}{2}}$ with $S_{kl} = \langle\widetilde{\Psi_k}|\widetilde{\Psi_l}\rangle$. Finally, we should stress that the QD approach requires just a small computational overhead in comparison to the single-state NEVPT2, since, for the evaluation of the matrix elements of $\hat{H}_{\text{eff}}$ also the transition density matrices have to be computed, but with particle rank not higher than three.

2.7 Third order NEVPT and Internally Contracted CI

Although, usually, a second order treatment is able to provide a conspicuous fraction of the dynamical correlation energy, evaluating the third order correction can be very useful, without prohibitive computational costs, in order to check on the stability judging on the quality of the reference wave function. In fact, when a strong discrepancy is found between the second and third order results, it can be often attributed to a defective zero order description.

As stated in section 2.1, in the RSPT the third order correction to the energy is given by

$$E_m^{(3)} = \left\langle \Psi_m^{(1)} \left| V \right| \Psi_m^{(1)} \right\rangle - E_m^{(1)} ||\Psi_m^{(1)}||^2 \tag{2.48}$$

but, since in NEVPT the first order contribution to the energy is null, eq. (2.48) reduces to

$$E_m^{(3)} = \left\langle \Psi_m^{(1)} \left| V \right| \Psi_m^{(1)} \right\rangle . \tag{2.49}$$

In the strongly and partially contracted approaches $\Psi_m^{(1)}$ is expanded on a rather limited set of correction functions and, as was formerly shown by Werner [38] in his CASPT3 formulation, the task of building a third order algorithm can be achieved without excessive computational effort. For both the NEVPT variants, the third order correction has been implemented in our group [24,25] and a consistent number of applications of its simpler version (SC-NEVPT3) has also been published [24,29–31,39–44].

Here, we shall introduce the third order equations pertaining to the more elaborated partially contracted approach, since its implementation has taken a considerable part of the present research work. The PC first order wavefunction has the form given in (2.25) so, the working equation for PC-NEVPT3 is

$$E_m^{(3)} = \sum_{l',k',\mu'} \sum_{l,k,\mu} C_{l',\mu'}^{(k')(1)*} C_{l,\mu}^{(k)(1)} \left\langle \Psi_{l',\mu'}^{(k')} \left| \hat{H} - \hat{H}_0 \right| \Psi_{l,\mu}^{(k)} \right\rangle . \tag{2.50}$$

We note that the coefficients $C_{l,\mu}^{(k)(1)}$ are computed and stored at the second order level (eq. 2.26) and that $\hat{H}_0$ gives a non null contribution, equal to $E_{l,\mu}^{(k)}$, only in the diagonal case $(l,k,\mu = l',k',\mu')$. Therefore, the PC-NEVPT3 implementation deals with the evaluation of the interaction via the Hamiltonian operator between two Internally Contracted (IC) functions. The main problem of computing the matrix elements $\left\langle \Psi_{l,\mu}^{(k)\prime} \left| \hat{H} \right| \Psi_{l,\mu}^{(k)} \right\rangle$, for all possible occurrence of the IC functions, has been solved by implementing, in the MuPAD [45] computer algebra system, a symbolic program named FRODO (after "Formal Reduction Of Density Operators") [46,47]. In fact, the program FRODO manipulates these matrix elements through the systematic

elimination of the inactive indices from the replacement operators, yielding a list of numerical factors, mono and bielectronic symbolic integrals and strings of excitation operators only confined to the active indices. Then this result is further elaborated in order to produce a Fortran subroutine to perform the calculation of the requested matrix element and, optionally, a LaTeX file.

A detailed analysis of all the 31 classes of interaction that have to be considered is proposed in Appendix B, where, for the sake of simplicity, the nomenclature "$V(k')V(k)$" is used to indicate the generic class $\left\langle \Psi_{l'}^{(k')} \left| V \right| \Psi_{l}^{(k)} \right\rangle$.

Finally, the knowledge of the matrix elements of H between the correction functions makes it possible to build a completely variational calculation where the trial wavefunction is expressed as a linear combination in the form

$$\Psi_m^{\text{trial}} = c_0 \Psi_m^{(0)} + \sum_{l,k,\mu} c_{l\mu}^{(k)} \Psi_{l,\mu}^{(k)}. \tag{2.51}$$

In the case of the partially contracted approach such an expansion corresponds to an Internally Contracted Configuration Interaction (IC–CI) [48] limited to the single and double contracted excitations of $\Psi_m^{(0)}$. IC–CI's are expected to show the same disadvantages present in the more common single reference SD–CI calculations; in particular they loose the size consistence property enjoyed by the NEVPT approach. An example of IC–CI is provided in Ref. [24], concerning the Cr_2 potential energy curve, where the IC–CI result is shown to parallel the third order description.

2.8 A test case: the $X^1\Sigma_g^+$ and $B'^1\Sigma_g^+$ states of C_2

Since the C_2 molecule is a central compound in various interstellar chemical phenomena and combustion reactions, a considerable attention has been paid, by various theoretical chemists [49–53], to the study of the its spectroscopic properties. The major peculiarity of this system is the presence of many low-lying electronic states above the ground state state, $X^1\Sigma_g^+$. The lowest-energy excited state ($^3\Pi_u$) appears only 716 cm^{-1} above the ground state and 16 other excited states have been experimentally observed [54]. This near degeneracy of different electronic states is significant even at the equilibrium geometry and becomes more problematic as the interatomic distance increases, making the use of MR-based methods necessary. Therefore, the C_2 molecule represents a good example to test the performance and the reliability of a MRPT method, which should be, in principle, able to accurately handle neardegeneracy problems and bond–breaking phenomena.

In the present conclusive section the C_2 molecule is chosen as example to present the full set of NEVPT2, NEVPT3 and IC-CI results. The accuracy of our approach

will be judged by comparison with previously published Full CI results [50], which, we recall, within a given one-electron basis set approximation, provide the exact solution to the electronic Schrödinger equation (see Sec. 1.2.1).

2.8.1 Method of calculation

In the light of the testing purpose of the present calculations, essentially aimed to illustrate the behavior of the different degrees of approximation in the NEVPT scheme rather than to provide a comprehensive description of the system, we restricted the study to the ground state, $X^1\Sigma_g^+$, and to the first excited state $B'^1\Sigma_g^+$. Since an avoided crossing occurs between these states around 1.70 Å, we carried out QDNEVPT2 calculations to properly compute the whole Potential Energy Curves (PECs). Besides, in order to obtain a more accurate treatment of the region around the minimum ($r \leq 1.70$ Å) second and third order SS-NEVPT as well as at IC-CI calculations were performed on the ground state.

To make the comparison meaningful, we have used the standard $6-31G^*$ basis set [55], used in the previous Full CI study by Abrams and Sherrill [50].

The zero order wavefunctions were obtained using the *MOLPRO2008.2* package [56]: a State–Averaged CASSCF (SA–CASSCF) calculation on the two $^1\Sigma_g^+$ states was performed for the QDNEVPT2 calculations, whereas a single-root optimization on the ground $X^1\Sigma_g^+$ state was adopted around the equilibrium distance before the NEVPT3 and IC-CI computations. Since *MOLPRO* can only handle with Abelian point groups not higher than D_{2h} , the reduced D_{2h} symmetry was used and the active space was made up by the 8 valence electrons and 8 valence orbitals ($2\sigma_g$, $2\sigma_u$, $3\sigma_g$, $3\sigma_u$, $1\pi_{x,u}$, $1\pi_{y,u}$, $1\pi_{x,g}$ and $1\pi_{x,g}$).

2.8.2 Results and discussion

The PC-QDNEVPT2 and FCI [50] potential energy curves for the ground state, $X^1\Sigma_g^+$, and for the excited state, $B'^1\Sigma_g^+$, are displayed in Fig. 2.8.2 and the total energies are reported in Tab.2.1. While obtaining of the SA-CASSCF wavefunction does not pose particular difficulties at short distances, it becomes quite a difficult task as the bonds is elongated. At longer distances, indeed, the energy curve of the $^1\Delta_g$ state (actually, its component belonging to the A_g irrep. in the D_{2h} point group) first drops below the $B'^1\Sigma_g^+$ (in the range between 1.25 and 1.75 Å) and then also below the $X^1\Sigma_g^+$. At SA-CASSCF level, with the *MOLPRO* package, the selection of the two Σ_g^+ roots was possible by forcing the convergence to the states with the desired value of the quantum number Λ. As stated, the avoided crossing appears around 1.7 Å, where, both at FCI [50] and NEVPT level, the separation between the states is roughly 10 kcal/mol. Then, the $B'^1\Sigma_g^+$ starts to go up in energy but

it becomes again very close to the other at longer distances. In fact, both states dissociate at the same limit 2 C($1s^2 2s^2 2p^2, {}^3P$). As is shown in Fig.2.8.2, where we have plotted only the PC results, the QDNEVPT2 PECs perfectly mimic the shape of the FCI ones, with an overall difference in the absolute energies amounting to $\simeq 0.02$ Hartree.

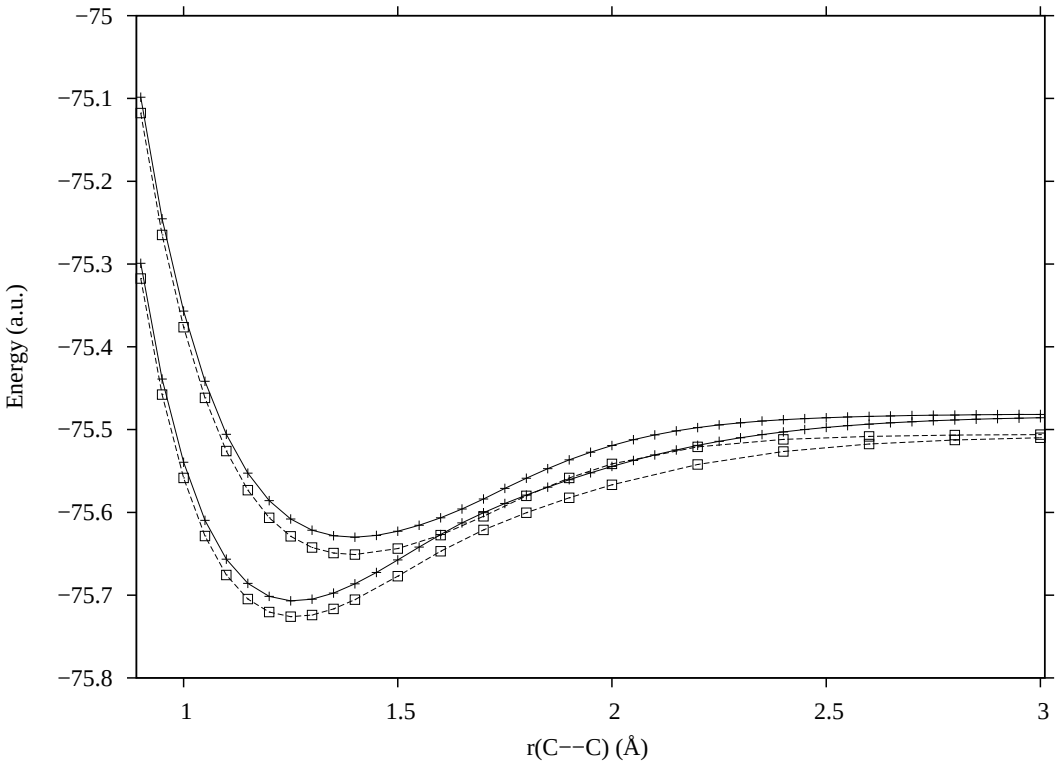

Figure 2.2: PC-QDNEVPT2 ("+" with full lines) and FCI [50] ("□" with dashed lines) PECs for the $X\,{}^1\Sigma_g^+$ and $B'\,{}^1\Sigma_g^+$ states of the C_2 molecule.

A deeper analysis of the computed wavefunctions explains the reasons which make the C_2 molecule a challenging test case even for highly–correlated single-reference methods, at the level, for instance, of Singles and Doubles Couple Cluster with perturbative Triples [CCSD(T)] or high–order Configuration Interaction (CI). Near the equilibrium distance (around 1.25 Å), the ground state wavefunction shows a surprising multireference character, being mainly described by the configuration $(1\sigma_g^2 1\sigma_u^2 2\sigma_g^2 2\sigma_u^2 1\pi_{x,u}^2 1\pi_{y,u}^2)$ with a weight of about 70%, but with a not negligible contribution amounting, to 14%, of the doubly excited configuration $(1\sigma_g^2 1\sigma_u^2 2\sigma_g^2$ $1\pi_{x,u}^2 1\pi_{y,u}^2 3\sigma_g^2)$. At the same geometry, the excited state $B'\,{}^1\Sigma_g^+$ is dominated by the configurations $(1\sigma_g^2 1\sigma_u^2 2\sigma_g^2 2\sigma_u^2 1\pi_{x,u}^2 3\sigma_g^2)$ and $(1\sigma_g^2 1\sigma_u^2 2\sigma_g^2 2\sigma_u^2 1\pi_{y,u}^2 3\sigma_g^2)$ appearing with the same coefficient and by a minor contribution of $(1\sigma_g^2 1\sigma_u^2 2\sigma_g^2 1\pi_{x,u}^2 1\pi_{y,u}^2 3\sigma_g^2)$.

As the interatomic distance increases, the nature of the ground state changes due to the mixing with the $B'^1\Sigma_g^+$ state: the weight of the doubly excited determinant $(2\sigma_g^2)$ $\rightarrow (3\sigma_g^2)$ decreases while that of the two configurations $(1\sigma_g^2 1\sigma_u^2 2\sigma_g^2 2\sigma_u^2 1\pi_{x,u}^2 3\sigma_g^2)$ and $(1\sigma_g^2 1\sigma_u^2\ 2\sigma_g^2 2\sigma_u^2 1\pi_{y,u}^2 3\sigma_g^2)$ progressively increases. Then, around 1.8-1.9 Å the character of the two states is interchanged as a consequence of the avoided crossing.

Table 2.1: QD-NEVPT2 and FCI [50] absolute energies (Hartree) for C_2. The bond distance, r, in Angstrom.

	$X^1\Sigma_g^+$			$B'^1\Sigma_g^+$		
r	SC-QDPT2	PC-QDPT2	FCI	SC-QDPT2	PC-QDPT2	FCI
0.90	-75.296945	-75.299147	-75.317618	-75.093846	-75.098434	-75.117717
0.95	-75.436746	-75.438997	-75.457665	-75.240892	-75.245426	-75.264774
1.00	-75.537208	-75.539483	-75.558335	-75.352471	-75.356832	-75.376449
1.05	-75.607410	-75.609677	-75.628645	-75.437589	-75.441688	-75.461663
1.10	-75.654410	-75.656632	-75.675637	-75.501883	-75.505691	-75.526003
1.15	-75.683662	-75.685806	-75.704813	-75.549173	-75.552701	-75.573273
1.20	-75.699424	-75.701464	-75.720475	-75.582615	-75.585889	-75.606636
1.25	-75.705037	-75.706960	-75.725995	-75.604984	-75.608032	-75.628883
1.30	-75.703134	-75.704938	-75.724026	-75.618661	-75.621510	-75.642414
1.35	-75.695795	-75.697484	-75.716657	-75.625626	-75.628297	-75.649224
1.40	-75.684667	-75.686253	-75.705544	-75.627482	-75.629992	-75.650929
1.50	-75.656049	-75.657494	-75.677127	-75.620627	-75.622839	-75.643794
1.60	-75.625210	-75.626783	-75.646930	-75.604767	-75.606582	-75.627561
1.70	-75.598549	-75.600391	-75.621163	-75.582627	-75.583782	-75.604839
1.80	-75.577403	-75.579135	-75.600442	-75.557715	-75.558759	-75.580101
1.90	-75.559176	-75.560657	-75.582417	-75.535582	-75.536670	-75.558438
2.00	-75.543159	-75.544477	-75.566646	-75.518210	-75.519213	-75.541479
2.20	-75.518133	-75.519152	-75.542142	-75.496885	-75.497636	-75.520806
2.40	-75.502044	-75.502818	-75.526459	-75.487530	-75.488060	-75.511848
2.60	-75.492845	-75.493427	-75.517449	-75.483723	-75.484098	-75.508225
2.80	-75.487899	-75.488369	-75.512568	-75.482140	-75.482413	-75.506703
3.00	-75.485347	-75.485723	-75.509925	-75.481448	-75.481702	-75.506025

In Tab.2.2 the single–state NEVPT and IC-CI total energies for the $X^1\Sigma_g^+$ are listed for $0.90 \leq r \leq 1.70$, where the interaction with the $B'^1\Sigma_g^+$ state can still regarded as minor. Notwithstanding, as shown in Fig.2.8.2, where the percentage error with respect to the FCI banchmark is plotted for each method, approaching the avoided crossing point the single–state treatment becomes defective. Indeed, while all the error curves are flat up to $r \simeq 1.4$ Å, the errors rapidly rise at longer distances. At $r = 1.7$ Å the deviation from the FCI values amounts about to 22-23% (16-18 kcal/mol) at the second order level and to 10-11% (8-9 kcal/mol) at the third

order and IC-CI level. Apart from the sensible improvement attained going to the third order correction to the energy, the most accurate description is obtained at IC-CI level when the partially contracted IC functions are employed. The relative percentage error in this case is $\simeq 2\%$ at short distances and remains slightly less than 10% at $r = 1.7$ Å.

Table 2.2: NEVPT2, NEVPT3 and IC-CI absolute energies (Hartree) for the $X^1\Sigma_g^+$ state. The bond distance, r, in Angstrom.

r	SC-PT2	PC-PT2	SC-PT3	PC-PT3	SC-IC-CI	PC-IC-CI
0.90	-75.297081	-75.299068	-75.311196	-75.313399	-75.312439	-75.315217
0.95	-75.437028	-75.439017	-75.451120	-75.453322	-75.452245	-75.455093
1.00	-75.537684	-75.539638	-75.551769	-75.553914	-75.552795	-75.555648
1.05	-75.608046	-75.609935	-75.622131	-75.624174	-75.623075	-75.625878
1.10	-75.655131	-75.656936	-75.669217	-75.671126	-75.670091	-75.672807
1.15	-75.684415	-75.686127	-75.698500	-75.700254	-75.699311	-75.701919
1.20	-75.700177	-75.701792	-75.714253	-75.715847	-75.715033	-75.717502
1.25	-75.705769	-75.707290	-75.719835	-75.721268	-75.720538	-75.722916
1.30	-75.703826	-75.705256	-75.717885	-75.719157	-75.718543	-75.720801
1.35	-75.696422	-75.697776	-75.710476	-75.711597	-75.711080	-75.713236
1.40	-75.685189	-75.686475	-75.699246	-75.700227	-75.699799	-75.701860
1.45	-75.671413	-75.672644	-75.685483	-75.686336	-75.685988	-75.687962
1.50	-75.656105	-75.657292	-75.670201	-75.670942	-75.670664	-75.672557
1.55	-75.640055	-75.641214	-75.654199	-75.654842	-75.654616	-75.656440
1.60	-75.623880	-75.625027	-75.638106	-75.638661	-75.638475	-75.640235
1.65	-75.608072	-75.609222	-75.622421	-75.622899	-75.622772	-75.624442
1.70	-75.593056	-75.594225	-75.607585	-75.607996	-75.607849	-75.609495

The SS-NEVPT and IC-CI PECs (strongly contracted on the top and partially contracted on the bottom) are plotted along with the FCI ones in Fig.2.8.2. The close-up insets in Fig.2.8.2 make the small differences among the various levels of approximation appreciable.

Finally, using a simple polynomial interpolation around the equilibrium distance, it has been possible to compute the spectroscopic constants reported in Tab.2.3, where the corresponding experimental values [57] and some FCI results [58] are also listed. As is apparent, improving the level of approximation, going from the CASSCF to the partially contracted IC-CI, progressively improves the accuracy of the computed r_e. But, the error still remains $\simeq 0.021$ Å for the PC-IC-CI methods. A good agreement with the experimental values is attained for the harmonic vibrational constant, ω_e, and for the rotational constant, B_e; larger discrepancies are, instead, obtained for the anharmonicity constant $\omega_e x_e$.

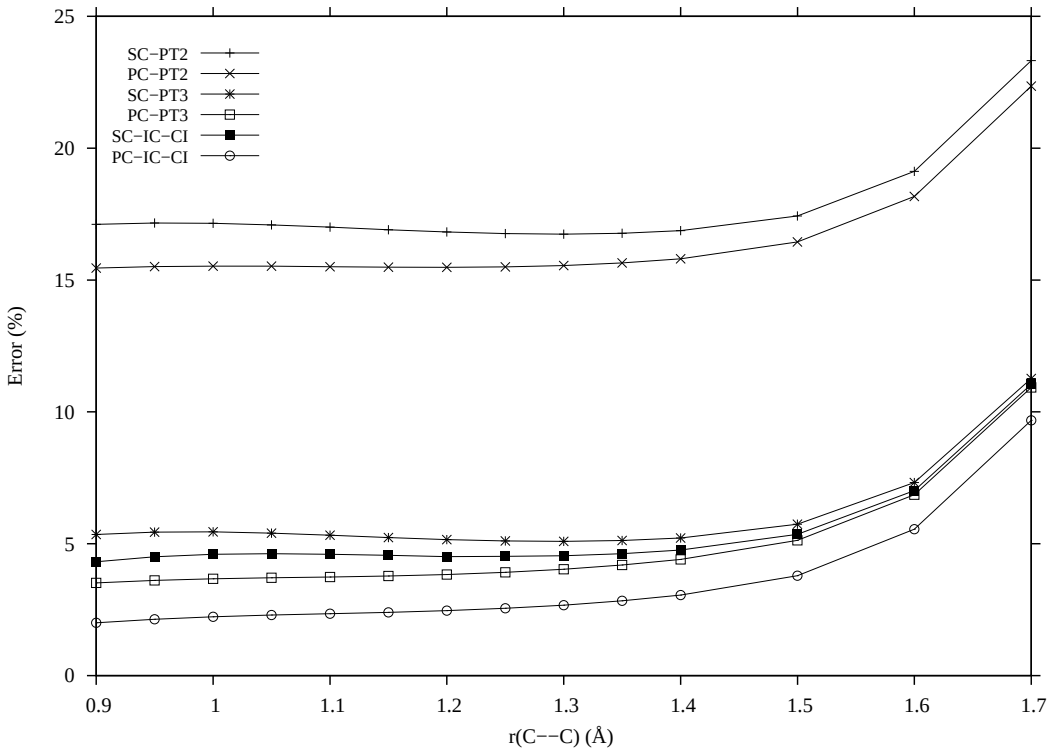

Figure 2.3: NEVPT and IC-CI errors (%) in the total energies with respect to the FCI values [50] for the $X^1\Sigma_g^+$ state of C_2.

Table 2.3: Spectoscopic constants for $X^1\Sigma_g^+$ state of C_2. Energies in Hartree, r_e in Angstrom and the other parameters in cm^{-1}.

Method	U_e	r_e	ω_e	$\omega_e x_e$	B_e
CASSCF	-75.617539	1.2676	1868	13.0	1.747
SC-NEVPT2	-75.706137	1.2650	1860	14.9	1.754
PC-NEVPT2	-75.707627	1.2643	1860	15.3	1.756
SC-NEVPT3	-75.720198	1.2649	1860	14.9	1.755
PC-NEVPT3	-75.721578	1.2637	1860	15.7	1.758
SC-IC-CI	-75.720871	1.2642	1858	14.7	1.756
PC-IC-CI	-75.723224	1.2636	1859	15.7	1.758
FCI/6-31G** [58]	-75.726127	1.2596	1859	13.2	1.771
FCI/cc-pVDZ [58]	-75.729852	1.2727	1813	13.5	1.734
Experiment [57]		1.2425	1855	13.3	1.820

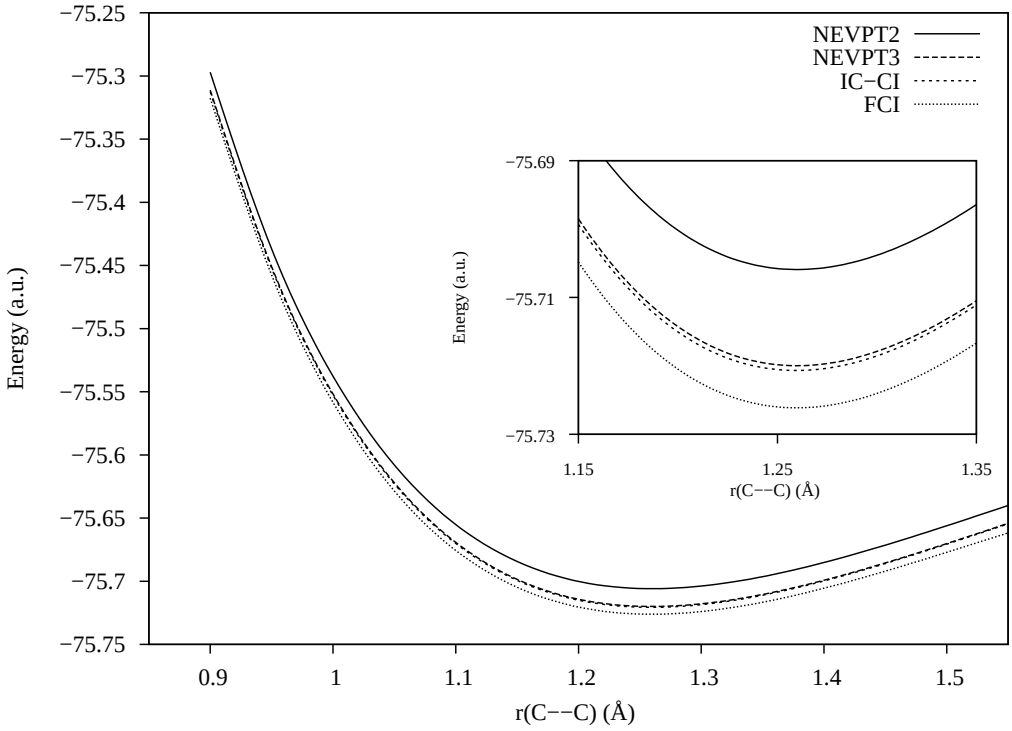

(a) Strongly Contracted

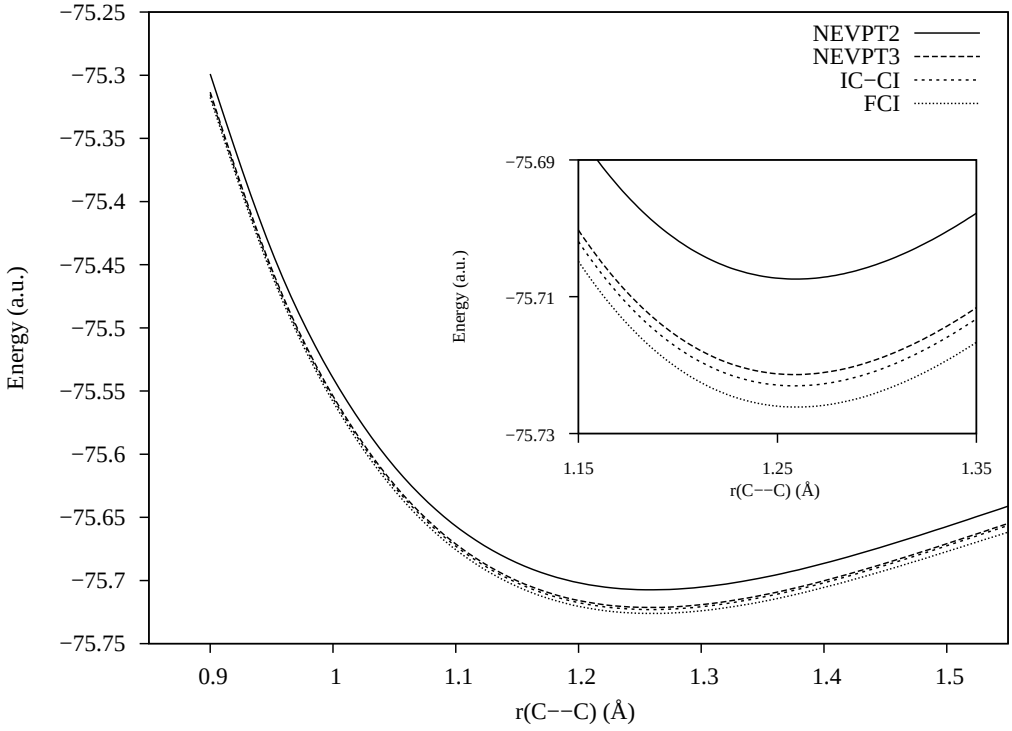

(b) Partially Contracted

Figure 2.4: NEVPT, IC-CI and FCI [50] PECs for the $X^1\Sigma_g^+$ state. All the calculations have been carried out with a standard $6-31G^*$ basis set.

Part I

Excited state calculations

Chapter 3

The hetero–cyclopentadienes

Pyrrole, **Furan** and **Thiophene** (Fig. 3.1) are 1–hetero–2,4–cyclopentadienes, consisting of a butadiene unit linked via an "hetero–atom bridge" (N, O and S respectively) (Fig. 3.1).

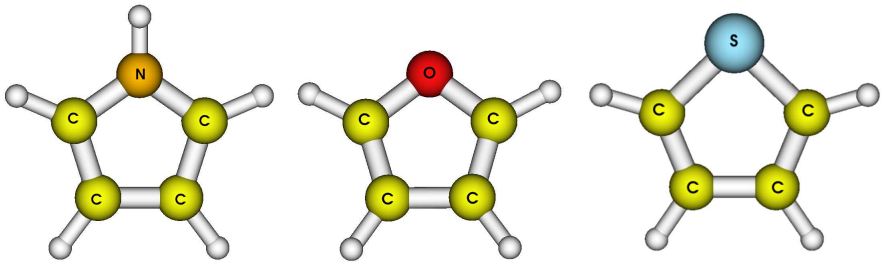

Figure 3.1: Molecular structures of **Pyrrole**, **Furan** and **Thiophene**

The experimental and theoretical investigation of the electronic absorption spectra of the five–membered six π–electrons compounds has received a particular attention since the beginning of the last century. The ongoing interest in their physical chemistry properties and spectroscopical features is certainly motivated by the prominent rôle they play in the biological and pharmaceutical chemistry, as well as in the modern material science (preparation of polymeric and co–polymeric monolayers for data–storage applications [59, 60]). However, despite the large number of joint experimental and theoretical efforts, a detailed interpretation of the absorption spectra of these molecules still remains to be reached and, by now, they are regarded as prototypic examples for the theoretical studies of excited states. The VUV spectra of these systems show a complex profile because of the appearance of rich series of Rydberg transitions, that overlap the valence bands and make the identification of the states quite a difficult task.

After a brief introduction addressing the qualitative interpretation of the valence states (section 3.1), the problem of the Rydberg states and of their mixing with the valence transitions will be discussed (section 3.2). The computational strategy adopted will be then presented in section 5.4. Finally, the results obtained for Pyrrole, Furan and Thiophene will be analyzed in sections 3.4, 3.5 and 3.6 respectively.

3.1 Ionic valence states

Pyrrole, Furan and Thiophene belong to the C_{2v} point group and, following Mulliken's recommendation, the molecules have been placed in the yz plane with the z axis being the C_2 axis. Thus, the five valence π orbitals belong to the B_1 and A_2 irreps and are in the order of energy $1b_1$, $2b_2$, $1a_2$, $3b_1$ and $2a_2$ ($2b_1$, $3b_2$, $1a_2$, $4b_1$ and $2a_2$ for Thiophene). That is, at the single Slater determinant level, the electronic configuration is

- (σ–core)$(1b_1)^2(2b_1)^2(1a_2)^2$ (**Pyrrole and Furan**)
- (σ–core)$(1b_1)^2(2b_1)^2(3b_1)^2(1a_2)^2$ (**Thiophene**)

where the σ–core is composed of 30 electrons in the former case and of 36 electrons in the latter.
The two highest–energy π MOs, $2b_1$ and $1a_2$ for Pyrrole and Furan and $3b_1$ and $1a_2$ for Thiophene, are essentially delocalized over the whole molecular skeleton, whereas the lowest–energy one, $1b_1$, is localized on the hetero–atom. It follows that the four lowest–energy valence $\pi \rightarrow \pi^*$ states are two states of A_1 symmetry and two states of B_2 symmetry.

A qualitative interpretation of the nature of the $\pi \rightarrow \pi^*$ valence states of the five–membered hetero–cyclopentadienes can be obtained by referring to the PPP model [61, 62] for the alternant hydrocarbons. We recall that a hydrocarbon is classified as *alternant* if its C atoms can be partitioned into two categories, in such a way that two adjacent atoms belong always to different categories (the linear polyenes as well as the even–membered cyclic hydrocarbons are alternant systems).
For these systems the PPP Hamiltonian is invariant under particle–hole permutation and it can be proved that the energies of the occupied and virtual orbitals (Fig. 3.2) are symmetric with respect to the LUMO-HOMO energy difference [63, 64].

Let us indicate with $\ldots, 3, 2, 1$ the occupied MOs, in increasing order of energy, and with $1', 2', 3', \ldots$ the unoccupied ones (Fig. 3.2), where the orbitals i and i' are termed a *conjugated pair*. It follows that the two excitations $i \rightarrow j'$ and $j \rightarrow i'$ are degenerate and result in a pair of *minus*, "$-$", and *plus*, "$+$", states. The former state has lower energy and a neutral character, whereas the latter *plus* state is dominated

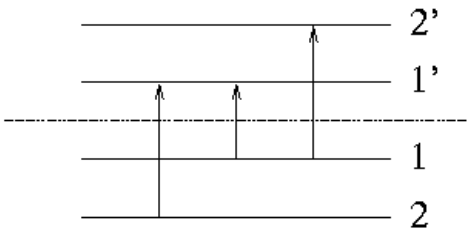

Figure 3.2: Schematic representation of the energies of the occupied and virtual orbitals of an alternant hydrocarbon.

by ionic configurations. The HOMO→LUMO ($1 \rightarrow 1'$) excitation gives rise to an ionic *plus* state as well. Then, the ground state and the doubly–excited configurations $(i)^2 \rightarrow (j')^2$ also are classified as *minus* states. Finally, some simple rules, based on the pairing properties of such systems, predict that only the excitations to *plus* states have oscillator strength different from zero, being, instead, forbidden the transition from a *minus* state (the ground state) to another *minus* state.

Even if the pairing properties are no longer satisfied in the five–membered six–π electrons compounds due to the presence of the hetero–atom, it is still possible to recognize for these molecules a spectroscopical behavior similar to that of alternant hydrocarbons. Therefore, the pair of $^1A_1$ states are a covalent *minus* state ($^1A_1^-$) and an ionic *plus* state ($^1A_1^+$), arising respectively from the symmetric and antisymmetric combination of the two quasi–degenerate configurations $1a_2 \rightarrow 2a_2$ and $2b_1 \rightarrow 3b_1$; the HOMO→LUMO transition is also a ionic *plus* state ($^1B_2^+$). It is worthwhile to stress, however, that, due to the breakdown of the alternant symmetry in the five–membered ring compounds, the excitation to the $^1A_1^-$ state is not strictly forbidden (it appears with low intensity around 6 eV) and the doubly–excited configurations ((HOMO)^2→(LUMO)^2) can interact with both $^1A_1^-$ and $^1A_1^+$ states.

The theoretical description of ionic valence $\pi \rightarrow \pi^*$ in aromatic molecules has been shown to be an extremely difficult task, even for the most refined quantum mechanics methodologies. As discussed by Serrano-Andrés *et al.* [65], it requires the use of quite large basis sets, to properly describe the diffuse nature of some excited states, as well as of highly–correlated methods, in order to take into account the various and differential effects of the dynamical correlation. In particular, the inclusion of the so-called "dynamical σ polarization" (above all its $\sigma - \pi$ component), *i*.e. the response of the σ framework to the change of the charge distribution in the ionic states, is thought to be crucial to get an accurate treatment of these states. This issue has been deeply investigated in a recent work [44], where the ionic V state of ethene is taken as a prototype for the study of the ionic $\pi \rightarrow \pi^*$ states of aromatic

and hetero–aromatic molecules. Through a Valence Bond (VB) decomposition of the wavefunction the nature of the σ polarization is analyzed and an additional (second order) physical effect is introduced: the spatial contraction of the π orbitals as a consequence of the charge displacement due to the polarization of the σ skeleton. In fact, as pointed out by the author [44], in the ionic forms, the effect of the σ polarization consists in moving the charge away from the atom bearing the two π electrons. Such charge reduction results in a contraction of the π orbitals, that, if not properly taken into account, significantly compromises the quality of the results. Clearly a "CASSCF plus perturbation" scheme, with the molecular orbitals optimized at the zero order level, without considering the effect of the dynamical polarization, is unable to provide good quality results. The strategy adopted in Ref. [44] to adequately treat the π contraction is based on an optimization of the MOs in a RASSCF [66] calculation with an appropriate choice of the RAS spaces in order to include, at the zero order level, all the excitations describing the dynamical σ polarization [44]. The author showed that, if the orbitals are properly optimized, accurate results can be obtained at the pertubative level, even using a minimal active space.

As we shall widely discuss later, also in these hetero–aromatic ring compounds the description of the two ionic valence states ($^1A_1^+$ and $^1B_2^+$) poses particular problems, partially alleviated by the inclusion in the active space of π^* orbitals, which allows for a partial contaction of the π orbitals through the interaction with higher energy $\pi \rightarrow \pi^*$ states. However, following the strategy suggested by Angeli [44], the effect of a full RASSCF optimization of the orbitals will be the subject of future investigations.

3.2 Valence–Rydberg interaction

A well–known problem in the spectroscopy of small and medium–sized molecules is the appearence of low–lying *Rydberg* excited states, which due to the overlap with valence transitions, complicate the interpretation of the electronic spectra. We recall that the Rydberg states arise from the promotion of one electron to a very diffuse orbital, characterized by an high quantum number n. Conventionally, for molecules containing atoms belonging to the first and second rows of the periodic system, only the orbitals with $n \geq 3$ are classified as Rydberg orbitals. Note that in the labelling of the Rydberg states of Thiophene, for analogy with Pyrrole and Furan, we have adopted the convention of choosing 3 as the lowest value of n, instead of 4, that would be the appropriate choice for a molecule, containing atoms belonging to the third row (see Ref. [67]).

The Rydberg states are of crucial importance in the characterization of the spectroscopy and photochemistry of small molecules, since they usually appear in the

same energy region of the principal valence $\pi \rightarrow \pi^*$ transitions. Therefore, an accurate theoretical study on the spectroscopy of small– and medium–sized molecules requires a simultaneous treatment of the valence and, at least, of the lowest–energy Rydberg states. This poses particular difficulties when a MRPT approach is employed. In fact, the Rydberg states, due to their "diffuse" nature, with the excited electron far from the molecular frame, are less sensitive to the dynamical correletion effects than the valence excited states. Therefore, at CASSCF level, Rydberg states lie at low energy, close to the valence states and a mixing among the wavefanctions may occur. When at CASSCF level such valence–Rydberg mixing takes place, the application of a single–state perturbative correction, leaving the coefficients of the zero order wavefunction unchanged, is unreliable and a quasi–degenerate perturbative approach (section 2.6) should be applied. On the other hand, it is also possible that two or more states, which are not mixed in the zero order description, become near degenerate after the perturbative correction in such a way that a mixing is liable to happen.

In the case of the hetero–cyclopentadienes, the excitation from the HOMO ($1a_2$) into diffuse s, p and d orbitals originates the R–series states, whereas the excitation out of the SHOMO ($2b_1$ for Pyrrole and Furan and $3b_1$ for Thiophene) gives rise to the so–called R$'$–series of Rydberg states. Since the energy differences between the first (IP_1) and second (IP_2) are around 1.0-1.5 eV, a rich structure of Rydberg bands is expected to appear in the UV spectra. As discussed in the following, the effects of the valence–Rydberg mixing were found to be significant for Furan and Thiophene and have been suitably treated at QD–NEVPT2 level.

3.3 Computational approach

For the computation of the vertical transition energies the experimental ground state geometries were used [68–70]. It is worthwhile to stress that the "theoretical vertical" transition energy is computed as the difference between the energy of the ground state at its equilibrium geometry (the minimum of the Potential Energy Surface) and that of the excited state again at the ground state equilibrium geometry; this value is usually compared with the peak of the experimental absorption band. However, as argued by Davidson and Jarzecki [71], this assumption holds, within the Born–Oppenheimer and Franck–Condon approximations (Fig. 3.3), provided that the vibronic excited state is high enough. But, as confirmed by the frequently observed asymmetry of the absorption bands, this could not be the case for small and medium size molecules, with excited states only slightly distorted. As a consequence, the comparison between the experimental maximum of the band and the computed vertical excitation energy should always be regarded with care.

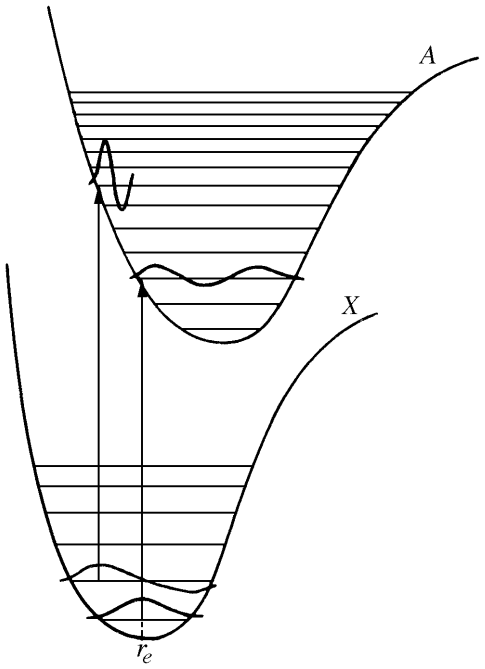

Figure 3.3: Electronic vertical transitions.

All the calculations were carried out with a contracted ANO-L basis set [72] adopting the contraction scheme S[5*s*4*p*2*d*], C,N,O[4*s*3*p*1*d*] and H[2*s*1*p*]. Note that this is the same valence basis set employed in the first CASPT2 work by Serrano-Andrés et al. [73]. In order to describe the Rydberg molecular orbitals, the above mentioned valence basis set was augmented with molecule–centered [74] diffuse functions. These basis functions were obtained by contraction of a set of 8*s*8*p*8*d* gaussian primitives, whose exponents were optimized as described by Kaufmann *et al.* [75] (Tab. 3.1). The contraction coefficients, reported in Tab. 3.1, were computed following the methodology developed by Roos *et al.* [74] with a contraction scheme [1*s*1*p*1*d*], thus confining ourselves to the calculation of 3s, 3p and 3d Rydberg states.

As already mentioned, Pyrrole, Furan and Thiophene belong to the C_{2v} point group, and the molecules have been placed in the yz plane with the z axis as the C_2 symmetry axis. The classification in the C_{2v} point group of the Rydberg orbitals is reported in Tab. 3.2.
The molecular orbitals were obtained from average CASSCF calculations using the MOLCAS5.4 package [76], averaging over all the states of interest for a given symmetry. Finally, the five 1*s* orbitals were kept uncorrelated during the subsequent second and third order NEVPT treatment.

	exponent	contraction coefficients		
		Pyrrole	**Furan**	**Thiophene**
1s				
	0.0246239324	0.3491	0.3219	0.4275
	0.0112533427	-2.3860	-2.2167	-2.2881
	0.0058583805	2.9273	2.5387	2.5127
	0.0033459739	-4.4334	-3.8427	-3.8323
	0.0020484225	5.2412	4.5278	4.5108
	0.0013236424	-4.4946	-3.8760	-3.8598
	0.0008930958	2.4185	2.0836	2.0746
	0.0006243129	-0.5996	-0.5163	-0.5140
1p				
	0.0423352810	0.0639	0.0764	0.1668
	0.0192542060	-0.7939	-0.7924	-0.5250
	0.0099882106	0.0798	0.0453	-0.2721
	0.0056893607	-0.8192	-0.7636	-0.5877
	0.0034756797	0.8973	0.8328	0.4575
	0.0022420590	-0.8142	-0.7546	-0.4294
	0.0015106399	0.4682	0.4337	0.2464
	0.0010547527	-0.1255	-0.1162	-0.0660
1d				
	0.0605402013	0.0079	0.0115	0.1190
	0.0274456919	-0.2356	-0.2534	0.3315
	0.0142043987	-0.2935	-0.3072	0.2779
	0.0080765930	-0.4987	-0.4892	0.3967
	0.0049271863	0.0186	0.0370	-0.0464
	0.0031748110	-0.1878	-0.1860	0.1598
	0.0021371230	0.0991	0.1011	-0.0870
	0.0014910155	-0.0292	-0.0297	0.0255

Table 3.1: Exponents [75] and contraction coefficients $(8s8p8d) \rightarrow [1s1p1d]$ for the Rydberg basis set

3.3.1 Active Spaces

Pyrrole and Furan

The study was addressed to the computation of the three lowest–energy valence $\pi \rightarrow \pi^*$ states ($^1B_2^+$, $^1A_1^-$ and $^1A_1^+$) as well as the six $\pi \rightarrow \pi$–Rydberg and $\pi \rightarrow \sigma$–Rydberg states, with $n = 3$. Therefore, since no excitations from σ orbitals were

Symmetry	Orbitals
$\mathbf{a}_1$	ns, np_z, nd_{z^2}, $nd_{x^2-y^2}$
$\mathbf{b}_1$	np_x, nd_{xz}
$\mathbf{b}_2$	np_y, nd_{yz}
$\mathbf{a}_2$	nd_{xy}

Table 3.2: Classification of the Rydberg orbitals into C_{2v} point group

considered, only the six π–electrons were active and two different types of active space were used.

Wee shall refer to every active space with a sequence of four indices, where each index indicates the number of orbitals for a given symmetry species (a_1, b_1, b_2, a_2 in order).

For the calculations of the $\pi \rightarrow \sigma^*$ states (B_1 and A_2) one need not include in the active space π–type Rydberg orbitals, while for the description of $\pi \rightarrow \pi^*$ states (A_1 and B_2) only π–type molecular orbitals (valence and Rydberg) are necessary. So, for the $\pi \rightarrow \pi^*$ states the smallest active space consists of the five (0302) valence π orbitals and three (0201) Rydberg–type orbitals (0503), whereas for the $\pi \rightarrow \sigma^*$ states it is composed of the five valence π orbitals and six (4020) Rydberg–type orbitals (4322) (see Tab. 3.2). However, in order to estimate the effects of the enlargement of the active space with π virtual orbitals, we have also carried out some calculations with eleven (0704), thirteen (0805) and fifteen (0906) active orbitals. We shall discuss in detail the effects of the active space size for the Pyrrole molecule, presenting the results computed with all the above indicated active spaces. Otherwise, since we found a similar behavior for the excited states of Furan, in section 3.5 we shall just report the CAS(0906) and CAS(0805) results. A summary of all the active spaces used and the corresponding number of states included in the average CASSCF calculations is given in Tab. 3.3.

Table 3.3: Active spaces and number of states used in the CASSCF calculations.

Nature	Symmetry	Active space	Number of states
$\pi \rightarrow \pi^*$	A_1	(0503), (0704), (0805), (0906)	6
	B_2		4
$\pi \rightarrow \sigma^*$	B_1	(4322)	6
	A_2		6

Thiophene

For the Thiophene molecule, we focused on the computation of the vertical excitation energy of the four low–lying $\pi \rightarrow \pi^*$ valence states: the two $^1B_2$ states mainly dominated by the $1a_2 \rightarrow 4b_1$ and $3b_1 \rightarrow 2a_2$ excitations respectively and the two $^1A_1$ states arising from the antisymmetric ($^1A_1(V)$) and symmetric ($^1A_1(V')$) linear combination of the two $1a_2 \rightarrow 2a_2$ and $3b_1 \rightarrow 4b_1$ configurations[1]. Moreover, since the experimental ionization potential of the $11a_1$ lone pair amounts to 12.1 eV [77], two $n \rightarrow \pi^*$ valence states (A_2 and B_1 symmetries) are expected near 9-10 eV. So, for the calculations of $\pi \rightarrow \pi^*$, $n \rightarrow \pi^*$ and $\pi \rightarrow \sigma^*$ excited states, the six π–electrons and the two lone pair electrons were active in all the calculations (the $1b_1$ π orbital, localized on the sulfur atom, was included into the inactive core). Two different types of active spaces were employed: one to compute the $\pi \rightarrow \pi^*$ and $n \rightarrow \pi^*$ states and one for the $\pi \rightarrow \sigma^*$ states. For the calculations of π–type excited states, the minimum active space should include the five π valence orbitals, the lone pair orbital and the three π Rydberg orbitals, resulting in a space (1503). Nevertheless, also for Thiophene, the use of such active space has been proved to be inadequate to get a satisfactory description of the $\pi \rightarrow \pi^*$ valence states; therefore, here we shall present only the results obtained with a larger space, composed of 12 active orbitals (1704) and 8 active electrons. Then, for the calculations of the $\pi \rightarrow \sigma^*$ states one need not include in the active space π–type Rydberg orbitals (b_1 and a_2 symmetries), and the smallest active space is a (5322) space, composed of the lone pair orbital, the five π valence orbitals and of the six Rydberg σ–type orbitals. However, as we shall discuss later (section 3.6.1), in order to treat the effects of the mixing occurring among a low–energy $\pi \rightarrow \sigma^*$ valence state and some $3p$ and $3d$ Rydberg states, the use of an extended active space, including one more orbital of b_2 symmetry (5332), was necessary. The excitation energy of each state was determined with respect to the corresponding ground state $^1A_1$, computed for both the 1704 and 5332 spaces, taking into account that, while a state–averaged CASSCF calculation was performed in the former case, a single–root optimization was carried out in the latter.

3.4 Pyrrole

3.4.1 The UV absorption spectrum

The electronic absorption spectrum of Pyrrole, in the region between $\simeq 5$ and $\simeq 8$ eV, has been widely investigated by both theoretical [73, 78–87] and experimental [77, 78,

[1] Note that for the the valence states of Thiophene, following the previous studies, we have adopted a different notation with respect to the usual *minus* and *plus* nomenclature used for Furan and Pyrrole.

88–96] studies. However, in spite of such a high number of studies an unambiguous assignment of the main spectrum features still remains to be reached.

The spectrum profile shows two regions of intense absorption, located around 6 and 7.5 eV respectively; another weak central band appears near 7 eV. According to the traditional experimental interpretation [90,92,95], the intensity of the lowest-energy band can be ascribed to a valence $\pi \rightarrow \pi^*$ state ($^1B_2^+$) while the second intense absorption region is attributed to the presence of high–lying valence states, like the strong $^1A_1^+$ transition. Another low–energy $\pi \rightarrow \pi^*$ state ($^1A_1^-$) is expected to be located in the first band system but, because of its weak intensity, an experimental assignment is not available in the literature.

Overlaid on these valence bands are two sets of Rydberg series, termed R– and R′–series. For a more comprehensive historical review see Ref. [73, 79]. Here we just remark that most of the discrepancies among the previous *ab initio* studies mainly concern the interpretation of the lowest–energy band. The issue is whether the $^1B_2^+$ valence state belongs to the first absorption region or not. CASPT2 studies published first by Serrano-Andrés *et al.* [73] and then by Roos *et al.* [79], in agreement with the traditional interpretation, locate this valence vertical transition at 6.00 and 5.87 eV respectively. However, almost all the subsequent *ab initio* investigations, starting from the multireference Møller-Plesset (MRMP) calculations by Hashimoto *et al.* [87] and including the sophisticated coupled cluster study by Christiansen *et al.* [83], yielded results significantly higher (0.5-0.7 eV) than those obtained in the CASPT2 works. As pointed out by Roos *et al.* [79], some experimental evidence is consistent with the CASPT2 attribution of the valence state $^1B_2^+$ to the lowest–energy absorption region. This band is observed both in the vapor and condensed phases with a maximum located at 5.96 [97] and 5.90 eV [93] respectively. This peak can also be found, placed at 6.0 eV [93], in the crystal spectrum. Since Rydberg states are thought to be less important in condensed phase, it is most unlikely that this band should arise solely from pure Rydberg transitions.

On the other hand, a better agreement is achieved among the various theoretical studies for the transition energies of Rydberg states, which are generally less sensitive to the dynamical correlation effects.

Anyway, it is important to keep in mind that, as shown by Werner in a recent paper [85], the valence excited states have non–planar equilibrium structures, so that a considerable geometry relaxation is expected. A study involving only the planar structures therefore tends to underestimate these relaxation effects. The difficult handling of the Rydberg–valence mixing, that may occasionally occur in the calculations, could be another source for such discrepancies.

3.4.2 The singlet valence states

As is expected on the basis of the considerations reported in section 3.1 about the spectroscopical behavior of the five–membered ring compounds, both the $^1A_1$ states have a multireference nature (symmetric and antisymmetric combination of the $1a_2 \rightarrow 2a_2$ and $2b_1 \rightarrow 3b_1$ configurations) and a small fraction (more consistent in the *minus* state) of the doubly excited configuration $(1a_2)^2 \rightarrow (3b_1)^2$ is expected to be present.

As is apparent from the values in Tab. 3.12, in the calculations with the smallest active space (0503) a different behavior in the treatment of the three valence states can be recognized: the description of the covalent state appears quite coherent, whereas considerable variations are evident in the NEVPT results for the two ionic states. In particular, for the *plus* states, the SC-NEVPT2 and PC-NEVPT2 calculations provided excitation energies significantly dissimilar, revealing a deficient CASSCF description. The difference between the two NEVPT2 results amounts to 0.36 eV for the $^1A_1^+$ state and 0.23 eV for the $^1B_2^+$ state and the sizeable increase of the excitation energies produced by the third order correction is a further indication of an improper reference wavefunction. Also, for these ionic states, it is interesting to notice that at the second order level a large reduction of the CASSCF transition energies is found (1.28 eV for the $^1B_2^+$ state and 0.72 eV for the $^1A_1^+$ state).

In order to improve the CASSCF function, calculations using active spaces of increasing size were performed. Actually, we have also made use of active spaces including occupied and virtual σ orbitals, but no remarkable improvements in the perturbative trend were observed, therefore these results are not reported here. On the contrary, the inclusion of π virtual orbitals into the active space yielded better results, as shown by the values in Tab. 3.12. As can be seen, the extension of the CAS space produces a pronounced lowering of the CASSCF excitation energies, amounting to $\simeq 0.7$ eV in the case of the $^1B_2^+$ state and $\simeq 0.9$ eV for the $^1A_1^+$ state. An improved consistency among the NEVPT values was consequently achieved using the (0704), (0805) and (0906) CAS spaces, but it must be stressed that the latter spaces (0805 and 0906) do not bring substantial improvements with respect to the (0704) one.

With the (0704) space for instance, the discrepancies between the SC-NEVPT2 and PC-NEVPT2 excitation energies were reduced to 0.12 eV for the $^1A_1^+$ state and 0.15 eV for the $^1B_2^+$ state. As a confirmation of the improvement obtained in the CASSCF description, the third order correction brought about just a small increase in the transition energies with respect to those calculated at PC-NEVPT2 level.

But, despite the improvement yielded by the extension of the CAS space, for the

ionic states the NEVPT results turn out significantly higher than those of the other theoretical methods.

Our largest calculation (SC-NEVPT3 with 0906), for istance, locates the vertical transition to the $^1B_2^+$ state at 7.05 eV, where a value of 5.87 eV is obtained by Roos *et al.* [79], of 6.63 eV (CC3) by Christiansen *et al* [83] and of 6.51 eV by Hashimoto *et al* [87].

Table 3.4: Vertical excitation energies (eV) for the $\pi \rightarrow \pi^*$ valence states of Pyrrole. Comparison between the NEVPT and previous theoretical results.

Method	$^1A_1^-(\pi \rightarrow \pi^*)$	$^1B_2^+(\pi \rightarrow \pi^*)$	$^1A_1^+(\pi \rightarrow \pi^*)$
	Active space (0503)		
CASSCF	6.55	7.94	9.68
SC-NEVPT2	6.85	6.66	8.96
PC-NEVPT2	6.78	6.43	8.62
SC-NEVPT3	6.68	7.07	9.14
	Active space (0704)		
CASSCF	6.33	7.27	8.71
SC-NEVPT2	6.66	7.22	8.54
PC-NEVPT2	6.62	7.07	8.42
SC-NEVPT3	6.51	7.24	8.50
	Active space (0805)		
CASSCF	6.37	7.23	8.76
SC-NEVPT2	6.57	7.11	8.43
PC-NEVPT2	6.53	6.96	8.30
SC-NEVPT3	6.51	7.12	8.47
	Active space (0906)		
CASSCF	6.37	7.23	8.82
SC-NEVPT2	6.63	7.07	8.44
PC-NEVPT2	6.59	6.95	8.29
SC-NEVPT3	6.56	7.05	8.48
previous works			
CASPT2[a][73]/ [79]	5.92/5.82	6.00/5.87	7.46
MRMP/MCQD [87]	5.98/6.01	6.51/6.51	7.48/7.51
CC3 [83][b]	6.37	6.63	8.07
CCSD(R) [83][b]	6.43	6.63	8.12
CCSD [83][c]	6.53	6.61	8.00
MRCI [86]	6.11	6.73	8.19
SAC-CI [81]	6.41	6.48	7.88
ADC(2) [80]	6.66	6.71	7.75
DFT (B97-2) [86]	6.61	6.55	

[a] MS-CASPT2 calculations in Ref. [79]

[b] Experimental equilibrium geometry and basis set as Ref. [73]

[c] aug-cc-pVTZ basis set with 7s7p7d molecule-centered functions

In the more recent CASPT2 study [79] the authors found a strong interaction between this valence state and the Rydberg $1a_2 3p_x$ so that the multi–state approach even reversed their positions. To investigate the effects of the valence–Rydberg interaction on the states of B_2 symmetry, we have also applied a quasi–degenerate second order correction (QD-NEVPT2) [23], but, as shown in Tab. 3.5, we did not find considerable changes in the excitation energies. Indeed, in the NEVPT calculations, the sizable energy difference (slightly lower than 1 eV) between the $^1B_2^+$ and $1a_2 \rightarrow 3p_x$ state does not allow any mixing between the wavefunctions.

Table 3.5: QD-NEVPT2 verical transition energies (eV) for the states of B_2 symmetry of Pyrrole.

	Active space (0704)		Active space (0805)	
States	SC-QDPT2	PC-QDPT2	SC-QDPT2	PC-QDPT2
$1^1B_2(1a_2 \rightarrow 3p_x)$	6.15	6.09	6.09	6.02
$2^1B_2(1a_2 \rightarrow 3d_{xz})$	6.86	6.80	6.80	6.72
$3^1B_2(2b_1 \rightarrow 3d_{xy})$	7.89	7.85	7.82	7.76
$4^1B_2^+(\pi \rightarrow \pi^*)$	7.26	7.15	7.14	7.04

Similar remarks can be made about the $^1A_1^+$ state, whose multireference nature, in addition to its ionic character, makes it a difficult task for all the *ab initio* methods. The NEVPT excitation energies are significantly higher (roughly 1 eV) than the CASPT2 values [73, 79], but a better agreement is otherwise attained with the coupled cluster results [83]. With the (0704), (0805) and (0906) spaces the difference between NEVPT values and those calculated by Christiansen *et al.* [83] never exceeds 0.5 eV, as was the case for the $^1B_2^+$ state.

Finally some interesting remarks can be made about the covalent valence state $^1A_1^-$, whose CASSCF description appears satisfactory even with (0503) space. As is evident, very similar results were obtained from the two different second order calculations: with all the active spaces the difference between SC-NEVPT2 and PC-NEVPT2 is always lower than 0.1 eV. The third order correction brought just a small reduction of the transition energies, amounting roughly to 0.1 eV in the (0503) and (0704) space, to 0.02 eV in (0805) and, finally, to 0.05 eV in the (0906) space.
Overall, our results for this state agree with the previous *ab initio* calculations by Trofimov and Schirmer [80], Wan *et al.* [81] and Christiansen *et al.* [83]. The best NEVPT3 values (0704, 0805, 0906 spaces) and the CC3 vertical transition energy differ by ~ 0.2 eV at most. Otherwise, our perturbative results are again significantly higher (~ 0.7 eV) than those calculated in the CASPT2 studies by Serrano-Andrés

et al. [73] and Roos *et al.* [79].

3.4.3 The π–type Rydberg states

Table 3.6: Vertical excitation energies (eV) for the π–type Rydberg states of Pyrrole. Comparison between the NEVPT and previous theoretical results.

Method	2^1A_1 $1a_2 \rightarrow 3d_{xy}$	3^1A_1 $2b_1 \rightarrow 3p_x$	5^1A_1 $2b_1 \rightarrow 3d_{xz}$	1^1B_2 $1a_2 \rightarrow 3p_x$	2^1B_2 $1a_2 \rightarrow 3d_{xz}$	3^1B_2 $2b_1 \rightarrow 3d_{xy}$
			Active space (0503)			
SC-NEVPT2	6.95	7.19	7.69	6.24	6.95	7.96
PC-NEVPT2	6.96	7.19	7.65	6.26	6.97	7.98
SC-NEVPT3	6.62	6.83	7.39	5.90	6.61	7.58
			Active space (0704)			
SC-NEVPT2	6.82	7.08	7.80	6.17	6.88	7.89
PC-NEVPT2	6.83	7.09	7.81	6.13	6.85	7.84
SC-NEVPT3	6.63	6.81	7.52	5.92	6.64	7.61
			Active space (0805)			
SC-NEVPT2	6.78	6.97	7.72	6.10	6.82	7.81
PC-NEVPT2	6.77	6.96	7.71	6.05	6.77	7.76
SC-NEVPT3	6.66	6.82	7.56	5.94	6.68	7.64
			Active space (0906)			
SC-NEVPT2	6.75	6.92	7.71	6.08	6.80	7.78
PC-NEVPT2	6.74	6.90	7.70	6.06	6.78	7.75
SC-NEVPT3	6.67	6.78	7.55	5.98	6.62	7.59
previous works						
CASPT2[a][73]/ [79]	6.54	6.65	7.36	5.78/6.09	6.53	7.43
MRMP/MCQD [87]	6.38/6.37	6.62/6.64	7.20/7.20	5.87/5.88	6.61/6.62	7.36/7.39
CC3 [83][b]	6.77	6.94	7.60	5.98	6.91	7.66
CCSDR(3) [83][b]	6.78	6.95	7.62	5.97	6.89	7.67
CCSD [83][c]	6.73	6.89	7.53	5.82	6.86	7.59
MRCI [86]	6.51	6.67	7.35	5.86	6.57	7.37
SAC-CI [81]	6.64	6.86	7.49	5.88	6.76	7.55
ADC(2) [80]	6.54	6.43	7.23	5.86	6.48	7.26
DFT (B97-2) [86]	6.86			6.05	6.90	

[a] MS-CASPT2 calculations in Ref. [79]

[b] Experimental equilibrium geometry and basis set as Ref. [73]

[c] aug-cc-pVTZ basis set with 7s7p7d molecule–centered functions

As can be seen in Tab. 3.6, the NEVPT results of the pure Rydberg states show quite a coherent trend. Since no significant valence–Rydberg mixing occurred, the zero order description was not problematic and even the smallest active space (0503) could provide good results. Contrary to what we have previously seen for the valence states, the differences between the values of the two second order variants are

negligible (the largest deviation amounts to 0.05 eV). The progressive extension of the CAS space gave rise to a lowering of the second order excitation energies and to a corresponding attenuation of the third order correction. With the exception of the $2b_1 \rightarrow 3d_{xz}$ state in the (0503) calculation, where probably a small Rydberg–valence mixing takes place, the NEVPT3 results, using different active spaces, for a given transition are all very similar, with differences not exceeding 0.07 eV. Furthermore, a remarkable agreement is obtained between NEVPT3 and the best coupled–cluster results (CC3), with the difference not exceeding 0.23 eV (2^1B_2 state). A weak interaction with the $\pi \rightarrow \pi^*$ valence state ($^1B_2^+$) might be the reason for this small discrepancy.

Finally, a good accordance is obtained between the SC-NEVPT3 and the the CASPT2 results. Nevertheless, the NEVPT2 excitation energies for the six π Rydberg states are, on average, higher (≤ 0.4 eV) than the CASPT2 ones of Serrano-Andrés *et al.* [73], MRCI by Palmer *et al.* [86] and SAC-CI by Wan *et al.* [81]

3.4.4 The σ–type Rydberg states

Table 3.7: Vertical excitation energies (eV) for the $^1B_1$ Rydberg states of Pyrrole. Comparison between the NEVPT and previous theoretical results.

	1^1B_1	2^1B_1	3^1B_1	4^1B_1	5^1B_1	6^1B_1
Method	$1a_2 \rightarrow 3p_y$	$2b_1 \rightarrow 3s$	$1a_2 \rightarrow 3d_{yz}$	$2b_1 \rightarrow 3p_z$	$2b_1 \rightarrow 3d_{a_1}$	$2b_1 \rightarrow 3d_{a_1}$
SC-NEVPT2	6.19	6.40	6.79	7.07	7.76	7.86
PC-NEVPT2	6.21	6.42	6.81	7.09	7.79	7.89
SC-NEVPT3	5.84	5.99	6.47	6.67	7.32	7.41
previous works						
CASPT2[a][73]/ [79]	5.85/5.87	5.97	6.40	6.62	7.32	7.39
MRMP/MCQD [87]	5.81/5.80	5.70/5.75	6.45/6.44	6.48/6.50	7.14/7.13	7.23/7.21
CC3 [83][b]	5.85	5.99	6.47	6.72	7.31	7.37
CCSDR(3) [83][b]	5.86	6.01	6.47	6.74	7.32	7.39
CCSD [83][c]	5.82	5.97	6.43	6.67	7.33	7.45
MRCI [86]	5.84	6.34	6.45	6.89	7,30	7.48
DFT (B97-2) [86]	6.00	6.11	6.61			
SAC-CI [81]	5.80	6.05	6.39	6.68	7.34	7.26
ADC(2) [80]	5.69	5.59	6.20	7.00	6.88	

[a] MS-CASPT2 calculations in Ref. [79]

[b] Experimental equilibrium geometry and basis set as in Ref. [73]

[c] aug-cc-pVTZ basis set with 7s7p7d molecule–centered functions

The perturbative results, obtained with the (4322) space, show an extremely consistent trend (Tabs. 3.7 and 3.8): the difference between the SC-NEVPT2 and PC-NEVPT2 values is indeed never larger than 0.03 eV and, moreover, the third order correction leads to a regular decrease in the transition energies, amounting

roughly to 0.4 eV. Since no low–energy valence states were present in the average CASSCF calculations and hence the zero order description was not affected by any Rydberg–valence mixing effect, one can clearly appreciate the systematic improvement brought by the third order correction. It is interesting to remark that, probably due to the same reason, the vertical excitation energies obtained from the various *ab initio* methods are quite similar. However, this is not the case for the MRCI results by Palmer *et al.* [86], which are, on average, higher than those reported in the other high–level studies.

The NEVPT3 excitation energies are in excellent agreement with the CC3 results, with a difference never going beyond 0.06 eV (2^1A_2 state). Furthermore, in opposition to what was found for the valence and π Rydberg states, a remarkable accordance with the CASPT2 [73] results was also attained; indeed, the SC-NEVPT3 and CASPT2 transition energies differ by 0.05 eV at most.

Table 3.8: Vertical excitation energies (eV) for the $^1A_2$ Rydberg states of Pyrrole. Comparison between the NEVPT and previous theoretical results.

	1^1A_2	2^1A_2	3^1A_2	4^1A_2	5^1A_2	6^1A_2
Method	$1a_2 \rightarrow 3s$	$1a_2 \rightarrow 3p_z$	$1a_2 \rightarrow 3d_{a_1}$	$1a_2 \rightarrow 3d_{a_1}$	$2b_1 \rightarrow 3p_y$	$2b_1 \rightarrow 3d_{yz}$
SC-NEVPT2	5.43	6.11	6.74	6.84	7.22	7.77
PC-NEVPT2	5.45	6.14	6.77	6.87	7.23	7.79
SC-NEVPT3	5.10	5.80	6.40	6.52	6.81	7.36
previous works						
CASPT2[a][73]/ [79]	5.08/5.22	5.83/5.97	6.42	6.51	6.77	7.31
MRMP/MCQD [87]	4.92/4.91	5.74/5.74	6.38/6.37	6.44/6.43	6.70/6.65	7.25/7.22
CC3 [83][b]	5.10	5.86	6.43	6.50	6.84	7.36
CCSDR(3) [83][b]	5.12	5.87	6.44	6.52	6.86	7.37
CCSD [83][c]	5.12	5.83	6.40	6.48	6.81	
MRCI [86]	5.59	6.12	6.80	6.57	6.71	7.30
DFT (B97-2) [86]	5.18	5.97	6.61	6.55		
SAC-CI [81]	5.11	5.81	6.38	6.44		
ADC(2) [80]	4.99	5.65	6.21	6.33	6.41	6.92

[a] MS-CASPT2 calculations in Ref. [79]

[b] Experimental equilibrium geometry and basis set as in Ref. [73]

[c] aug-cc-pVTZ basis set with 7s7p7d molecule–centered functions

3.5 Furan

3.5.1 The UV absorption spectrum

The investigation of the electronic absorption spectrum of Furan has a long history and a large number of experimental [77, 94–96, 98–104] and theoretical works [73, 81,82,84,103,105–109] have been published. Analogously to Pyrrole, the ultraviolet

(UV) spectrum exhibits two principal regions of absorption, located around 6 and 8 eV and two rich series of overlapped $\pi \rightarrow$ Rydberg transitions. While the various experimental and theoretical studies are in substantial agreement in ascribing the two absorption regions to the $\pi \rightarrow \pi^*$ valence states $^1B_2^+$ and $^1A_1^+$ respectively, some discussion concerns the exact position of the covalent $^1A_1^-$ state. The controversial question is whether the vertical transition to the $^1A_1^-$ state is lower or higher in energy than the $^1B_2^+$ one. Palmer and co–workers, in their MRCI study [103], computed the $^1A_1^-$ state to lie below the $^1B_2^+$ one and assigned the former to a peak observed at 5.80 eV. Their conclusions were also corroborated by some experimental works [101, 104], such as the UV absorption study on jet–cooled Furan by Roebber *et al.* [101], who suggested that the peak at 5.80 eV should show a valence character because of its insensitivity to the formation of molecular clusters, where the Rydberg states are thought to play a minor role. Nevertheless, all the more recent *ab initio* calculations [81,107–109] do not support this interpretation, computing the $^1A_1^-$ valence transition at the high–energy side of the $^1B_2^+$ state. Indeed, as shown by Gromov *et al.* in their extensive molecular dynamics study [109], the partial valence character and the unexpected intensity of the forbidden $^1A_2(3s)$ excitation, can be explained by a vibronic interaction with higher energy dipole–allowed transitions, like the $^1B_2^+$ and $^1A_1^-$ valence states. Finally, other ambiguities concern the assignment of the $B_1(3p_y)$ and $B_2(3p_x)$ states as well as other high–energy Rydberg states [103, 107].

3.5.2 Valence–Rydberg mixing

In Tabs. 3.9 and 3.10 the single–state and quasi–degenerate NEVPT excitation energies for the $\pi \rightarrow \pi^*$ states of Furan ($^1A_1$ and $^1B_2$ respectively) are reported. As is apparent, despite the use of rather large active spaces, the perturbative treatment of the two ionic valence states ($^1B_2^+$ and $^1A_1^+$) remains problematic, as was also the case for the ionic valence states of Pyrrole [29](Sec. 3.4). Indeed, both in the single–state and quasi–degenerate (QDNEVPT2) calculations, significant differences ($\simeq 0.2$ eV) between the SC and PC second order results are evident. Then, further complications arise from the strong valence–Rydberg effects that take place both at the zero and second order level. In order to check on the occurrence of valence–Rydberg interactions in the zero order description, we have evaluated, as is common practice, the expectation value of the second moment of the charge distribution: values of $\langle x^2 \rangle$ in the range between 25-35 a.u. are indeed typical values for pure valence states.

Table 3.9: Single–state and quasi–degenerate (QD) vertical transition energies (eV) for the $^1A_1$ states of Furan.

Method	$^1A_1^-$	$1a_2 \rightarrow 3d_{xy}$	$2b_1 \rightarrow 3p_x$	$2b_1 \rightarrow 3d_{xz}$	$^1A_1^+$
	Active space (0704)				
SC-NEVPT2	6.77	7.44	8.22	8.89	8.94
PC-NEVPT2	6.73	7.44	8.20	8.88	8.77
SC-NEVPT3	6.67	7.33	8.02	8.69	8.71
SC-QDNEVPT2	6.76	7.45	8.22	9.11	8.72
PC-QDNEVPT2	6.71	7.46	8.20	9.10	8.56
	Active space (0805)				
SC-NEVPT2	6.68	7.44	8.16	8.83	8.87
PC-NEVPT2	6.64	7.42	8.13	8.80	8.69
SC-NEVPT3	6.64	7.37	8.06	8.73	9.00
SC-QDNEVPT2	6.68	7.44	8.16	9.03	8.67
PC-QDNEVPT2	6.62	7.43	8.13	9.01	8.49

Table 3.10: Single-state and quasi–degenerate (QD) vertical transition energies (eV) for the $^1B_2$ states of Furan.

Method	$1a_2 \rightarrow 3p_x$	$1a_2 \rightarrow 3d_{xz}$	$^1B_2^+$	$2b_1 \rightarrow 3d_{xy}$
	Active space (0704)			
SC-NEVPT2	6.74	7.36	7.22	8.97
PC-NEVPT2	6.67	7.29	7.04	8.88
SC-NEVPT3	6.64	7.27	7.42	8.82
SC-QDNEVPT2	7.05	7.65	6.63	8.97
PC-QDNEVPT2	6.91	7.67	6.42	8.88
	Active space (0805)			
SC-NEVPT2	6.71	7.29	7.23	8.92
PC-NEVPT2	6.63	7.21	7.05	8.82
SC-NEVPT3	6.65	7.26	7.37	8.85
SC-QDNEVPT2	7.02	7.61	6.61	8.92
PC-QDNEVPT2	6.87	7.62	6.41	8.82

In Tab. 3.11 the values of $\langle x^2 \rangle$ obtained from the average CASSCF calculations are listed and compared with those recomputed after the QD correction. At the

average CASSCF level, for the excited states of A_1 symmetry the valence–Rydberg mixing can be regarded as negligible, whereas a consistent mixing is evident for the $^1B_2$ states. Indeed, with both active spaces, the $^1A_1^-$ and $^1A_1^+$ states have values of $\langle x^2 \rangle$ of $\simeq 25$ and $\simeq 32$ a.u., in accordance with their valence character; on the contrary, the $^1B_2^+$ state shows too large a value of $\langle x^2 \rangle$ ($\simeq 45$ a.u.), revealing a small Rydberg component. As shown both by the NEVPT results in Tab. 3.9 and the values of $\langle x^2 \rangle$ in Tab. 3.11, the covalent valence state $^1A_1^-$ and the two $1a_2 \rightarrow 3d_{xy}$ and $2b_1 \rightarrow 3p_x$ Rydberg states are not affected by any mixing.

The application of the QD approach leaves substantially unchanged their excitation energies and the SC-NEVPT3 result can be regarded as reliable.
On the other hand, after the second order correction the $^1A_1^+$ valence state and the $2b_1 \rightarrow 3d_{xz}$ Rydberg state become very close in energy and, since their coupling ($\simeq 0.09$ a.u.) is greater than their energy difference ($\simeq 0.04$ a.u.), the QD correction allows for a consistent interaction between the two wavefunctions. As one can reasonably expect, the application of the QD approach brings about a decrease in the excitation energy of the valence state ($\simeq 0.2$ eV), which is more sensitive to the dynamical correlation effects, and a corresponding increase in the excitation energy of the Rydberg state. Also, as is apparent in Tab. 3.11, after the QD approach the value of $\langle x^2 \rangle$ of the valence (Rydberg) state is increased (decreased) by about 5 a.u.

Table 3.11: $\langle x^2 \rangle$ component of the second moment of the charge distribution (a.u.) for the $^1A_1$ and $^1B_2$ states of Furan. The values have been obtained using two different active spaces

		Active Space (0704)		Active Space (0805)	
State	Nature	$\langle x^2 \rangle^a$	$\langle x^2 \rangle^b$	$\langle x^2 \rangle^a$	$\langle x^2 \rangle^b$
$^1A_1^-$	$\pi \rightarrow \pi^*$	25.84	24.85	25.26	24.74
$^1A_1$	$1a_2 \rightarrow 3d_{xy}$	88.22	88.95	89.93	90.30
$^1A_1$	$2b_1 \rightarrow 3p_x$	75.29	74.95	76.66	76.35
$^1A_1$	$2b_1 \rightarrow 3d_{xz}$	86.20	81.86	86.18	81.53
$^1A_1^+$	$\pi \rightarrow \pi^*$	32.72	37.07	31.68	36.64
$^1B_2$	$1a_2 \rightarrow 3p_x$	73.38	70.65	73.59	68.68
$^1B_2$	$1a_2 \rightarrow 3d_{xz}$	81.68	89.62	79.81	89.02
$^1B_2^+$	$\pi \rightarrow \pi^*$	44.86	38.09	45.15	39.82
$^1B_2$	$2b_1 \rightarrow 3d_{xy}$	87.93	87.95	89.08	89.08

[a] Values obtained from the average CASSCF calculations

[b] Values recomputed after the PC-QDNEVPT2 correction

Since a remarkable valence–Rydberg mixing occurs both at the zero order and second order levels, the treatment of the states of B_2 symmetry turns out to be

rather problematic. As can be noticed in Tab. 3.10 only the $2b_1 \rightarrow 3d_{xy}$ state is not influenced by the application of the QD correction. The strongest mixing takes places between the $1a_2 \rightarrow 3p_x$ and the valence state in such a way that the application of the quasi–degenerate approach even interchanges their positions. After the QD calculations, the identification of the valence and Rydberg states was possible on the basis of the recomputed values of the second moment of the charge distribution. As shown in Tab. 3.11, at the "partially contracted" level, where the interaction is more consistent and hence the QD approach is more efficient, the value of $\langle x^2 \rangle$ of the $^1B_2^+$ state amounts to $\simeq$ 39 a.u, whereas a value of $\simeq$ 45 a.u. was obtained from the average CASSCF calculations. Finally, a noticeable change in the excitation energies of the $1a_2 \rightarrow 3d_{xz}$ Rydberg state is also observed; its transition energies are increased by $\simeq$ 0.3 eV with respect to those computed at the single–state level.

In conclusion, it is interesting to remark that no significant improvements were obtained increasing from eleven (0704) to thirteen (0805) the number of active orbitals, since the extent of the valence–Rydberg mixing is not modified and the lowering of the second order transition energies amounts to 0.1 eV at most.

3.5.3 Singlet Valence States

In Tab. 3.12 the SC-NEVPT3 and PC-QDNEVPT2 excitation energies, obtained with the (0805) space are reported and compared with the previous theoretical results and the available experimental assignments. Since, as previously discussed (section 3.6.1), the two ionic states ($^1B_2^+$ and $^1A_1^+$) are strongly influenced by the interaction with the Rydberg states, the consistent differences ($\simeq$ 0.6 eV) between the SC-NEVPT3 and PC-QDNEVPT2 values are not surprising. Therefore for these two states, in the following discussion, we shall refer only to the QD excitation energies.

The PC-QDNEVPT2 calculation locates the $^1B_2^+$ state at 6.41 eV, in excellent agreement with the previous coupled cluster computations by Christiansen and Jørgensen [107], SAC-CI by Wan *et al.* [81] and EOM-CCSD by Gromov *et al* [108].

A very good agreement with the coupled cluster results is also observed for the $^1A_1^+$ state, whose PC-QDNEVPT2 excitation energy is 8.49 eV, only 0.14 eV higher than the CC3 result and 0.07 eV lower than the CCSD one. This agreement is even more meaningful when considering that the CC computations were performed using the same geometry [69] and ANO basis set [72] used in the present study. Taking into account the rather significant discrepancies ($\simeq$ 0.2-0.3 eV) [107, 108] between the computed vertical transition energy and the observed maximum of the band, our present results confirm the traditional attribution of the broad bands at 6 and 8 eV

to the valence $^1B_2^+$ and $^1A_1^+$ states respectively.

Table 3.12: Computed vertical transition energies for the $\pi \rightarrow \pi^*$ valence states of Furan compared with the previous theoretical results and the experimental data.

Method	$^1B_2^+$	$^1A_1^-$	$^1A_1^+$
SC-NEVPT3[a]	7.37	6.64	9.00
PC-QDNEVPT2[a]	6.41	6.62	8.49
previous works			
CASPT2 [73]	6.04	6.16	7.74
MRMP/MCQD [105]	5.95/5.99	6.16/6.19	7.69/7.72
CC3 [107][b]	6.35	6.61	8.35
CCSD [107][b]	6.49	6.86	8.56
CCSD [107][c]	6.45	6.82	8.34
MRCI [103]	6.76	6.02	8.32
SAC-CI [81]	6.40	6.79	8.34
ADC(2) [106]	6.37	6.70	8.16
TD-DFT (B97-1) [84]	6.12	6.76	
EOM-CCSD [108]	6.49	6.84	
Expt.(vert.)	6.04[d,e]		7.80[e]

[a] Active Space (0805)

[b] Experimental equilibrium geometry [69] and basis set as in Ref. [73]

[c] aug-cc-pVTZ basis set augmented with 7s7p7d ring–centered diffuse functions

[d] Refs. [77, 95, 98, 99]

[e] Ref. [103]

Finally, the NEVPT calculations, in agreement with most of all the other *ab initio* studies and with the traditional experimental interpretation, predict the $^1A_1^-$ state to be about 0.2 eV higher in energy than the $^1B_2^+$ one. Its excitation energy at SC-NEVPT3 level is computed at 6.64 eV, only 0.03 eV higher than the CC3 result (6.61 eV). A good accordance with the TD-DFT [84] and EOM-CCSD [108] excitation energies is also attained. On the other hand, for the three valence states, the CASPT2 results by Serrano-Andrés *et al.* [73] and MRMP by Hashimoto *et al.* [105] turn out to be significantly lower than the NEVPT ones. Apart from the case of the $^1A_1^+$ state, where, as pointed out by the authors [73], the presence of intruder states could compromise the accuracy of the result, the differences between the NEVPT and CASPT2 values amount roughly to 0.4-0.5 eV.

3.5.4 Singlet Rydberg states

In Tab. 3.13 the SC-NEVPT3 and PC-QDNEVPT2 excitation energies (0805 space) of the π–type Rydberg states are reported and compared with those obtained in the previous theoretical works and with the experimental data. Instead, in Tabs. 3.14 and 3.15 we present the second and third order single–state NEVPT results obtained for the σ–type Rydberg states: the excited states are separated into the $1a_2 \rightarrow 3l$ (Tab. 3.14) and $2b_1 \rightarrow 3l$ states (Tab. 3.15).

Table 3.13: Computed vertical transition energies for the π–type Rydberg states of Furan compared with the previous theoretical results and the experimental data.

	$^1A_1$	$^1A_1$	$^1A_1$	$^1B_2$	$^1B_2$	$^1B_2$
Method	$1a_2 \rightarrow 3d_{xy}$	$2b_1 \rightarrow 3p_x$	$2b_1 \rightarrow 3d_{xz}$	$1a_2 \rightarrow 3p_x$	$1a_2 \rightarrow 3d_{xz}$	$2b_1 \rightarrow 3d_{xy}$
SC-NEVPT3[a]	7.37	8.06	8.73	6.65	7.26	8.85
PC-QDNEVPT2[a]	7.43	8.13	9.01	6.87	7.62	8.82
previous works						
CASPT2 [73]	7.31			6.48	7.13	
MRMP/MCQD [105]	7.26/7.29			6.50/6.11	7.18/7.21	
CCSD [107][b]	7.58	8.26		6.94	7.72	
MRCI [103]	7.75	8.15	8.33	6.66	7.71	8.94
SAC-CI [81]	7.36	8.14	8.95	6.82	7.51	8.79
ADC(2) [106]	7.22	7.71	8.51	6.73	7.35	8.32
TD-DFT (B97-1) [84]	7.47			6.83	7.55	
Expt.	7.28[c], 7.52[d]		8.46(?)[d]	6.47[d]		8.77[d]

[a] (0805)Active Space

[b] aug-cc-pVTZ basis set augmented with 7s7p7d ring–centered diffuse functions

[c] Refs. [77, 95, 98, 99]

[d] Ref. [103]

3s Rydberg States

In the NEVPT calculations the $1a_2 \rightarrow 3s$ Rydberg transition is predicted to be the lowest–energy excited state of Furan (Tab. 3.14). At the second order level its excitation energy is computed at 6.11 (SC-NEVPT2) and 6.13 eV (PC-NEVPT2); a slight reduction ($\leq$ 0.1 eV) is observed in the SC-NEVPT3 calculation, where this state is computed at 6.00 eV. As can be seen, the computed excitation energies agree with those obtained in the previous theoretical studies [73,81,84,103,107,108].

Table 3.14: Computed vertical excitation energies (eV) for the $1a_2 \rightarrow \sigma^*$ Rydberg states of Furan compared with the previous theoretical results and the experimental data.

$1a_2 \rightarrow 3l$	$^1A_2$	$^1B_1$	$^1A_2$	$^1A_2$	$^1B_1$	$^1A_2$
Method	$3s$	$3p_y$	$3p_z$	$3d_{x^2-y^2}$	$3d_{yz}$	$3d_{z^2}$
SC-NEVPT2	6.11	6.67	6.77	7.26	7.39	7.44
PC-NEVPT2	6.13	6.68	6.79	7.28	7.39	7.46
SC-NEVPT3	6.00	6.56	6.65	7.14	7.27	7.31
previous works						
CASPT2 [73]	5.92	6.46	6.59	7.00	7.15	7.22
MRMP/MCQD [105]	5.84/5.84	6.40/6.40	6.53/6.54	6.98/6.98	7.10/7.12	7.18/7.19
CCSD[a][107]	6.11	6.64	6.80	7.12	7.32	7.39
MRCI(DZPR) [103]	5.95	6.63	6.41	7.15	6.99	7.40
TD-DFT (B97-1c) [84]	5.97	6.58	6.69	7.03	7.21	7.27
SAC-CI [81]	5.99	6.45	6.66	7.04	7.14	7.27
ADC(2) [106]	5.86	6.35	6.50	6.89	6.98	7.11
EOM-CCSD [109]	6.04	6.56	6.71			
Expt.	5,94[d],5.80[b]	6.47[b], 6.76[c]	6.61[b]		7.28[c]	

[a] aug-cc-pVTZ basis set with 7s7p7d molecule–centered functions

[b] Refs. [77, 95, 98, 99, 102]

[c] Ref. [103]

[d] Refs. [101, 104]

On the basis of electron–energy loss (EEL) measurements, the $2b_1 \rightarrow 3s$ ($^1B_1$) transition was assigned by Palmer and co–workers [103] to a peak at 7.38 eV. The most accurate NEVPT result places the vertical transition of this state at 7.41 eV (SC-NEVPT3 value in Tab. 3.15), in agreement with the experimental assignment and the previous CCSD [107], SAC-CI [81] and TD-DFT [84] results.

3p Rydberg States

The three $1a_2 \rightarrow 3p$ Rydberg states are one π-type state ($^1B_2(3p_x)$) and two σ–type states ($^1B_1(3p_y)$ and $^1A_2(3p_z)$). Some discussion concerns the energetical order of the $^1B_1(3p_y)$ and $^1B_2(3p_x)$ states. In particular, two p–type Rydberg transitions were experimentally observed at 6.47 [77,96,99,103] and 6.76 eV [102,103]. In their MRCI study, Palmer and co–workers [103] assigned the lower transition (6.47 eV) to the $^1B_2(3p_x)$ state and the higher one (6.76 eV) to the $^1B_1(3p_y)$ state. However, in the subsequent theoretical studies [81, 84, 106, 107], the assignment proposed by Palmer *et al.* [103] was questioned and reversed. For instance, in the best CC calculations [107] the $^1B_1(3p_y)$ state was estimated to be about 0.3 eV lower then the $^1B_2(3p_x)$ one. Similar results were also attained in the more recent SAC-CI [81] and TD-DFT [84] studies. Our most accurate calculations locate the vertical transition to the

$^1B_1(3p_y)$ and $^1B_2(3p_x)$ states at 6.56 (Tab. 3.14) and 6.87 eV (Tab. 3.13) respectively. Thus, the NEVPT results fully confirm the energy difference amounting to $\simeq 0.3$ eV computed in the CC [107] and TD-DFT [84] studies and the reassignment suggested by those authors. Finally, a peak located at 6.61 eV was attributed by Flicker *et al.* to the $1a_2 \rightarrow 3p_z$ transition. The SC-NEVPT3 excitation for the $^1A_2(3p_z)$ state is 6.65 eV (Tab. 3.14), in excellent accordance with experiments and the previous SAC-CI (6.66 eV) [81], TD-DFT (6.69 eV) [84] and EOM-CCSD (6.69 eV) [108] calculations.

Table 3.15: Computed vertical excitation energies (eV) for the $2b_1 \rightarrow \sigma^*$ Rydberg states of Furan compared with the previous theoretical results and the experimental data.

$2b_1 \rightarrow 3l$	$^1B_1$	$^1A_2$	$^1B_1$	$^1B_1$	$^1A_2$	$^1B_1$
Method	$3s$	$3p_y$	$3p_z$	$3d_{x^2-y^2}$	$3d_{yz}$	$3d_{z^2}$
SC-NEVPT2	7.68	8.18	8.30	8.83	8.85	9.00
PC-NEVPT2	7.69	8.18	8.31	8.84	8.85	9.02
SC-NEVPT3	7.41	7.99	7.99	8.53	8.64	8.69
previous works						
CASPT2 [73]	7.21					
MRMP/MCQD [105]	7.31/7.25					
CCSD[a][107]	7.52	8.14	8.11			
MRCI(DZPR) [103]	7.14	7.90	8.04	8.36	8.00	8.39
TD-DFT (B97-1c) [84]	7.41		8.07			
SAC-CI [81]	7.45	8.07	8.54	8.87		
ADC(2) [106]	7.05	7.57	7.61	8.06	8.16	8.23
Expt.[b]	7.38		8.10	8.46		8.77(?)

[a] aug-cc-pVTZ basis set with 7s7p7d molecule–centered functions

[b] Ref. [103]

It is certainly rather problematic to get an accurate description of the high–energy Rydberg states. However, for the three $2b_1 \rightarrow 3p$ transitions, the PC-NEVPT2 excitation energies are 8.13 ($^1A_1(3p_x)$ in Tab. 3.13), 8.18 ($^1A_2(3p_y)$ in Tab. 3.15) and 8.31 eV ($^1B_1(3p_z)$ in Tab. 3.15). A slight lowering of the transition energies is observed at the third order level (SC-NEVPT3), where the three states are computed at 8.06, 7.99 and 7.99 eV respectively. However, a reversed energetical order ($^1B_1(3p_z) \leq {}^1A_2(3p_y) \leq {}^1A_1(3p_x)$) is found in the coupled cluster study by Christiansen and Jørgensen [107], and different orders are also obtained from the MRCI [103] and SAC-CI [81] calculations. In addition, a firm experimental assign-

ment is not available for these states, with the exception of the $^1A_1(3p_x)$) transition, located by Palmer *et al.* [103] at 8.10 eV.

3d Rydberg States

The best NEVPT excitation energies of the five $1a_2 \rightarrow 3d$ states are 7.14 ($^1A_2(3d_{x^2-y^2})$ in Tab. 3.14), 7.27 eV ($^1B_1(3d_{yz})$ in Tab. 3.14), 7.31 eV ($^1A_2(3d_{z^2})$ in Tab. 3.14), 7.33 eV ($^1A_1(3d_{xy})$ in Tab. 3.13) and, finally, 7.62 eV ($^1B_2(3d_{xz})$ in Tab. 3.13). As can be seen, due to its interaction with the $^1B_2^+$ valence state, the transition energy of the $1a_2 \rightarrow 3d_{xz}$ state is noticeably underestimated (about 0.3-0.4 eV) at the single–state level and this pronounced valence–Rydberg mixing could be the reason for the too low excitation energy (7.13 eV) computed in the single–state CASPT2 study by Serrano–Andrés *et al* [73]. On the contrary, for this state, the PC-QDNEVPT2 result agrees with the CCSD [107], MRCI [103], SAC-CI [81] and TD-DFT [84] transition energies. A satisfactory accordance with the previous theoretical studies is also attained for the other four states: with the exception of some MRCI results (see $^1B_1(3d_{yz})$ and $^1A_1(3d_{xy})$ states), the largest discrepancies amount indeed to $\simeq 0.2$ eV.

Finally, our most accurate excitation energies for the five $2b_1 \rightarrow 3d$ Rydberg states are 8.53 ($^1B_1(3d_{x^2-y^2})$ in Tab. 3.14), 8.64 ($^1A_2(3d_{yz})$ in Tab. 3.14), 8.69 ($^1B_1(3d_{z^2})$ in Tab. 3.14), 8.85 ($^1B_2(3d_{xy})$ in Tab. 3.13) and 9.01 eV ($^1A_1(3d_{xz})$ in Tab. 3.13). As is apparent, very different values have been obtained for these high–energy Rydberg states in the previous theoretical studies [81, 103, 106] and, up to now, no well–established experimental assignments are available in the literature. Since, as estimated by Christiansen and Jørgensen [107], the difference between the adiabatic and vertical transition energy, for the $1a_2 \rightarrow 3l$ states, does not exceed 0.16 ± 0.03 eV, the NEVPT vertical excitation energies support the attribution of the peak at 8.46 eV [103] to the the $^1B_1(3d_{x^2-y^2})$ state (computed at 8.53 eV).

3.6 Thiophene

As we shall discuss later, no large attention has been paid in the literature to the theoretical investigation of the electronic spectrum of Thiophene and therefore its interpretation is still far from being complete, since consistent discrepancies (*i.e.* up to 0.7-0.8 eV) among the various *ab initio* results exist. For this reason, for almost all the xcited states under consideration, the accuracy of the NEVPT results was also judged with respect to some reference coupled cluster calculations (CCSD and CCSDR(3)) [110, 111], specifically performed for this study. These computations were carried out with the DALTON program [112], using the same geometry [70]

and ANO+1s1p1d basis set employed for the NEVPT ones. The oscillator strengths for the excited states were calculated with the CASSCF state interaction (CASSI) method [113], using the NEVPT2 and NEVPT3 energy differences. Moreover, for those states subjected to quasi–degenerate NEVPT2 treatment, the transition dipole moments were recomputed using the corrected linear combinations obtained by diagonalization of the QD-NEVPT2 matrix.

3.6.1 Valence–Rydberg mixing

As can be seen in Tab. 3.16, where the CASSCF, QD-NEVPT2 and CCSD values of the $\langle x^2 \rangle$ component of the second moment of the charge distribution for the $\pi \rightarrow \pi^*$ are collected, at the zero order level, the more consistent mixing effects take place among the states of the B_2 and A_2 symmetries. In fact, both the lower–energy $\pi \rightarrow \pi^*$ valence state ($4^1B_2(V)$) and the $n \rightarrow \pi^*$ (2^1A_2) state show too diffuse a character for pure valence states, with values of $\langle x^2 \rangle$ amounting roughly to 39 and 42 a.u. respectively; indeed, the ground state of Thiophene has a value of $\langle x^2 \rangle$ of about 30 a.u. Then, a minor valence–Rydberg mixing can also be detected among the $2^1A_1(V)$ valence state and the $3b_1 \rightarrow 3p_x$ (3^1A_1) and $1a_2 \rightarrow 3d_{xy}$ (4^1A_1) Rydberg states.

Table 3.16: CASSCF, QDNEVPT2 and CCSD $\langle x^2 \rangle$ component of the second moment of the charge distribution (a.u.) for the $\pi \rightarrow \pi^*$ and $n \rightarrow \pi^*$ excited states of Thiophene.

		$\langle x^2 \rangle$			
State	Assignment	CASSCF	SC-QDNEVPT2	PC-QDNEVPT2	CCSD
$2^1A_1(V)$	$\pi \rightarrow \pi^*$	33.57	31.19	30.65	31.26
3^1A_1	$3b_1 \rightarrow 3p_x$	90.13	91.79	91.03	88.12
4^1A_1	$1a_2 \rightarrow 3d_{xy}$	89.02	90.36	90.45	87.01
5^1A_1	$3b_1 \rightarrow 3d_{xz}$	89.80	89.52	69.48	85.15
$6^1A_1(V')$	$\pi \rightarrow \pi^*$	32.65	32.56	63.43	40.91
1^1B_2	$1a_2 \rightarrow 3p_x$	93.17	93.12	93.42	89.91
2^1B_2	$1a_2 \rightarrow 3d_{xz}$	86.76	89.52	89.38	88.06
3^1B_2	$3b_1 \rightarrow 3d_{xy}$	83.88	86.69	81.71	85.34
$4^1B_2(V)$	$\pi \rightarrow \pi^*$	38.81	32.85	32.62	31.55
$5^1B_2(V')$	$\pi \rightarrow \pi^*$	33.85	34.15	40.04	35.99
1^1A_2	$n \rightarrow 3d_{xy}$	81.52	90.89	90.67	
2^1A_2	$n \rightarrow \pi^*$	41.81	32.32	32.89	

The single–state and quasi–degenerate NEVPT excitation energies of the $^1A_1$, $^1B_2$ states, together with the CCSD and CCSDR(3) ones, are reported in Tabs. 3.17

and 3.18 respectively. Instead, in Tab. 3.19 are shown the NEVPT results for the states of A_2 symmetry.

Table 3.17: NEVPT, CCSD and CCSDR(3) vertical transition energies (eV) of the $^1A_1$ excited states of Thiophene.

Method	$\pi \rightarrow \pi^*$	$3b_1 \rightarrow 3p_x$	$1a_2 \rightarrow 3d_{xy}$	$3b_1 \rightarrow 3d_{xz}$	$\pi \rightarrow \pi^*$
CASSCF	5.71	6.36	6.88	7.02	8.06
SC-NEVPT2	5.94	7.17	7.56	7.89	8.00
PC-NEVPT2	5.89	7.18	7.56	7.90	7.86
SC-NEVPT3	5.78	6.97	7.41	7.69	7.94
SC-QDNEVPT2	5.88	7.18	7.55	7.89	8.04
PC-QDNEVPT2	5.80	7.20	7.56	7.89	7.94
CCSD	5.78	7.11	7.53	7.83	7.93
CCSDR(3)	5.70	7.10	7.50	7.81	7.71

Table 3.18: NEVPT, CCSD and CCSDR(3) vertical transition energies (eV) of the $^1B_2$ excited states of Thiophene.

Method	$1a_2 \rightarrow 3p_x$	$1a_2 \rightarrow 3d_{xz}$	$3b_1 \rightarrow 3d_{xy}$	$\pi \rightarrow \pi^*$	$\pi \rightarrow \pi^*$
CASSCF	6.17	6.83	7.01	7.16	8.88
SC-NEVPT2	6.94	7.58	7.85	6.47	8.30
PC-NEVPT2	6.95	7.59	7.86	6.37	8.12
SC-NEVPT3	6.70				8.36
SC-QDNEVPT2	6.94	7.64	7.92	6.34	8.31
PC-QDNEVPT2	6.95	7.69	7.97	6.14	8.14
CCSD	6.84	7.56	7.81	6.23	7.96
CCSDR(3)	6.81	7.54	7.80	6.10	7.85

As is apparent in Tab. 3.17, the application of the QD approach leads to a slight lowering ($\leq$ 0.1 eV) of the single–state NEVPT2 excitation energy of the $2^1A_1(V)$ state, in agreement with the slight reduction observed in its value of $\langle x^2 \rangle$, passing from $\simeq$ 33 (CASSCF) to $\simeq$ 30 a.u. (PC-QDNEVPT2). However, as the CASSCF mixing can be regarded as negligible, the trend of the single–state NEVPT results appears coherent, with the SC-NEVPT3 calculation locating this state at 5.78 eV. A value of 5.80 eV is obtained from the PC-QDNEVPT2 calculation. A good agreement is also achieved with the CC results, where this transition is predicted at 5.78 (CCSD) and 5.70 eV (CCSDR(3)). As can be seen from the results in Tab. 3.17 and from the values of $\langle x^2 \rangle$ reported in Tab. 3.16, the description of the other $^1A_1$ states is essentially not influenced by the application of the QD formalism, with

the only exception of the $6^1A_1(V')$ state at the PC level. Concerning this issue some remarks are needed. Similarly to what we found for Pyrrole [29](section 3.4) and Furan [30] (section 3.5), the ionic character of the higher–energy $^1A_1$ valence state, in addition to its partial nature of double excitation, makes the calculation of this state rather problematic. The difficulties are clearly shown by the difference (0.15-0.2 eV) between the strongly contracted and the partially contracted results. Note that for this state, a remarkable difference, amounting roughly to 0.2 eV, is also obtained from CCSD and CCSDR(3) calculations. So, at the partially contracted level, where the $6^1A_1(V')$ state is computed at significantly lower energy, a quasi degeneracy with the $3b_1 \rightarrow 3d_{xz}$ Rydberg state occurs, with the two states being separated by less than 0.04 eV. The QD formalism, applied at the PC-NEVPT2 level, gives rise to a strong mixing between the two wavefunctions, in such a way that the resulting roots have values of $\langle x^2 \rangle$ amounting to $\simeq$ 69 and $\simeq$ 63 a.u. (values in Tab. 3.16). A similar mixing, even if less pronounced, was also found in the CCSD calculations, where the computed $\langle x^2 \rangle$ are $\simeq$ 85 and $\simeq$ 41 a.u. for the Rydberg and valence state respectively. The SC-NEVPT3 excitation energy of the $6^1A_1(V')$ state is 7.94 eV, in excellent accordance with the value of 7.93 eV obtained from the CCSD calculation.

As above mentioned and shown by the results in Tab. 3.16 and 3.18, the valence–Rydberg mixing effects are more prominent among the $^1B_2$ states. The $4^1B_2(V)$ valence state, mixed at CASSCF level with the 2^1B_2 and 3^1B_2 Rydberg states, after the QD calculation, shows a remarkable reduction ($\simeq$ 6 a.u.) in the value of its $\langle x^2 \rangle$; the recovery of the valence nature is, obviously, followed by the lowering in its excitation energy, which, at the more accurate PC level, reduces from 6.37 to 6.14 eV. In accordance with the PC-QDNEVPT2 result, the CCSDR(3) transition energy of this state is 6.10 eV ($\langle x^2 \rangle \simeq 31$ a.u.), whereas a value of 6.23 eV is attained at CCSD level. Obviously, the opposite behaviour is observed for the two Rydberg states, whose transition energies slightly increase ($\simeq$ 0.1 eV). However, the second moments of the charge distribution, reported in Tab. 3.16, indicate that at the PC level, where the two states are more close in energy, a small mixing occurs between the $3b_1 \rightarrow 3d_{xy}$ Rydberg state and the $5^1B_2(V')$ valence state; as can be seen in Tab. 3.18, however, the effects on the excitation energies are negligible. A small mixing is also found at CCSD level, where the computed values of $\langle x^2 \rangle$ are $\simeq$ 36 and $\simeq$ 85 a.u. for the valence and Rydberg state respectively.

Finally, the QD approach was proved to be important also for the calculation of the two π–type $^1A_2$ states, which appear mixed in the CASSCF description. At the PC level, where the correction is more efficient, the QDNEVPT2 excitation energy (Tab. 3.19) for the valence (Rydberg) state turns out to be about 0.2 eV lower (higher) than that obtained from the single–state calculations. Also, the values of $\langle x^2 \rangle$ recomputed in the correct zero order space (Tab. 3.16) are in accordance with

those typical for pure valence and Rydberg states, being $\simeq 32$ and $\simeq 90$ a.u.

Table 3.19: Single–state and quasi–degenerate NEVPT2 vertical transition energies (eV) of the π–type $^1A_2$ excited states of Thiophene.

Method	$n \rightarrow 3d_{xy}$	$n \rightarrow \pi^*$
CASSCF	9.77	10.07
SC-NEVPT2	10.49	10.13
PC-NEVPT2	10.45	10.04
SC-QDNEVPT2	10.61	10.01
PC-QDNEVPT2	10.64	9.86

An important difference in the spectroscopical features of Thiophene with respect to the analogous hetero–cycles, Pyrrole [29] and Furan [30], is the presence of two low–energy $\pi \rightarrow \sigma^*$ states, one of B_1 symmetry and one of A_2 symmetry, strongly interacting with $3p$ and $3d$ type Rydberg states.

In Tab. 3.20 the values of $\langle x^2 \rangle$ for the σ–type states, the zero order assignments, the CASSCF and single–state NEVPT excitation energies of the first seven excited states of B_1 and A_2 symmetry are listed.

Table 3.20: CASSCF and single–state NEVPT excitation energies (eV) for the σ–type excited states of Thiophene. The CASSCF values of the $\langle x^2 \rangle$ component of the second moment of the charge distribution and the nature of the states are also reported.

	CASSCF			SC-PT2	PC-PT2	SC-PT3
State	Assignment	$\langle x^2 \rangle$	ΔE	ΔE	ΔE	ΔE
1^1B_1	$3b_1 \rightarrow 3s + 1a_2 \rightarrow 3p_y$	51.12	6.76	6.45	6.51	6.24
2^1B_1	$(1a_2 \rightarrow 3p_y + \sigma^*) + 3b_1 \rightarrow 3s$	47.99	6.90	6.50	6.54	
3^1B_1	$3b_1 \rightarrow 3p_z + 1a_2 \rightarrow 3d_{yz}$	49.30	7.27	7.06	7.11	6.82
4^1B_1	$1a_2 \rightarrow 3d_{yz} + \sigma^*$	45.64	7.44	6.97	7.00	
5^1B_1	$3b_1 \rightarrow 3d_{a_1}$	54.23	7.88	7.60	7.64	7.38
6^1B_1	$3b_1 \rightarrow 3d_{a_1}$	72.12	7.96	7.50	7.48	7.34
7^1B_1	$1a_2 \rightarrow \sigma^* + 3d_{yz}$	34.53	8.53	7.16	7.12	
1^1A_2	$1a_2 \rightarrow 3s$	51.26	6.48	6.10	6.15	5.90
2^1A_2	$1a_2 \rightarrow 3p_z$	50.18	7.03	6.77	6.82	6.55
3^1A_2	$3b_1 \rightarrow 3p_y + 3d_{yz} + \sigma^*$	43.48	7.12	6.64	6.65	
4^1A_2	$1a_2 \rightarrow 3d_{a_1}$	63.22	7.49	7.22	7.27	7.01
5^1A_2	$1a_2 \rightarrow 3d_{a_1}$	63.33	7.54	7.17	7.20	6.99
6^1A_2	$3b_1 \rightarrow 3d_{yz} + 3p_y + \sigma^*$	46.72	7.69	7.23	7.24	
7^1A_2	$3b_1 \rightarrow \sigma^* + 3d_{yz}$	38.20	8.48	7.53	7.50	

As can be seen, for the $^1B_1$ states, apart from a slight mixing between the $3b_1 \rightarrow 3s$ and $1a_2 \rightarrow 3p_y$ as well as the $3b_1 \rightarrow 3p_z$ and $1a_2 \rightarrow 3d_{yz}$ Rydberg states, the

most significant valence–Rydberg interaction takes place between the $1a_2 \rightarrow \sigma^*$ and the $1a_2 \rightarrow 3d_{yz}$ states; moreover, also the $1a_2 \rightarrow 3p_y$ state exhibits a partial valence character. The CASSCF second moments for the Rydberg states are $\simeq 48$ ($3p$) and $\simeq 45$ a.u ($3d_{yz}$), where a value of $\simeq 34$ a.u. is attained for the 7^1B_1 state.
An analogous situation occurs among the states of A_2 symmetry, where the three states which mix are again the 7^1A_2, having a σ^* dominant character, and the two $3b_1 \rightarrow 3d_{yz}$ and $3b_1 \rightarrow 3p_y$ Rydberg states; the computed $\langle x^2 \rangle$ are 38.20, 46.72 and 43.48 a.u. respectively.
The QDNEVPT2 calculations were carried out on five states of B_1 symmetry (1-4^1B_1 and 7^1B_1) and on three states of A_2 symmetry (3^1A_2, 6^1A_2 and 7^1A_2). The third order computations were performed only for those states not involved in the valence–Rydberg mixing.

After the application of the QD formalism, the interpretation of the states in terms of Rydberg $3p_y$, $3d_{yz}$ and valence σ^* states turn out to be rather problematic. However, on the basis of the evaluation of the values of $\langle x^2 \rangle$ in the corrected zero order space, some considerations, concerning the valence or Rydberg nature, are possible. In addition, further information has been obtained by computing the natural orbitals for each eigenstate of the QD-PT matrix in order to build the CASCI molecular orbitals in the corrected zero order space. In Tab. 3.21 the recomputed values of $\langle x^2 \rangle$ and the QDNEVPT2 excitation energies are reported. The CC results for all the σ–type states are, instead, listed in Tab. 3.22.

Table 3.21: Values of the $\langle x^2 \rangle$ component of the second moment of the charge distribution (a.u.) and QDNEVPT2 excitation energies for some σ–type excited states of Thiophene.

	SC-QDNEVPT2			PC-QDNEVPT2		
State	$\langle x^2 \rangle$	Assignment	ΔE	$\langle x^2 \rangle$	Assignment	ΔE
1^1B_1	36.49	$1a_2 \rightarrow \sigma^* + 3p_y$	6.33	32.77	$1a_2 \rightarrow \sigma^* + 3p_y$	6.10
2^1B_1	44.48	$1a_2 \rightarrow 3p_y + \sigma^* + 3d_{yz}$	6.38	51.66	$3b_1 \rightarrow 3s$	6.52
3^1B_1	51.15	$3b_1 \rightarrow 3s$	6.47	48.17	$1a_2 \rightarrow 3p_y$	6.86
4^1B_1	49.34	$3b_1 \rightarrow 3p_z$	7.07	49.30	$3b_1 \rightarrow 3p_z$	7.14
5^1B_1	45.19	$1a_2 \rightarrow 3d_{yz} + \sigma^*$	7.45	46.61	$1a_2 \rightarrow 3d_{yz}$	7.65
1^1A_2	33.75	$3b_1 \rightarrow \sigma^*$	6.46	31.14	$3b_1 \rightarrow \sigma^*$	6.22
2^1A_2	48.02	$3b_1 \rightarrow 3p_y + 3d_{yz}$	7.19	49.79	$3b_1 \rightarrow 3p_y$	7.25
3^1A_2	46.27	$3b_1 \rightarrow 3d_{yz} + 3p_y + \sigma^*$	7.75	47.58	$3b_1 \rightarrow 3d_{yz}$	7.94

First of all, some important remarks concern the different behaviour of the two QDNEVPT2 variants. Indeed, as can be observed in Tab. 3.21, while the mixing among the $3p_y$, $3d_{yz}$ and σ^* states persists at the strongly contracted level, the nature

of the states appear to be in good measure pure after the PC calculations; only the $^1B_1$ ($1a_2 \rightarrow \sigma^*$) state shows a slight Rydberg character. The different nature of the states obtained from the SC and PC calculations is, obviously, the reason for the remarkable deviations observed between the SC-QDNEVPT2 and PC-QDNEVPT2 excitation energies. Note that these deviations can be, instead, regarded as negligible (0.07 eV at most) for the $3b_1 \rightarrow 3s$ and $3b_1 \rightarrow 3p_z$ Rydberg states. At the SC level, the excitation energies of the Rydberg states, which still have a partial valence character, are significantly lower (even $\simeq 0.3$ eV for the $1a_2 \rightarrow 3p_y$ state) than those computed at PC level; obviously, too high excitation energies are, instead, obtained for the two valence states.

Table 3.22: CCSD and CCSDR(3) excitation energies (eV) for the σ–type excited states of Thiophene. The $\langle x^2 \rangle$ component of the second moment of the charge distribution and the nature of the states are also reported.

			CCSD	CCSDR(3)
State	Assignment	$\langle x^2 \rangle$	ΔE	ΔE
1^1B_1	$1a_2 \rightarrow \sigma^*$ mix.	36.41	6.28	6.20
2^1B_1	$3b_1 \rightarrow 3s$	48.84	6.40	6.36
3^1B_1	$1a_2 \rightarrow 3p_y$ mix.	44.94	6.85	6.81
4^1B_1	$3b_1 \rightarrow 3p_z$	47.79	7.01	6.99
5^1B_1	$3b_1 \rightarrow 3d_{a_1}$	55.68	7.46	7.43
6^1B_1	$3b_1 \rightarrow 3d_{a_1}$	61.64	7.52	7.50
7^1B_1	$1a_2 \rightarrow 3d_{yz}$ mix.	45.06	7.60	7.55
1^1A_2	$1a_2 \rightarrow 3s$	49.15	6.10	6.05
2^1A_2	$3b_1 \rightarrow \sigma^*$ mix.	32.11	6.31	6.26
3^1A_2	$1a_2 \rightarrow 3p_z$	48.97	6.78	6.74
4^1A_2	$3b_1 \rightarrow 3p_y$	53.47	7.14	7.11
5^1A_2	$1a_2 \rightarrow 3d_{a_1}$	46.94	7.18	7.14
6^1A_2	$1a_2 \rightarrow 3d_{a_1}$	63.73	7.23	7.19
7^1A_2	$3b_1 \rightarrow 3d_{yz}$ mix.	46.14	7.81	7.80

Although the $1a_2 \rightarrow \sigma^*$ state still shows a small $3p$ character, the PC-QDNEVPT2 approach brings about a remarkable decrease ($\simeq 1$ eV) with respect to the single–state excitation energy of the 7^1B_1 state, which, at the CASSCF level, is the state with the strongest valence nature (see Tab. 3.20); indeed, the transition energy changes from 7.12 to 6.10 eV. At the strongly contracted level as well as at CCSD level, this state is computed with a value of $\langle x^2 \rangle$ of $\simeq 36$ a.u., that is somewhat diffuse for a pure valence state. As a consequence of this partial Rydberg character the SC-QDNEVPT2 and CC excitation energies turn out to be higher than the PC one, being 6.33 and 6.30 eV (CCSDR(3)) respectively. On the contrary, both the

$3b_1 \rightarrow 3s$ and $3b_1 \rightarrow 3p_z$ Rydberg states are essentially not affected by the application of the QD approach: their values of $\langle x^2 \rangle$ remain the same as computed at CASSCF level and hence the single–state and quasi–degenerate excitation energies are very similar.

As shown in Tab. 3.20, the third order calculations, for both these states, bring about a lowering in the excitation energies slightly less than 0.3 eV, locating the states at 6.24 eV ($3s$) and 6.82 eV ($3p_z$). For these two states, a good accordance is also attained with the CC results (Tab. 3.22), that turn out to be only $\simeq 0.15$ eV higher than the SC-NEVPT3 ones. At PC-QDNEVPT2 level, the $1a_2 \rightarrow 3p_y$ is computed at 6.86 eV, in remarkable accordance with the CC results, that locate this state at 6.85 (CCSD) and 6.81 eV (CCSDR(3)). Then, at the PC level, the $1a_2 \rightarrow 3d_{yz}$ is calculated to lie at 7.65 eV, about 0.7 eV above the value computed in the single–state approach for the 4^1B_1 state (see Tab. 3.20). Very similar transition energies were provided by the CC calculations, where the state is located at 7.60 and 7.55 eV (respectively CCSD and CCSDR(3) values in Tab. 3.22).

Similar remarks can be made for the three $^1A_2$ states, which, after the PC-QDNEVPT2 treatment, result in a pure valence state ($\langle x^2 \rangle \simeq 31$ a.u.) and two pure Rydberg $3p_y$ and $3d_{yz}$ states. At PC-QDNEVPT2 level, the $3b_1 \rightarrow \sigma^*$ transition is predicted at 6.22 eV in very good agreement with the CC values (see Tab. 3.22), where the state is located at 6.31 (CCSD) 6.26 eV (CCSDR(3)), with a value of $\langle x^2 \rangle$ of 32.11 a.u. Instead, the two Rydberg states are shifted at higher energy with respect to single–state excitation energies: the $3b_1 \rightarrow 3p_y$ state is computed at 7.25 eV (PC-QDNEVPT2), with an $\langle x^2 \rangle$ of $\simeq 49$ a.u. and the $3b_1 \rightarrow 3d_{yz}$ excitation in predicted at 7.94 eV (PC-QDNEVPT2) with an $\langle x^2 \rangle$ of $\simeq 47$ a.u. The CC excitation energies, reported in Tab. 3.22, are only slightly lower ($\simeq 0.15$) than the PC-QDNEVPT2 ones. Note that at the single–state level, the two states were calculated at 6.65 and 7.50 eV respectively (PC-NEVPT2 values in Tab. 3.20). Finally, as can be seen in Tab. 3.20, for the other four Rydberg states, not involved in the CASSCF mixing, the application of the SC-NEVPT3 correction produces a small (0.15-0.25 eV) and regular lowering in the second order excitation energies. Comparable transition energies, even if always slightly higher than the SC-NEVPT3 ones, were obtained from the CC calculations (see values in Tab. 3.22).

3.6.2 The VUV absorption spectrum

In contrast to the large number of theoretical works dedicated to the absorption spectra of Pyrrole and Furan, surprisingly few *ab initio* studies on the electronic spectrum of Thiophene have been published. Indeed, the first CI study by Bendazzoli *et al.*, published in 1978 [114], was followed only by three high–level *ab initio* studies,

namely, a single–state CASPT2 study in 1993 [115], a MRCI investigation in 1999 [67] and, finally, a SAC-CI work in 2001 [116]. In addition, some TD-DFT [117] and ADC(2) [118] results have also been presented. Although there is, overall, a good agreement in the assignments of the four lowest–energy $\pi \rightarrow \pi^*$ states, a number of inconsistencies still exists in the interpretation of some Rydberg states.

The most accurate NEVPT excitation energies and the corresponding oscillator strengths, which are used to discuss the interpretation of the spectrum, are shown in Tab. 3.9, together with the CCSDR(3) results and those of the previous theoretical studies [67, 115–117].

Energy range 5-6.5 eV

In this energy range is located the first absorption region, which is composed of the two historical A and B bands. The first system (A band), whose valence $\pi \rightarrow \pi^*$ nature was experimentally assessed on the basis of the comparison of gas phase results with condensed–phase measurements [114,123–125], begins at 5.16 eV with the maximum at 5.39 eV. Furthermore, in the magnetic circular dichroism spectrum (MCD) of Thiophene in hexane, two bands with opposite signs in their B-values [126–128] were detected at 5.27 and 5.64 eV, confirming the presence of two $\pi \rightarrow \pi^*$ transitions in the low–energy tail of the first VUV band. On the basis of PPP calculations [126] and *ab initio* prediction of the B-values [114], the lower–energy peak was attributed to the $^1A_1(V)$ state. Our most accurate results predict the vertical transitions to the $^1A_1(V)$ and $^1B_2(V)$ states to be 5.78 (SC-NEVPT3) and 6.14 eV (PC-QDNEVPT2) respectively; the computed oscillator strengths are 0.130 ($^1A_1(V)$) and 0.107 ($^1B_2(V)$). Taking into account that for these aromatic molecules, the vertical transition and the observed maximum of the band may differ significantly, with the former being even 0.2 eV [83, 107, 108] above the latter, our present results confirm the traditional valence interpretation of the A band. The CCSDR(3) excitation energies are in remarkable accordance with the NEVPT ones, locating the $^1A_1(V)$ state at 5.70 eV and the $^1B_2(V)$ transition at 6.10 eV, with very similar intensities (0.082 and 0.080 respectively). The present results also agree with those computed in the MRCI study by Palmer *et al.* [67], whereas larger deviations ($\simeq$ 0.4 eV) are observed with the CASPT2 [115] and SAC-CI [116] values.

Then, the weak fine structure near 6 eV [67,95,129,130], known as the B band, is interpreted as Rydberg in nature, principally arising from the symmetry forbidden $1a_2 \rightarrow 3s$ state; this system indeed does not appear in the condensed–phase spectrum [114, 123, 124], where the Rydberg states are thought to play a negligible rôle. The $1a_2 \rightarrow 3s$ state ($^1A_2$) is computed, at SC-NEVPT3 level, at 5.90 eV, in perfect accordance with experiments and with the CASPT2 result [115] (5.93 eV); slightly

Table 3.23: NEVPT and CC vertical transition energies (eV) and oscillator strengths (within parentheses) of the singlet excited states of Thiophene compared with the previous theoretical results.

		NEVPT[a]							
State	Nature	SC3	PC-QD	CCSDR(3)[a,b]	SAC-CI [116]	MRCI [67]	CASPT2 [115]	TD-DFT [117]	Exp.[d]
$^1A_1(V)$	$\pi \rightarrow \pi^*$	5.78 (0.130)	5.80 (0.153)	5.70 (0.082)	5.41 (0.091)	5.69 (0.119)	5.33 (0.089)	5.64 (0.058)	5.39
$^1A_2$	$1a_2 \rightarrow 3s$	5.90		6.05	5.70	5.78	5.93	5.94	5.93
$^1B_1$	$1a_2 \rightarrow \sigma^*$		6.10 (0.004)	6.30 (0.015)	5.87 (0.011)	6.41	6.20[c] (0.002)[c]	5.67 (0.005)	
$^1B_2(V)$	$\pi \rightarrow \pi^*$		6.14 (0.107)	6.10 (0.080)	5.72 (0.113)	6.00 (0.154)	5.72 (0.070)	5.65 (0.074)	5.64
$^1A_2$	$3b_1 \rightarrow \sigma^*$		6.22	6.28	6.03	6.85	6.26[c]	6.04	
$^1B_1$	$3b_1 \rightarrow 3s$	6.24 (0.000)	6.52 (0.001)	6.36 (0.002)	6.12 (0.000)	6.33 (0.000)	6.23 (0.000)	6.32 (0.002)	
$^1A_2$	$1a_2 \rightarrow 3p_z$	6.55		6.74	6.41	7.03	6.58	6.59	6.60
$^1B_2$	$1a_2 \rightarrow 3p_x$	6.70 (0.040)	6.95 (0.045)	6.81 (0.032)	6.41 (0.038)	7.02 (0.034)	6.56 (0.030)	6.74 (0.023)	6.60
$^1B_1$	$1a_2 \rightarrow 3p_y$		6.86 (0.021)	6.81 (0.022)	6.47 (0.016)	6.39 (0.000)	6.30 (0.030)	6.72 (0.017)	6.60
$^1B_1$	$3b_1 \rightarrow 3p_z$	6.82 (0.025)	7.14 (0.024)	6.99 (0.024)	7.17 (0.019)	6.73 (0.029)	6.83 (0.020)		6.7-7.0
$^1A_1$	$3b_1 \rightarrow 3p_x$	6.97 (0.022)	7.20 (0.051)	7.10 (0.041)	6.73 (0.065)	7.31 (0.021)	6.76 (0.015)		6.7-7.0
$^1A_2$	$3b_1 \rightarrow 3p_y$		7.25	7.11	6.89	6.39	6.35		6.7-7.0
$^1A_2$	$1a_2 \rightarrow 3d_{a_1}$	6.99		7.14	6.73	7.93	6.97	6.91	
$^1A_2$	$1a_2 \rightarrow 3d_{a_1}$	7.01		7.19	6.75	7.85	7.08	7.07	
$^1A_1$	$1a_2 \rightarrow 3d_{xy}$	7.41 (0.002)	7.55 (0.000)	7.50 (0.013)	7.08 (0.018)	7.93 (0.001)	7.23 (0.001)	7.45 (0.037)	7.33

Table 3.9: Continued

State	Nature	NEVPT[a] SC3	NEVPT[a] PC-QD	CCSDR(3)[a,b]	SAC-CI [116]	MRCI [67]	CASPT2 [115]	TD-DFT [117]	Exp.[d]
$^1B_1$	$1a_2 \rightarrow 3d_{yz}$		6.65 (0.000)	7.55 (0.000)	7.15 (0.000)		7.24 (0.001)	7.32 (0.000)	
$^1B_2$	$1a_2 \rightarrow 3d_{xz}$		7.69 (0.001)	7.54 (0.002)	7.12 (0.003)	8.11 (0.000)	7.28 (0.001)	7.43 (0.014)	
$^1B_1$	$3b_1 \rightarrow 3d_{a_1}$	7.34 (0.001)		7.43 (0.000)	7.21 (0.000)	8.18	7.37 (0.000)		
$^1B_1$	$3b_1 \rightarrow 3d_{a_1}$	7.38 (0.001)		7.50 (0.000)	7.14 (0.000)	8.26	7.67 (0.001)		
$^1A_1$	$3b_1 \rightarrow 3d_{xz}$	7.69 (0.000)	7.89 (0.077)	7.81 (0.017)	7.47 (0.034)	8.05	7.57 (0.000)		
$^1A_2$	$3b_1 \rightarrow 3d_{yz}$		7.94	7.80		7.59	7.64		7.95
$^1B_2$	$3b_1 \rightarrow 3d_{xy}$		7.97 (0.129)	7.80 (0.007)	7.46 (0.024)	7.92	7.53 (0.002)		7.95
$^1A_1(V')$	$\pi \rightarrow \pi^*$	7.94 (0.238)	7.94 (0.069)	7.71 (0.294)	7.32 (0.361)	7.91 (0.429)	6.69 (0.185)	7.35 (0.121)	7.05
$^1B_1$	$n \rightarrow \pi^*$	8.26 (0.034)			7.86 (0.000)	8.83	7.77 (0.033)		
$^1B_2(V')$	$\pi \rightarrow \pi^*$	8.36 (0.412)	8.14 (0.276)	7.85 (0.105)	7.40 (0.120)	8.10 (0.131)	7.32 (0.392)	7.34 (0.071)	7.50
$^1A_2$	$n \rightarrow \pi^*$		9.86			10.34	9.69		
$^1A_2$	$n \rightarrow 3d_{xy}$		10.64			10.75	10.27		

[a] This work

[b] The reported oscillator strengths were computed at CCSD level

[c] Values from Ref. [117]

[d] Values from Refs. [67, 94, 119–122]

lower excitation energies were instead obtained from the MRCI [67] (5.78 eV) and SAC-CI [116] (5.70 eV) calculations. In the CCSDR(3) computations this transition is instead obtained at 6.10 eV. Our results, in accordance with the SAC-CI [116], MRCI [67], CASPT2 [115] and TD-DFT [117], also predict the $3b_1 \rightarrow 3s$ Rydberg state to belong to the B band, with a SC-NEVPT3 vertical excitation energy of 6.24 eV. Moreover, on the basis of the present calculations, two other valence $\pi \rightarrow \sigma^*$ states, partially mixed with the $3p_y$ and $3d_{yz}$ states, should be attributed to this band: the $1a_2 \rightarrow \sigma^*$ state ($^1B_1$) is computed at 6.10 eV (PC-QDNEVPT2) with an $\langle x^2 \rangle$ of $\simeq 32.5$ a.u. and a negligible oscillator strength (0.004) and the $3b_1 \rightarrow \sigma^*$ state ($^1A_2$) is instead located at 6.22 eV (PC-QDNEVPT2) with an $\langle x^2 \rangle$ of $\simeq 31$ a.u. Very similar excitation energies were obtained from the CC calculations, where the states are computed at slightly higher energy (6.30 and 6.28 eV respectively) and with a slightly more diffuse character (36.41 and 32.11 a.u. respectively). This partial Rydberg ($3p$) nature of the $^1B_1$ state justifies the greater oscillator strength (0.015) computed at CC level. In the SAC-CI study [116] these two states are calculated at 5.87 ($^1B_1$) and 6.03 eV ($^1A_2$) and the corresponding values of second moments of the charge distribution are $\simeq 35$ and $\simeq 32$ a.u. Values of 6.41 ($^1B_1$) and 7.85 eV ($^1A_2$) are reported in the MRCI work [67] and, finally, excitation energies of 6.20 ($^1B_1$) and 6.26 eV ($^1A_2$) have been obtained at CASPT2 level [117].

Energy range 6.5-7.8 eV

This spectral region, known as C Band, is considered as principally originated from the couple of higher–energy $\pi \rightarrow \pi^*$ states [67,77]: $^1A_1(V')$ and $^1B_2(V')$ in increasing energetical order. However, the shape of the spectrum in this region is complicated by a number of Rydberg states, which are expected to appear both at the low and high energy tails of the C band. In the Electron Energy Loss (EEL) spectrum the maximum appears at 7.05 eV and it was attributed to Rydberg ($3b_1 \rightarrow 3p$) and/or to valence ($^1B_2(V')$) excitations [67]. The rising side, with a maximum detected at 6.60 eV, was, instead, assigned to a $1a_2 \rightarrow 3p$ state [67,77].

The best NEVPT results locate the vertical transitions to the two higher–energy $\pi \rightarrow \pi^*$ states at 7.94 ($^1A_1(V')$) and 8.14 eV ($^1B_2(V')$), whereas excitation energies of 7.71 and 7.85 were obtained from the CCSDR(3) calculations. In comparison to the experimental assignments, the NEVPT and CCSDR(3) transition energies turn out to be slightly higher, confirming the difficulty, already discussed for the analogous hetero–cycles in Refs. [29,30], of obtaining accurate theoretical results for these ionic high–energy $\pi \rightarrow \pi^*$ states. As is apparent in Tab. 3.9, for both these valence states, dissimilar oscillator strengths were obtained at SC3 and PC-QD level; this is not surprising considering that, above all for the $^1A_1(V')$ state, a remarkable mixing

with the less intense Rydberg states was found in the quasi–degenerate NEVPT2 calculations (see subsection 3.6.1). Very similar excitation energies are reported in the MRCI study [67], where the $^1A_1(V')$ state is computed at 7.91 eV and the $^1B_2(V')$ one at 8.10 eV. On the contrary, larger differences (up to 1 eV) are observed between the NEVPT and the CASPT2 [115] results, which locate the two states at 6.69 ($^1A_1(V')$) and 7.32 eV ($^1B_2(V')$).

The first three members of the $1a_2 \rightarrow 3p$ Rydberg series have been computed to have vertical excitation energies of 6.55 (p_z), 6.70 (p_x) and 6.86 eV (p_y), in accordance with the experimental assignments [67, 77] of the structure below 7 eV to a $3p$-type state converging to IP_1 (8.872 eV). A good agreement (within 0.2 eV) is attained with the CCSDR(3) excitation energies, whereas significant discrepancies are evident among those of the previous works. Apart from the MRCI results [67], which seem to overestimate the excitation energies of both the $3p_z$ and $3p_x$ states, the main difficulties concern the calculation of the σ–type $3p_y$ state. The SAC-CI [116], MRCI [67] and single–state CASPT2 [115] excitation energies are 6.47, 6.39 and 6.30 eV, which are remarkably lower than the best NEVPT and CC values. On the contrary, a value of 6.72 eV was obtained from the TD-DFT computations [117]. The explanation for such too low excitation energies can be attributed to the partial valence σ^* character of the $3p_y$ state. The SAC-CI $\langle x^2 \rangle$ of this state is $\simeq$ 43 a.u. [116], where a value of $\simeq$ 47 is reported in the CASPT2 work [115]. Note that the single–state PC-NEVPT2 excitation energy of this state, partially mixed with the $3d_{yz}$ and σ^* states, was 6.54 eV (Tab. 3.20 in subsection 3.6.1), noticeably lower than the corresponding QD value but much more similar to the SAC-CI and single–state CASPT2 results.

On the basis of our accurate NEVPT calculations, also the $3p$ components of the second Rydberg series (R′) are expected to belong to the C Band, with vertical excitation energies of 6.82 ($3p_z$), 6.97 ($3p_x$) and 7.25 eV ($3p_y$); the CCSDR(3) computations locate the states at 6.99, 7.10 and 7.11 eV respectively. Again, the valence–Rydberg mixing seems to be the reason for the strong differences in the computed transition energies of the $3b_1 \rightarrow 3p_y$ state.

The five members of the $1a_2 \rightarrow 3d$ Rydberg series are computed to lie in the range between $\simeq$ 7 and $\simeq$ 7.7 eV, on the high–energy tail of the C Band, with a very low intensity. The best NEVPT results are 6.99 and 7.01 eV, for the two quasi–degenerate $3d_{a_1}$ states and 7.41 ($3d_{xy}$), 7.65 ($3d_{yz}$) and 7.69 eV ($3d_{xz}$) for the others. As can be seen (Tab. 3.9), the CCSDR(3) excitation energies fully agree with the NEVPT results, with differences not exceeding 0.2 eV. On the contrary, remarkably dissimilar values (up to $\simeq$ 1 eV) have been obtained in the previous *ab initio* studies.

Finally, on the higher energy shoulder of this band, the present results locate also the first three components of the $3b_1 \rightarrow 3d$ Rydberg series, whose NEVPT excitation energies are 7.34 and 7.38 eV for the two $3d_{a_1}$ type states and 7.69 eV for

the $3b_1 \rightarrow 3d_{xz}$ state; however, there are not available experimental assignments for this region of the spectrum. As already pointed out, the larger oscillator strength obtained at PC-QD level for the $3b_1 \rightarrow 3d_{xz}$ state, with respect to that computed at CC level as well as those reported in the other studies, has to be ascribed to the mixing with the strong valence transition (subsection 3.6.1).

Energy range 7.8-10 eV

As suggested by some previous experimental [67, 77, 129] and theoretical works [67, 116], the region between 7.8-8.8 eV is dominated by excitations to Rydberg states. Since the present study is restricted to the computations of the only $3l$ Rydberg states, the experimental assignments of the higher components of the two Rydberg series will be left out (see Refs. [67, 116] for a detailed discussion).

Palmer *et al.* [67], on the basis of their joint experimental and theoretical work, assigned the peak at 7.95 eV to a $3b_1 \rightarrow 3d$ state. The NEVPT results fully confirm this assignment, computing two components of the $3d'$ series near 7.95 eV: the dipole–forbidden $3b_1 \rightarrow 3d_{yz}$ transition is predicted to be located at 7.94 eV and the $3b_1 \rightarrow 3d_{xy}$ state at 7.97 eV, with an oscillator strength of 0.129, due to the interaction with the strong $^1B_2(V')$ transition. In good agreement with the NEVPT results, both states are calculated at 7.80 eV at CCSDR(3) level. On the contrary, significantly lower values are reported in the CASPT2 study [115], where the states are given at 7.64 ($3d_{yz}$) and 7.53 eV ($3d_{xy}$).

Up to now, there is no direct experimental evidence of excitations from the lone pair orbital on the sulfur atom to π^* orbitals. However, the two lowest–energy $n \rightarrow \pi^*$ states are expected to be located in this energy region, completely hidden by intense $\pi \rightarrow \pi^*$ transitions. Our results predict the two states at 8.26 ($^1B_1$) and 9.86 eV ($^1A_2$); in the MRCI study [67] they are computed at 8.83 ($^1B_1$) and 10.34 eV ($^1A_2$) and, finally, at 7.77 ($^1B_1$) and 9.69 eV ($^1A_2$) in the CASPT2 work [115]. A Rydberg state $n \rightarrow 3d_{xy}$ has also been detected at 10.64 eV; a similar excitation energy (10.75 eV) is reported by Palmer *et al.* [67], whereas a value of 10.27 eV was obtained by Serrano-Andrés *et al.* [115].

Chapter 4

The vertical electronic spectrum of Free–Base Porphin

4.1 The UV spectrum of free-base porphin

Due to their crucial rôle in a great deal of biological phenomena, such as the photosynthesis and the oxygen absorption and transport processes, the photochemical and photophysical properties of the porphyrins have been extensively studied [131–133]. Particular attention has been obviously paid to the experimental and theoretical investigation of the electronic spectrum of free base porphin (FBP), the basic building block of the porphyrins and related systems (Fig. 4.1). Since the FBP has become tractable for correlated theoretical methods, a large number of studies has been published, among which we quote the most recent SAC-CI [134–136], STEOM-CC [137, 138], MRPT [139, 140], MRMP [141] and, finally, TD-DFT [132, 142–145] calculations. Certainly, FBP, with its valence π system composed of 24 orbitals and 26 electrons, represents a severe challenge for highly accurate *ab initio* calculations, at the level, for instance, of coupled cluster or multireference perturbation theory and despite the large number of published studies some spectral assignments are still debated.

The most investigated portion of the absorption spectrum extends from $\simeq 2$ to $\simeq 5.5$-6.0 eV and is characterized by three principal regions [146–148]. The lowest–energy band (1.98-2.42 eV), the so–called Q band, is composed of two peaks, designated, according to their polarization, as Q_x and Q_y bands. The most intense absorption region, known as Soret Band (or B band) is located in the range between 3.13 and 3.33 eV and a shoulder on its high–energy tail is instead called N band (3.65 eV). Finally, two weak and broad peaks (L and M bands) appear at 4.25 and 5.50 eV.

The traditional interpretation of the first two bands (Q and B) is based on the "four–

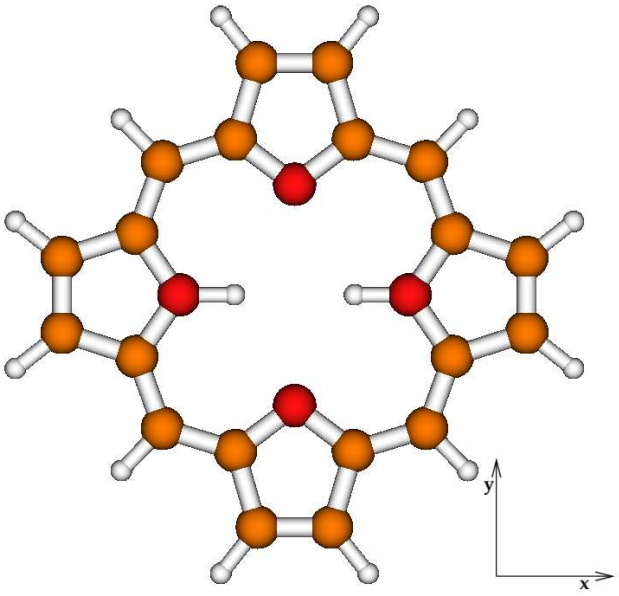

Figure 4.1: Molecular structure of Free Base Porphin (FBP)

orbital model" introduced by Gouterman and co–workers [149–151] in the 1960's. According to this model, the low-energy region of the spectrum can be accounted for in terms of single excitations from the two highest occupied MOs ($5b_{1u}$ and $2a_u$ in the D_{2h} symmetry group) to the two lowest unoccupied MOs ($4b_{2g}$ and $4b_{3g}$) (Figure 4.2). So, if the molecule is placed in the xy plane with the x axis passing along the pyrrolic hydrogens, the x and y components of the Q band should be ascribed to the 1^1B_{3u} and 1^1B_{2u} states respectively; the 2^1B_{3u} and 2^1B_{2u} transitions are instead responsible for the B band. Although Gouterman's model holds for the interpretation of the Q band, it has proved to fail for the the B band, where excitations from the lower b_{1u} orbitals play a non negligible rôle.

4.2 Computational approach

The geometry of the ground state of FBP was optimized at B3LYP/6-31G* level, imposing D_{2h} symmetry, which, on the basis of previous theoretical calculations [152,153], was shown to be the most stable one. Following the convention adopted in most previous theoretical works, the molecule has been placed in the xy plane with the two internal hydrogens along the x axis (Fig. 4.1). All the calculations were carried out with a 6-31G* basis set [55], consisting of 364 basis functions. The zero order description was attained using two different active spaces, named CAS(4/4) and CAS(14/13), where the notation (m/n) indicates, as usual, m active electrons

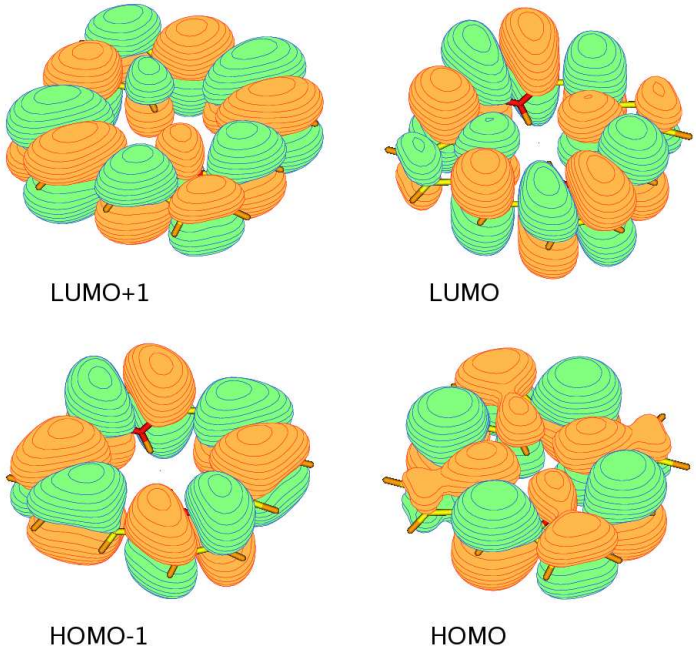

Figure 4.2: HOMO ($2a_u$), HOMO-1 ($5b_{1u}$), LUMO ($4b_{3g}$) and LUMO+1 ($4b_{2g}$) MOs of Free Base Porphin

and n active orbitals. In all the calculations, the 24 $1s$ orbitals were kept frozen at the CASSCF level.

Table 4.1: Active spaces, basis set and number of states used in the CASSCF calculations.

Basis set	Active Space	Composition[a]	Number of states	
			B_{3u}	B_{2u}
6-31G*	CAS(4/4)[b]	$5b_{1u}$,$4b_{2g}$,$4b_{3g}$,$2a_u$	2	2
	CAS(14/13)[c]	3-$5b_{1u}$,3-$6b_{2g}$,3-$6b_{3g}$,1-$2a_u$	4	4

[a] At the SCF level the ground state electronic configuration is $20a_g 17b_{3u} 17b_{2u} 14b_{1g} 5b_{1u} 3b_{2g} 3b_{3g} 2a_u$

[b] Single–state CASSCF calculations

[c] State–averaged CASSCF calculations

The detailed composition of the two active spaces is given in Tab. 4.1, where the number of the computed states is also reported. In the CAS(4/4) calculations the zero order wavefunction was obtained from single–root CASSCF calculations, whereas with the CAS(14/13) space, state–averaged CASSCF optimizations were performed. The excitation energies were obtained with respect to the corresponding

ground state 1^1A_{1g}, which was calculated both for the CAS(4/4) and CAS(14/13) spaces.

4.3 NEVPT results

In Tab. 4.2 the CASSCF and NEVPT2 excitation energies are gathered and compared with those computed in the most recent theoretical studies; the experimental data are also reported.

Table 4.2: Vertical excitation energies of the first four excited states of B_{3u} and B_{2u} symmetries of free base porphin compared with other theoretical results and experimental data.

Method	Excited States							
	1^1B_{3u}	1^1B_{2u}	2^1B_{3u}	2^1B_{2u}	3^1B_{3u}	3^1B_{2u}	4^1B_{3u}	4^1B_{2u}
CAS(4/4)								
CASSCF	3.48	3.71	5.08	5.12				
SC-NEVPT2	2.05	2.53	3.25	3.33				
PC-NEVPT2	2.04	2.51	3.22	3.30				
CAS(14/13)								
CASSCF	3.12	3.80	4.72	5.22	5.74	6.15	7.52	6.27
SC-NEVPT2	2.21	2.76	3.49	3.62	4.10	4.40	4.93	4.47
PC-NEVPT2	2.05	2.56	3.30	3.35	3.84	4.13	4.50	4.10
Previous works								
CASPT2 [139]	1.63	2.11	3.12	3.08	3.53	3.42	4.04	3.96
MRPT2 [140]	1.73	2.25	2.96	3.02				
SAC-CI [135]	1.75	2.23	3.56	3.75	4.24	4.52	5.45	5.31
STEOM-CC [138]	1.72	2.61	3.66	3.77	4.28	4.67	5.38	5.26
TD-DFT [144]	2.16	2.29	2.98	3.01	3.47	3.41	3.76	3.77
TD-DFT [132]	2.27	2.44	3.33	3.41	3.61	3.56	3.89	3.89
Expt. values								
	1.98-2.02[a]	2.33-2.42[a]	3.13-3.33[b]	3.13-3.33[b]	3.65[c]		4.25[c]	
Assignment	Q_x	Q_y	B_x	B_y	N		L	

[a] Refs. [148, 154, 155]
[b] Refs. [146, 148, 155]
[c] Ref. [148]

Before discussing in detail the interpretation of the spectrum, some general remarks are possible. First of all, contrary to the trend observed in the results of the other *ab initio* methods [135, 138–140], which, with the exception of the TD-DFT calculations [132,144], seem to overestimate the correlation energy of the 1^1B_{3u} state with respect to the ground state, the NEVPT2 excitation energies turn out to be slightly higher than the experimental values; a similar behaviour is also noticed for the 1^1B_{2u} state. Also, while a perfect accordance, with differences not exceeding 0.03

eV, can be observed between the SC and PC transition energies in the CAS(4/4) calculation, significant deviations are found using the larger active space. The different behaviour in the second order correction between the two NEVPT variants, can be understood considering the increasing accuracy of the PC approach, involving a much larger number of perturbation functions with respect to the SC case, as the size of the active space increases.

Table 4.3: Analysis of the CASSCF wavefunction composition. Only the configurations with weight greater than 5% are considered.

	CAS(4/4)		CAS(14/13)	
State	Config.	Weight (%)	Config.	Weight (%)
1^1B_{3u}	$5b_{1u} \rightarrow 4b_{2g}$	43	$5b_{1u} \rightarrow 4b_{2g}$	46
	$2a_u \rightarrow 4b_{3g}$	55	$2a_u \rightarrow 4b_{3g}$	42
2^1B_{3u}	$5b_{1u} \rightarrow 4b_{2g}$	52	$5b_{1u} \rightarrow 4b_{2g}$	25
	$2a_u \rightarrow 4b_{3g}$	39	$4b_{1u} \rightarrow 4b_{2g}$	22
			$2a_u \rightarrow 4b_{3g}$	35
3^1B_{3u}			$5b_{1u} \rightarrow 4b_{2g}$	37
			$4b_{1u} \rightarrow 4b_{2g}$	34
			$2a_u \rightarrow 4b_{3g}$	9
4^1B_{3u}			$3b_{1u} \rightarrow 4b_{2g}$	87
1^1B_{2u}	$5b_{1u} \rightarrow 4b_{3g}$	40	$5b_{1u} \rightarrow 4b_{3g}$	41
	$2a_u \rightarrow 4b_{2g}$	58	$2a_u \rightarrow 4b_{2g}$	51
2^1B_{2u}	$5b_{1u} \rightarrow 4b_{3g}$	55	$5b_{1u} \rightarrow 4b_{3g}$	43
	$2a_u \rightarrow 4b_{2g}$	36	$2a_u \rightarrow 4b_{2g}$	37
3^1B_{2u}			$4b_{1u} \rightarrow 4b_{3g}$	56
			$3b_{1u} \rightarrow 4b_{3g}$	20
4^1B_{2u}			$4b_{1u} \rightarrow 4b_{3g}$	66
			$5b_{1u} \rightarrow 4b_{3g}$	14

Actually, as is apparent, these deviations are more consistent for the higher excited states and the maximum value (0.43 eV) is obtained for the 4^1B_{3u} state. These

increasing discrepancies are a clear clue of the inadequacy of such an active space, including only 13 valence π orbitals (slightly more than half of the complete π valence space), to describe high–energy excited states. Then, it should be considered that the use of molecular orbitals not fully optimized, but obtained from state–averaged calculations, possibly contributes to the defective zero order description.

The most accurate NEVPT results predict the vertical transition to the 1^1B_{3u} and 1^1B_{2u} states at 2.05 and 2.56 eV (CAS(14/13) calculation), in remarkable accordance with the experimental values of 1.98-2.02 (Q_x) and 2.33-2.42 eV (Q_y). Also, we note that, for the Q band, the results obtained from the "four–orbital" based calculations (CAS(4/4) space) can be regarded as satisfactory. Moreover, the splitting between the 1^1B_{3u} and 1^1B_{2u} states, computed to be 0.47 eV, at the PC level, fully agrees with the observed value of 0.44 eV [148].

If on the one hand the Q band assignment is, altogether, well established, on the other hand the interpretation of the B band is still debated in the literature. In fact, according to Gouterman's model [149–151] two components, with perpendicular polarizations, should be distinguished: the B_x and B_y bands, arising from the 2^1B_{3u} and 2^1B_{2u} states respectively. The line splitting between the two components of the B band, measured at low temperature [146], amounts to 0.03 eV. This traditional interpretation, supported by some experimental evidence [147], as well as by the CASPT2 [139, 156], TD-DFT [144] and MRPT [140] calculations, was however questioned by Nakatsuji *et al.* [134] and Tokita *et al.* [135], who, on the basis of their SAC-CI calculations, assigned the 2^1B_{3u} state to the B band, but the 2^1B_{2u} state to the N band, appearing as a shoulder to the intense B band. Nevertheless, the SAC-CI oscillator strengths of the two transitions, not matching with the spectrum profile, seem to be a weak point of their conclusions (see Ref. [138]).

The PC-NEVPT2(4/4) results locate the 2^1B_{3u} state at 3.22 eV and the 2^1B_{2u} state at 3.30 eV, predicting a splitting of 0.08 eV, slightly greater then the experimental value of 0.03 eV. A small reduction of this splitting is observed in the CAS(14/13) calculations, where the two states are computed, at the PC level, at 3.30 and 3.35 eV respectively, in reasonable agreement with experiments (3.13-3.33 eV). While the description of the 2^1B_{2u} state provided by the CAS(4/4) calculations is comparable to that obtained using the larger active space, this is not the case for the 2^1B_{3u} state. Indeed, as shown in Tab. 4.3, while, with both active spaces, the reference wavefunction of the 2^1B_{2u} state is dominated by the $4b_{1u} \rightarrow 4b_{3g}$ and $2a_u \rightarrow 4b_{2g}$ configurations, in the larger calculation, the 2^1B_{3u} state is also described by the $4b_{1u} \rightarrow 4b_{3g}$ excitation (22%), not considered in Gouterman's four–orbital model.

The interpretation of the two higher–energy bands is certainly more complex and also the experimental evidence is less clear. Moreover, as shown by Gwaltney and Bartlett [138], in this region of the spectrum (4.5-5 eV) the Rydberg transitions are

expected to start. By now, the firmest assignment, suggested by Serrano-Andrès *et al.* [139], is that the N band has to be ascribed to the pair of states 3^1B_{3u}-3^1B_{2u} and, analogously, the so-called L band is assigned to the 4^1B_{3u}-4^1B_{2u} states. However, as apparent in Tab. 4.2, quite a conflicting picture emerges from the results of the various theoretical methods, with differences in the computed excitation energies greater than 1 eV. At the partially contracted level, the 3^1B_{3u}-3^1B_{2u} states are computed at 3.84-4.13 eV, whereas the other pair of states 4^1B_{3u}-4^1B_{2u} is located at 4.50-4.10 eV. Our results, overall, are consistent with the CASPT2 interpretation, since the largest deviation between the PC-NEVPT2 and CASPT2 amounts roughly to 0.7 eV (3^1B_{2u} state). Nevertheless, a too sizable splitting, with respect to that computed by Serrano-Andrés *et al.* [139], is found between the components of each pair of states. However, at the present stage of calculation, since the ground state geometry, basis set and, above all, the active space used for this study are not the same as in Ref. [139], and hence also the nature of the excited states computed is not exactly the same, the direct comparison with the CASPT2 results should be regarded with care.

Part II

Mixed–Valence systems

Chapter 5

Electron transfer in a model spiro system

5.1 Introduction

The present chapter addresses the problem of the description of the Electron Transfer (ET) processes in Mixed–Valence (MV) compounds in the framework of multireference perturbation theory. The investigation is carried out on the model MV spiro system reported in Fig. 5.1, (the 5,5′(4H,4H′)- spirobi[cyclopenta[c]pyrrole]2,2′,6,6′tetrahydro cation) [157], which, due to its relatively small size, allows the application of highly–correlated methodologies.

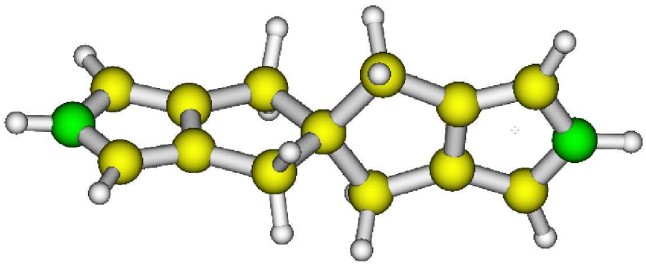

Figure 5.1: Molecular structure of the spiro molecule

The work presented here [42, 43] was thought as the extension of a previous CASSCF and MRCI study [158], which reports an extensive investigation by using different basis sets and computational approaches (canonical *vs.* localized orbitals).

After a short introduction to the ET processes in MV systems (section 5.2), the model spiro system, subject of the present investigation, is presented in section 5.3 and the computational approach is, instead, illustrated in section 5.4. Section 5.5 shows that MRPT treatments (such as, for instance, NEVPT2 and CASPT2 [17])

with a standard definition of the MO's and of their energies are inadequate for the MV systems, leading to an unphysical description of the electronic energy curve as a function of the reaction coordinate. In the same section, it is shown that the application of the perturbation approach to the third order in the energy is able to restore the correct shape of the energy profile. The origin of such a behaviour is illustrated in section 5.6, by resorting to a simple Marcus–like two–state model comprising only three electrons in four orbitals. By using this model, a strategy based on the use of the canonical orbitals of a state–averaged calculation and with state–averaged orbital energies is proposed with the aim to overcome the failure of the second order perturbation treatment based on state–specific canonical orbitals and energies. This strategy is adopted in actual calculations on spiro in section 5.7, confirming its validity.

5.2 Electron Transfer reactions and Mixed–Valency

The pivotal rôle played by the ET processes in a great deal of chemical–physical and biological phenomena, accounts for the extensive research efforts addressed to the understanding of its mechanisms. In the domain of the intramolecular ET, Mixed–Valence (MV) compounds play a relevant rôle as simple model systems suitable for understanding the adiabatic ET phenomena [159–164]. Furthermore, MV compounds are extensively investigated, both experimentally and theoretically, particularly in the field of the inorganic binuclear MV complexes [165], for their appealing optical and magnetic properties as well as for their possible application in molecular electronics and photonics [166]. Nevertheless, more recently, an increasing attention has been paid to the purely organic MV systems (see, for instance, the extensive work on the triarylamine–based MV systems by Lambert and Nöll [167]), since their Inter Valence Charge Transfer (IV-CT) band is, generally, not affected by the overlap with other low–lying transitions, contrary to what may occur for inorganic compounds due to appearance of the $d \rightarrow d$ metal to ligand (MLCT) or ligand to metal (LMCT) charge transfer excitations.

The simplest MV compound is composed of two moieties (hereafter indicated with A and B), linked either directly or via a bridge, where an inter–valence ET (IV-ET) occurs between the two redox sites being in different oxidation states. The electronic coupling between the two ideally non–interacting systems, where the electron (hole) is localized either on the left or on the right moiety, governs the communication between the two subunits, determining the general properties of the system. Such interaction is expressed by the Hamiltonian matrix element $\mathcal{H}_{ab} = \left\langle \Psi_a \left| \hat{\mathcal{H}} \right| \Psi_b \right\rangle$, where Ψ_a and Ψ_b are the diabatic states, one with the electron/hole localized on the

(left) subunit A and the other on the (right) subunit B.

According to the usual classification by Robin and Day [168], MV systems can be divided into three classes:

- class I: redox centers strongly localized (**complete valence trapping**);
- class II : partial delocalization arising from a weak electronic interaction (**valence trapping**);
- class III : strong electronic coupling which gives rise to a complete delocalized system with a single minimum for the ground state (**delocalized valency**).

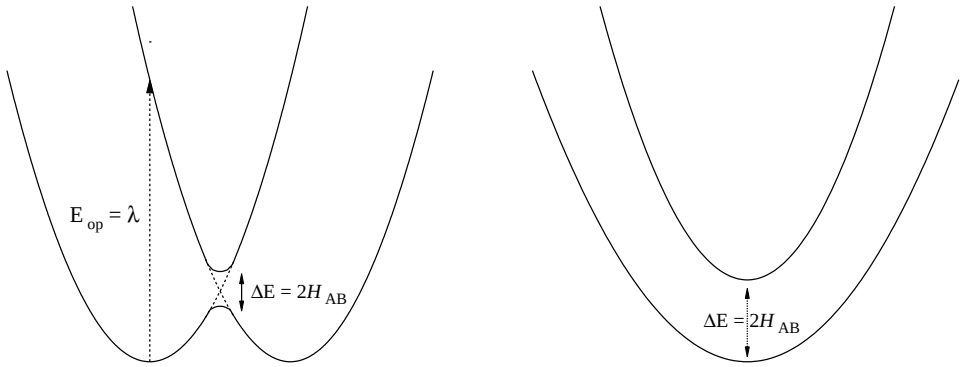

(a) class II (b) class III

Figure 5.2: Potential Energy Surfaces (PESs) of an ET reaction in a symmetric MV compound.

In the case of class II and class III compounds (Fig. 5.2), the analysis of the IV-CT band, either based on the semiclassical Hush theory [169,170] or on a more rigorous quantum mechanical approach [171], provides a direct way to estimate $\mathcal{H}_{ab}$, and the reorganization energy, λ. The extent of the electronic coupling can also be obtained experimentally by means of Electron Spin Resonance (ESR), Nuclear Magnetic Resonance (NMR) Spectroscopy as well as Photoelectron Spectroscopy measures (see Refs. [172,173] for a more detailed overview). Nevertheless, since the obtaining of a reliable experimental measure of $\mathcal{H}_{ab}$ is often not possible, particularly for strongly coupled systems, where the ET rates are much faster than the typical time scale of the above cited experimental techniques and, additionally, the significant vibronic coupling makes the Hush theory no longer applicable, the development of accurate and efficient computational strategies represents a crucial issue in the study of MV systems. Moreover, the accurate theoretical prediction of the electronic

coupling would represent a powerful tool for the design of new "spacers", allowing the specific modulation of the properties of the ET process (e.g. long or short distance ET). In the framework of the widely used two–state one–mode model and in the simple case of symmetry–equivalent donor and acceptor groups, the electronic coupling $\mathcal{H}_{ab}$ is defined as half the energy splitting (ΔE) between the two adiabatic potential surfaces at the crossing seam, and it can be computed using different methodologies and approaches [157, 158, 167, 174–186].

Nevertheless, the theoretical study of thise kind of systems presents difficulties: the effect of the dynamical correlation has to be evaluated, improving the qualitative minimal description given by the simple mixing of the quasi degenerate determinants accounting for the two charge distributions. These difficulties are related to the intrinsic multireference (MR) nature of the ground and the first excited state wavefunctions of these systems and to their dimension, which makes impractical the use of too expensive computational approaches. MR perturbation theory (MRPT), among the other MR methods, is a good candidate due to the reliability shown in many MR applications and due to the scaling properties of the computational cost with respect to the dimensions of the system. With the exception of some recent semiempirical Austin Model 1 (AM1) computations [167, 183], the most frequently applied methods, to study the ET process, are based on Density Functional [176] and Time–Dependent Density Functional Theories (TD-DFT) [180, 181]. However, as shown in different applications [181,187], some doubts have been raised concerning the applicability of the DFT approach to the study of the electron transfer in MV compounds, since the computed electronic coupling has been shown to be systematically underestimated by 20-30% in comparison to the results of more refined *ab initio* calculations.

5.3 The model Spiro system

The π-σ-π spiro molecule (reported in Fig. 5.3) consists of two pyrrolic units (π systems), lying on two perpendicular planes, connected by a spirocycloalkane rigid σ bridge. The symmetry of the neutral molecule is D_{2d}, with the C_2 axis (the z axis) passing through the two N atoms; if an electron is removed from the system, the positive charge tends to localize on the left or on the right pyrrolic unit, distorting the symmetry and giving rise to two equivalent C_{2v} minima. These are separated by a symmetrical D_{2d} saddle point at the crossing seam, corresponding to the situation of a complete delocalization of the positive charge over the whole molecule.

Although some arguments about the equilibrium geometry of the spiro cation in either its left/right–localized or delocalized structures have been provided and C_1

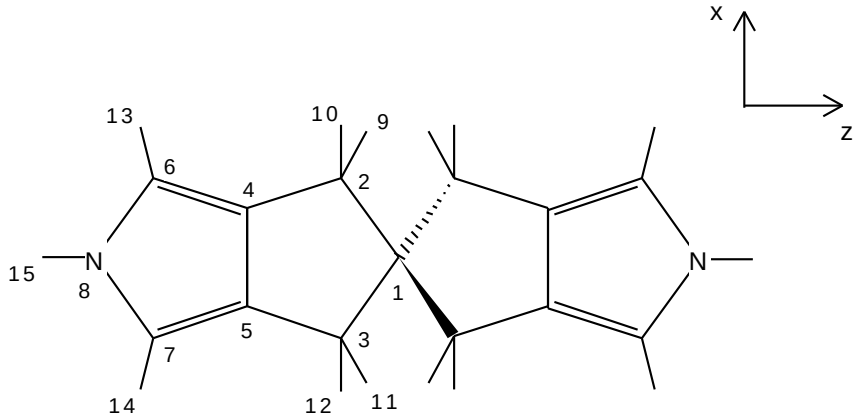

Figure 5.3: Structure of the spiro molecule

and C_2 symmetries have been respectively suggested [177], here, as in Refs. [158,186], we adopt the C_{2v} point group for the two minima with the localized charge and the D_{2d} symmetry for the structure at the saddle point.

The "π system" of the spiro cation, composed of the π systems localized on the two pyrrolic rings, comprises 11 π electrons and 10 π orbitals and, at the single determinant level and in the C_{2v} point group, the electronic configuration is given by $(\sigma\text{–core})(1b_1)^2(2b_1)^2(1b_2)^2(2b_2)^2(1a_2)^2(2a_2)^1$. Therefore, the ground and the first excited states, involved in the ET process, are two states of A_2 symmetry, denoted as $^2A_2(1)$ and $^2A_2(2)$ in the following.

The ET process was studied along an *ad hoc* approximate reaction path, defined by the linear mixing of the cartesian coordinates of the two optimized C_{2v} geometries [158]:

$$\mathbf{Q}(\xi) = \left(\frac{1}{2} - \xi\right)\mathbf{Q}_A + \left(\frac{1}{2} + \xi\right)\mathbf{Q}_B \tag{5.1}$$

where the mixing parameter ξ was varied, in steps of 0.05, from -1.50 to +1.50 and $\mathbf{Q}_A$ and $\mathbf{Q}_B$ are vectors collecting the coordinates of the two optimized C_{2v} geometries. Therefore, the two equivalent minima are in $\xi = -0.50$ ($\mathbf{Q}_A$, charge on the left A moiety) and $\xi = +0.50$ ($\mathbf{Q}_B$, charge on the right B moiety). An "averaged" D_{2d} geometry, which was however found to be very close to the optimized one (see Ref. [158]), is obtained at the crossing seam point (ξ=0.0). Nevertheless, since the MOLCAS package [76], used to obtain the CASSCF wavefunctions, can only deal with Abelian point groups, the calculations for the non–Abelian D_{2d} group were performed using the reduced C_{2v} symmetry.

5.4 Computational details

Following the previous works, the calculations were carried out with basis sets of Atomic Natural Orbitals (ANO-L) [72] type. Different contractions levels were adopted: C,N[2s1p] and H[1s] (SZ); C,N[3s2p] and H[2s] (DZ); C,N[3s2p1d] and H[2s1p] (DZP) and, finally, C,N[4s3p1d] and H[3s1p] (TZP).

For the calculation of the reaction coordinate (see section 5.3), use has been made of the geometries optimized in Ref. [158] at the Restricted Open Shell Hartree–Fock (ROHF) level with a triple zeta plus Polarization (TZP) ANO basis set [72].

State–averaged CASSCF calculations were performed for the two $^2A_2$ states using different active spaces: CAS(3/2), just composed of the three electrons and the two a_2 (HOMO and HOMO-1) orbitals; CAS(11/10), comprising the whole π system of the molecule, obtained distributing eleven active electrons into ten active orbitals and an intermediate space, composed of seven electrons and four orbitals, CAS(7/4). The explicit composition, in the C_{2v} point group, of the active spaces used, is reported in Tab. 5.1.

Table 5.1: Active space composition and nomenclature.

Active Space	Composition[a]
CAS(3/2)	3-4a_2
CAS(7/4)	12b_1, 12b_2,3-4a_2
CAS(11/10)	11-13b_1, 11-13b_2, 3-6a_2

[a] At the SCF level, in the C_{2v} point group, the ground state electronic configuration of the neutral system is $(25a_1)^2(12b_1)^2(12b_2)^2(4a_2)^2$.

In all the perturbative calculations, the 1s orbitals of N and C were kept uncorrelated.

Finally, all the energy differences, reported in the next sections, were computed with respect to the energy of the ground state of the cation at the C_{2v} geometry with $\xi = +0.5$ ($\xi = -0.5$), corresponding to that of the optimized geometry $\mathbf{Q}_A$ ($\mathbf{Q}_B$), although it might not be the actual minimum of the curve.

5.5 Second and third order standard MRPT

This section is devoted to the discussion of the results provided by a standard perturbation approach (hereafter indicated as NEVPT(can) and CASPT2(can)), which is based on the use of state–specific canonical molecular orbitals and orbital energies. Therefore, the zero order wavefunctions were defined performing a state–averaged

CASSCF calculation on the two $^2A_2$ states, followed by two distinct single–root CASCI calculations, in order to build the canonical orbitals and to compute the orbital energies for each state. Here, we shall just report the results computed with the minimal basis set (SZ) and active space, CAS(3/2).

The computed CASSCF, NEVPT2(can), CASPT2(can) and NEVPT3(can) energy differences are collected in Tab. 5.2. As is apparent from the energy profiles reported in Fig. 5.5, and from the computed values of the energy barriers in Tab. 5.2, a non–physical description of the two adiabatic PES, in proximity of the symmetrical saddle point is attained with both the NEVPT2 and CASPT2 approaches.

Table 5.2: Spiro cation: NEVPT2(can), NEVPT3(can) and CASPT2(can) energies (kJ/mol) of the ground state, $^2A_2(1)$, at $\xi = 0.0$ and of the first excited state, $^2A_2(2)$, at $\xi = 0.0$ and $\xi = -0.5$. All the energies are computed with respect to the energy of the ground state at $\xi = -0.5$. For the sake of clarity the energy splitting (ΔE kJ/mol) between the two states at $\xi = 0.0$ is also reported. For the CASPT2 results the level shift was varied from 0.0 to 0.2 hartree.

States	CAS	NEVPT(can)			CASPT2(can)		
		SC-PT2	PC-PT2	SC-PT3	L.S. 0.0	L.S. 0.1	L.S. 0.2
$\xi = -0.5$							
$^2A_2(2)$	56.690	51.442	51.441	51.539	50.001	50.043	50.151
$\xi = 0.0$							
$^2A_2(1)$	8.328	-5.117	-5.330	3.765	-5.790	-5.724	-5.503
$^2A_2(1)$	17.371	4.726	4.505	12.983	4.017	4.087	4.314
ΔE ($\xi = 0.0$)							
$^2A_2(2)$	9.043	9.843	9.835	9.218	9.807	9.811	9.817

In particular, an increasing overestimation of the correlation energy, starting at $\xi = -0.15$ and culminating at $\xi = 0$, is observed, with the consequent loss of the barrier and the appearance of a "well" in the avoided–crossing region. Indeed, both NEVPT2(can) and CASPT2(can) calculations, irrespective of whether a level shift is used or not in the latter case (thereby excluding an intruder state problem), yield for the $^2A_2(1)$ state the D_{2d} nuclear configuration $\simeq$5 kJ/mol below the C_{2v} minimum. As shown in Fig. 5.5, the SC–NEVPT2(can) and the CASPT2(can) curves are almost parallel along the reaction coordinate and the computed energy differences collected in Tab. 5.2 are in very good accordance. The energy splitting at the D_{2d} geometry amounts roughly to 9.8 kJ/mol, very close to that computed at CASSCF level ($\simeq$9 kJ/mol). As is apparent, proceeding up to the third order is essential to restore the correct behavior of the two PES, with the expected double–well profile for the ground state and with the smooth parabolic curve for the first excited state.

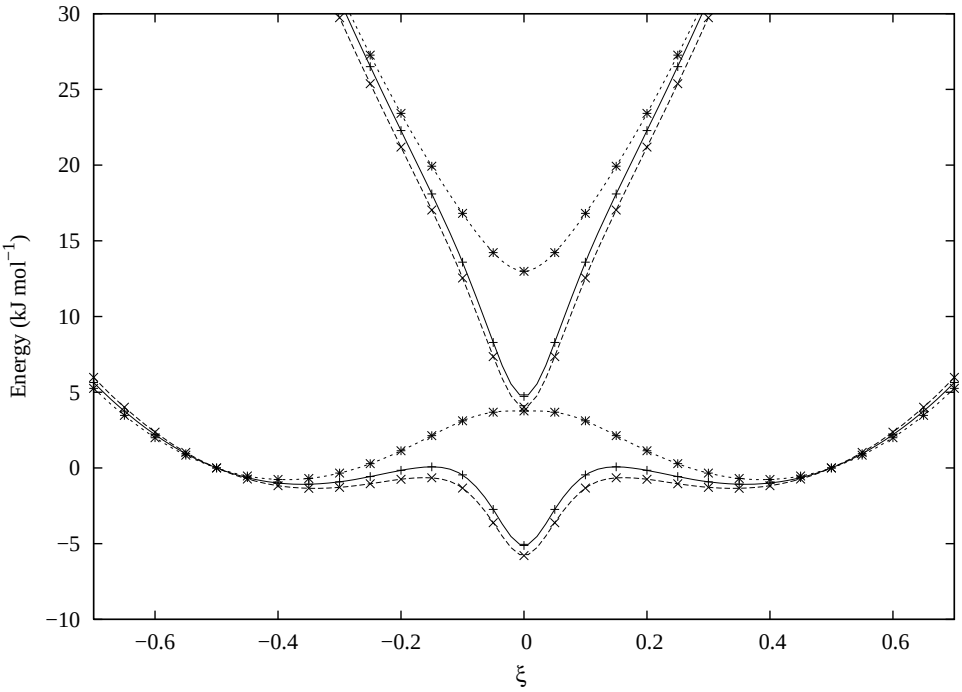

Figure 5.5: SC-NEVPT2(can), SC-NEVPT3(can) and CASPT2(can) (no level shift) PES of the $^2A_2(1)$ and $^2A_2(2)$ states of the spiro cation. All the curves are shifted in order to have the two C_{2v} minima at zero energy. Full lines and "+" points, NEVPT2(can) energies; dashed lines and "×" points, CASPT2(can) energies; dotted lines and "∗" points, NEVPT3(can) energies.

The SC-NEVPT3 [24] calculation is rather expensive on this system and one can reasonably expect the PC-NEVPT3 and CASPT3 results to agree with the SC-NEVPT3. The energy barrier computed at SC-NEVPT3(can) level is 3.765 kJ/mol, whereas a value of 8.328 kJ/mol is obtained from the CASSCF calculation. Finally, it is interesting to notice that the splitting of the two states seems to be unaffected by the wrong second order description, being essentially the same at the CASSCF, second and third order PT levels. In the following section, this general failure of the MRPT2 treatment making use of a partially monoelectronic zero order Hamiltonian and of state–specific canonical orbitals and orbital energies, together with the benefit brought by the third order correction, will be demonstrated and discussed, for a simple Marcus–like two–state model.

5.6 Failure of a standard MRPT approach

5.6.1 A simple two-state model

Let us consider a model system A, with two electrons and two orbitals, a and a^* (a lower in energy than a^*). In a perturbation scheme, using the Møller-Plesset [26] partition of the Hamiltonian, the zero–order wavefunction is the determinant $\|a\bar{a}\|$ and only one perturber ($\|a^*\bar{a}^*\|$) must be considered (if the orbitals are supposed to be optimized, the single excitations are excluded due to Brillouin's theorem [7]). The first order correction to the wavefunction is

$$\Psi^{(1)} = -\frac{\langle aa|a^*a^*\rangle}{2(\varepsilon^{\mathrm{A}}_{a^*} - \varepsilon^{\mathrm{A}}_{a})}\|a^*\bar{a}^*\| \tag{5.2}$$

and the second and third order corrections to the energy are:

$$E^{(2)}_{\mathrm{A}} = -\frac{|\langle aa|a^*a^*\rangle|^2}{2(\varepsilon^{\mathrm{A}}_{a^*} - \varepsilon^{\mathrm{A}}_{a})} \tag{5.3}$$

$$\begin{aligned} E^{(3)}_{\mathrm{A}} &= \left\langle \Psi^{(1)} \left| \mathcal{V} \right| \Psi^{(1)} \right\rangle - E^{(1)} \langle \Psi^{(1)} | \Psi^{(1)} \rangle \\ &= \frac{|\langle aa|a^*a^*\rangle|^2}{4(\varepsilon^{\mathrm{A}}_{a^*} - \varepsilon^{\mathrm{A}}_{a})^2} \left[E\left(\|a^*\bar{a}^*\|\right) - E\left(\|a\bar{a}\|\right) \right] + E^{(2)}_{\mathrm{A}} \end{aligned} \tag{5.4}$$

where $\mathcal{V}$ is the perturbation operator ($\hat{\mathcal{H}} = \hat{\mathcal{H}}_0 + \mathcal{V}$),

$$\varepsilon^{\mathrm{A}}_{a} = \langle a \left| h \right| a \rangle + \langle aa|aa\rangle \tag{5.5}$$

$$\varepsilon^{\mathrm{A}}_{a^*} = \langle a^* \left| h \right| a^* \rangle + 2\langle a^*a|a^*a\rangle - \langle a^*a|aa^*\rangle \tag{5.6}$$

are the orbital energies of the a and a^* orbitals (the superscript A has been added to stress that the orbital energies refer to the A system treated alone) and

$$E\left(K\right) = \left\langle K \left| \hat{\mathcal{H}} \right| K \right\rangle \tag{5.7}$$

is the energy of determinant K.

Consider now a second system B, equal to A, and the supersystem $(\mathrm{A}\cdots\mathrm{B})^+$ where A and B are weakly interacting (Fig. 5.6.1). The molecular orbitals of the AB system can be regarded as localized and they are very close to the orbitals of A and B: they are therefore indicated in the following with a, a^*, b and b^*.

The ground state zero order wavefunction for the supersystem is described by the linear combination of the two quasi–degenerate determinants $\|ab\bar{b}\|$ and $\|a\bar{a}b\|$ (corresponding to the $\mathrm{A}^+\cdots\mathrm{B}$ and $\mathrm{A}\cdots\mathrm{B}^+$ charge distributions, respectively):

$$\Psi^{(0)} = c_1\|ab\bar{b}\| + c_2\|a\bar{a}b\| \ . \tag{5.8}$$

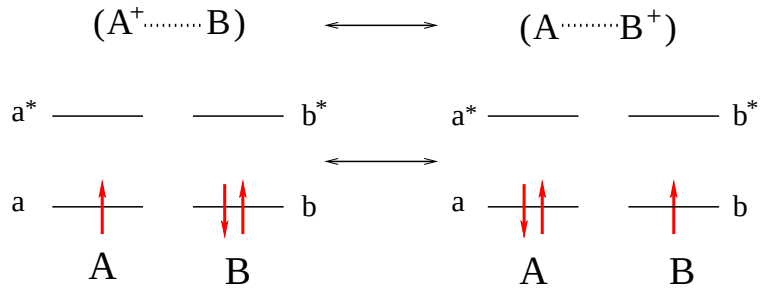

Figure 5.6: Schematic representation of the $A^+\cdots B$ and $A\cdots B^+$ systems

We suppose a small relaxation of the geometry going from A (B) to A^+ (B^+). The weak coupling between the two systems A and B is given by an effective Hamiltonian of the form:

$$\mathbf{H} = \begin{vmatrix} k_1(\frac{1}{2}-\xi)^2 & k_2 \\ k_2 & k_1(\frac{1}{2}+\xi)^2 \end{vmatrix} \tag{5.9}$$

where ξ is a "reaction coordinate": with $\xi = -0.5$ the system is described by $A^+\cdots B$ while with $\xi = 0.5$ the system is $A\cdots B^+$. The values of k_1 and k_2 are such that c_1 remains close to 1 for $\xi < -\delta$ and is close to 0 for $\delta < \xi$, with $0 < \delta \ll 1$.

5.6.2 Second order correction

To compute the second order correction to the energy one has to use in this case a MRPT scheme, and in order to keep the approach as simple as possible, the Møller–Plesset barycentric [188] (MPB) partition of the Hamiltonian is adopted. The orbital energies of the $(A\cdots B)^+$ system are computed using the formula [189]:

$$\varepsilon_i = \langle i\,|h|\,i\rangle + \sum_k n_k \left[\langle ik|ik\rangle - \frac{1}{2}\langle ik|ki\rangle\right] \tag{5.10}$$

where n_k is the natural occupation of orbital k ($n_a = 1 + |c_2|^2$, $n_b = 1 + |c_1|^2$, and $n_{a^*} = n_{b^*} = 0$). In the MPB partition, the zero order energy of the ground state is:

$$E^{(0)} = (1 + |c_2|^2)\varepsilon_a + (1 + |c_1|^2)\varepsilon_b \tag{5.11}$$

In order to simplify the derivation, we use the approximation to neglect the bielectronic integrals in which one electronic distribution (of electron 1 or 2) is the product of orbitals one on A and the other on B. With this approximations, the

orbital energies are:

$$\varepsilon_a = \langle a\,|h|\,a\rangle + \frac{1+|c_2|^2}{2}\langle aa|aa\rangle + \left(1+|c_1|^2\right)\langle ab|ab\rangle \tag{5.12}$$

$$\varepsilon_b = \langle b\,|h|\,b\rangle + \frac{1+|c_1|^2}{2}\langle bb|bb\rangle + \left(1+|c_2|^2\right)\langle ab|ab\rangle \tag{5.13}$$

$$\begin{aligned}\varepsilon_{a^*} = {} & \langle a^*\,|h|\,a^*\rangle + \left(1+|c_2|^2\right)\langle aa^*|aa^*\rangle - \frac{1+|c_2|^2}{2}\langle aa^*|a^*a\rangle + \\ & + \left(1+|c_1|^2\right)\langle a^*b|a^*b\rangle\end{aligned} \tag{5.14}$$

$$\begin{aligned}\varepsilon_{b^*} = {} & \langle b^*\,|h|\,b^*\rangle + \left(1+|c_1|^2\right)\langle bb^*|bb^*\rangle - \frac{1+|c_1|^2}{2}\langle bb^*|b^*b\rangle + \\ & + \left(1+|c_2|^2\right)\langle b^*a|b^*a\rangle\end{aligned} \tag{5.15}$$

We note that the dependence of these orbital energies on ξ (through the dependence of c_1 and c_2 on ξ) agrees with the one found in the NEVPT calculations reported in the previous section, as is apparent from Fig. 5.7 where the orbital energies used in the NEVPT2 calculation for four representative inactive orbitals are reported as a function of ξ. The dependence of the charge of the B moiety (equivalent to $|c_2|^2$ in the model) as a function of ξ is also reported for the sake of clarity.

Let us turn to the calculation of the second order perturbation correction to the energy: the single excitations are considered to give negligible contributions, since local single excitations on the two systems can be disposed of if the orbitals are supposed to be optimized (contracted singles would yield strictly zero according to the Generalized Brillouin theorem [14]) and, moreover, intersystem excitations are thought to have a small contribution due to the weak interaction between the two systems. Therefore only the two doubly excited perturbers, $\|ab^*\bar{b}^*\|$ and $\|a^*\bar{a}^*b\|$ (with zero order energy $\varepsilon_a + 2\varepsilon_{b^*}$ and $\varepsilon_b + 2\varepsilon_{a^*}$, respectively) must be considered, obtaining for the second order correction to the energy:

$$\begin{aligned}E^{(2)} = {} & -|c_1|^2\frac{|\langle bb|b^*b^*\rangle|^2}{2\varepsilon_{b^*} - \left(1+|c_1|^2\right)\varepsilon_b - |c_2|^2\,\varepsilon_a} \\ & -|c_2|^2\frac{|\langle aa|a^*a^*\rangle|^2}{2\varepsilon_{a^*} - \left(1+|c_2|^2\right)\varepsilon_a - |c_1|^2\,\varepsilon_b}\end{aligned} \tag{5.16}$$

and for the first order correction to the wavefunction

$$\Psi^{(1)} = -c_1\frac{\langle bb|b^*b^*\rangle}{2(\varepsilon_{b^*}-\varepsilon_b)}\|ab^*\bar{b}^*\| - c_2\frac{\langle aa|a^*a^*\rangle}{2(\varepsilon_{a^*}-\varepsilon_a)}\|a^*\bar{a}^*b\|\ . \tag{5.17}$$

Since the two subsystems A^+ and B (or A and B^+) are supposed to be weakly interacting and given that the ionized system need not be correlated, the second

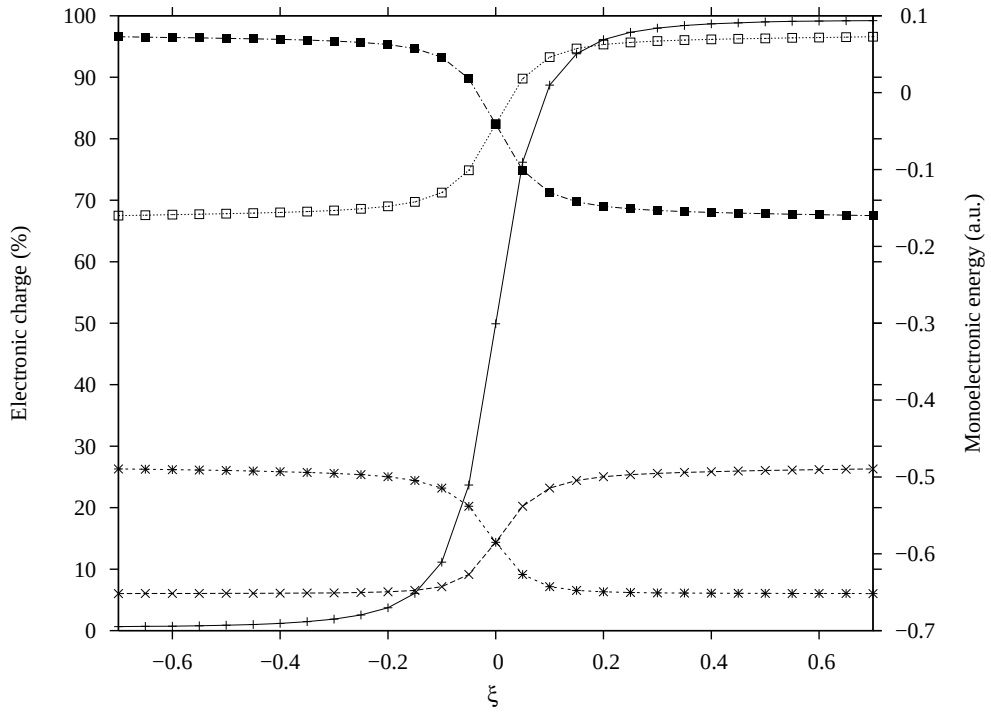

Figure 5.7: Spiro cation: variation of the charge of the B moiety (in %) and of the orbital energies (in hartree) of two core and two virtual representative orbitals along the reaction coordinate ξ. Charge of the B moiety, full line and "+" symbols; energy of a core and a virtual π orbital localized on A, "$\times$" and open square symbols, respectively; energy of a core and a virtual π orbital localized on B, "$*$" and black square symbols, respectively.

order approximation to the energy, $E^{(2)}$, is expected to be very close (equal at the non–interaction limit) to that of the isolated system A (or B), computed in equation (5.3) for all $-0.5 \leq \xi \leq 0.5$.

Note that for $\xi = -0.5$ and $\xi = 0.5$ ($c_1 \simeq 1$, $c_2 \simeq 0$ and $c_1 \simeq 0$, $c_2 \simeq 1$, respectively), equation (5.16) correctly reduces to equation (5.3), apart from the small integrals $\langle ab|ab\rangle$ and $\langle a^*b|a^*b\rangle$.

Let us consider the case $\xi = 0$: making use of the equalities $|c_1|^2 = |c_2|^2$, $\varepsilon_{a^*} = \varepsilon_{b^*}$ and $\varepsilon_a = \varepsilon_b$ and noting that $\langle aa|a^*a^*\rangle = \langle bb|b^*b^*\rangle$, one has

$$E^{(2)} = -\frac{|\langle aa|a^*a^*\rangle|^2}{2(\varepsilon_{a^*} - \varepsilon_a)} \tag{5.18}$$

and

$$\Psi^{(1)} = -\frac{\langle aa|a^*a^*\rangle}{2(\varepsilon_{a^*} - \varepsilon_a)} \left[c_1 \|ab^*\bar{b}^*\| + c_2 \|a^*\bar{a}^*b\|\right] \tag{5.19}$$

where

$$\varepsilon_a = \langle a\,|h|\,a\rangle + 0.75\langle aa|aa\rangle + 1.5\langle ab|ab\rangle \tag{5.20}$$

$$\varepsilon_{a^*} = \langle a^*\,|h|\,a^*\rangle + 1.5\langle a^*a|a^*a\rangle - 0.75\langle a^*a|aa^*\rangle + 1.5\langle a^*b|a^*b\rangle \tag{5.21}$$

Expressions (5.20) and (5.21) for the orbital energies are different from those reported in eqs. (5.5) and (5.6), even disregarding the small integrals $\langle ab|ab\rangle$ and $\langle a^*b|a^*b\rangle$. The denominator in (5.18) is smaller than the one in (5.3) (the onsite repulsion integrals $\langle aa|aa\rangle$ and $\langle a^*a|a^*a\rangle$ being large and positive) and the correlation energy is therefore larger in module.

It is worthwhile to point out that the model here discussed involves only active and virtual orbitals. The inclusion of core orbitals complicates the derivation. However, one can show that for $\xi = 0$ the perturbers obtained by a promotion of two core electrons into the active space ($V(+2)$ or $2h$ class) are associated with a denominator larger than the correct one and therefore their contribution to the correlation energy is too small. The same happens for the promotion of one core electron into the active space accompanied by an excitation inside the active space ($V(+1)'$ or $1h$ class). In the cases where both the core and the virtual orbitals are involved in the excitation process ($V(0)$ or $2h-2p$, $V(+1)$ or $1h-2p$, $V(-1)$ or $2h-1p$, and $V(0)'$ or $1h-1p$ classes) the analysis is more complex and there is a competition between the effect of the virtual orbital energies (which tend to give too small denominators) and the one of the core orbital energies (which, on the contrary, tend to give too large denominators).

The analogy between the model system and the NEVPT2 description of the spiro molecule is confirmed by the curves shown in Fig. 5.8 where the NEVPT2 correlation energy for each excitation class is plotted as a function of ξ. In order to have a prompt comparison of the behavior of the different NEVPT2 classes, the origin of the energy scale is different for each class and all plots have the same energy range (for more details, see caption of Fig. 5.8). As expected the $V(-2)$ class (two active electrons promoted to the virtual space) shows a sharp profile with too large a correlation energy close to $\xi = 0$. All the other classes, apart from the $V(-1)'$ class, involve both core and virtual orbitals and the effect of the virtual orbital energies is dominant for the $V(1)$ and $V(-1)$ classes, while for the $V(0)'$ the effect of the core orbital energies slightly prevails. The two effects almost compensate each other in the case of the $V(0)$ class. The behavior of the $V(-1)'$ class is peculiar: given that in this case only virtual inactive orbitals are involved in the excitation process, from the model system one can expect for this class a behavior similar to the one observed for the $V(-2)$ class, while the NEVPT2 curve shows an opposite shape. One must however note that, in the same energy scale of the other classes, the contribution of this class is almost constant and that the deviation from the correct behavior is negligible. However, the curve of the total CASSCF+NEVPT2 energy, reported in Figure 5.5, indicates that the effect of the virtual orbital energies (too large a correlation energy for $\xi = 0$) is dominant.

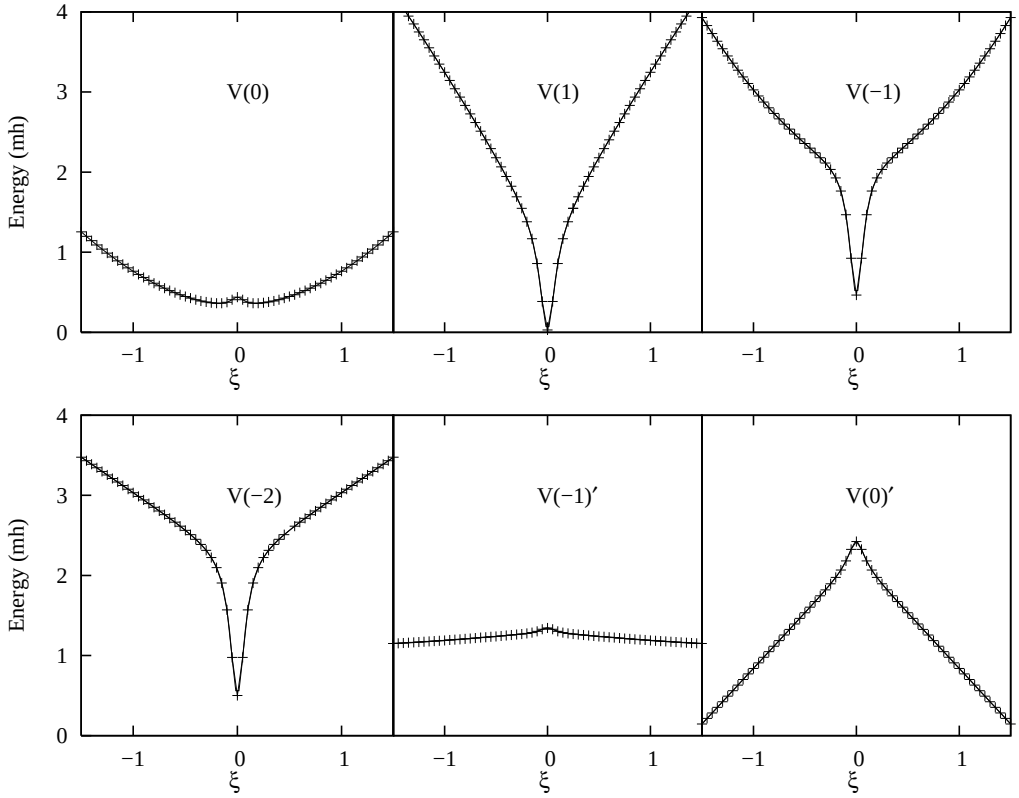

Figure 5.8: Spiro cation: contribution of the different classes to the NEVPT second order correction to the energy (in millihartree, mh) as a function of the reaction coordinate ξ. The $V(2)$ and $V(+1)'$ classes give vanishing contribution. In order to make the comparison between the different classes easier, the energy reported in figure is $E^{(2)}+E_{\text{shift}}$, where E_{shift} (in hartree, h) is different for each class: $V(0) \rightarrow E_{\text{shift}} = 0.6480$ h, $V(1) \rightarrow E_{\text{shift}} = 0.0185$ h, $V(-1) \rightarrow E_{\text{shift}} = 0.0730$ h, $V(-2) \rightarrow E_{\text{shift}} = 0.0115$ h, $V(-1)' \rightarrow E_{\text{shift}} = 0.0030$ h, and $V(0)' \rightarrow E_{\text{shift}} = 0.3000$ h. Moreover the same energy scale is adopted for all plots.

5.6.3 Third order correction

For the third order correction to the energy, the full derivation is rather irksome, even considering only active and virtual orbitals. In this case, one can, however, easily prove that for $\xi = -0.5$ and $\xi = 0.5$ the correct behavior is obtained.

For $\xi = 0$ one has

$$E^{(3)} = \frac{|\langle aa|a^*a^*\rangle|^2}{4(\varepsilon_{a^*} - \varepsilon_a)^2}\left[E\left(\|a^*\bar{a}^*b\|\right) - E\left(\Psi^{(0)}\right)\right] + E^{(2)} \tag{5.22}$$

where use has been made of the relations $E\left(\|a^*\bar{a}^*b\|\right) = E\left(\|ab^*\bar{b}^*\|\right)$ and $\left\langle \|a^*\bar{a}^*b\| \, |\mathcal{V}| \, \|ab^*\bar{b}^*\| \right\rangle = 0$. Introducing the new quantities

$$\Delta\varepsilon = 2\left(\varepsilon^{\text{A}}_{a^*} - \varepsilon^{\text{A}}_{a}\right) \tag{5.23}$$

and

$$\Delta = \Delta\varepsilon - 2\left(\varepsilon_{a^*} - \varepsilon_a\right) \tag{5.24}$$

one can expand $E^{(2)}$ and $E^{(3)}$ in McLaurin series with respect to $\Delta/\Delta\varepsilon$ (which is expected to be $\ll 1$) obtaining to the first order:

$$E^{(2)} \simeq E_{\mathrm{A}}^{(2)}\left(1 + \frac{\Delta}{\Delta\varepsilon}\right) \tag{5.25}$$

$$\begin{aligned} E^{(3)} &\simeq \frac{|\langle aa|a^*a^*\rangle|^2}{(\Delta\varepsilon)^2}\left[E\left(\|a^*\bar{a}^*b\|\right) - E\left(\Psi^{(0)}\right)\right]\left(1 + 2\frac{\Delta}{\Delta\varepsilon}\right) + E_{\mathrm{A}}^{(2)}\left(1 + \frac{\Delta}{\Delta\varepsilon}\right) \\ &\simeq E_{\mathrm{A}}^{(3)} + E_{\mathrm{A}}^{(2)}\left(1 - 2\frac{\left[E\left(\|a^*\bar{a}^*b\|\right) - E\left(\Psi^{(0)}\right)\right]}{\Delta\varepsilon}\right)\frac{\Delta}{\Delta\varepsilon} \end{aligned} \tag{5.26}$$

where the relation $E\left(\|a^*\bar{a}^*b\|\right) - E\left(\Psi^{(0)}\right) \simeq E\left(\|a^*\bar{a}\|\right) - E\left(\|a\bar{a}\|\right)$ has been used (the equality holds if A and B are non interacting). Therefore, neither $E^{(2)}$ nor $E^{(3)}$ show the correct behavior (which is $E_{\mathrm{A}}^{(2)}$ and $E_{\mathrm{A}}^{(3)}$, respectively) at the first order in $\Delta/\Delta\varepsilon$, but the sum of the two corrections

$$E^{(2)} + E^{(3)} \simeq E_{\mathrm{A}}^{(2)} + E_{\mathrm{A}}^{(3)} + 2E_{\mathrm{A}}^{(2)}\left(1 - \frac{\left[E\left(\|a^*\bar{a}^*b\|\right) - E\left(\Psi^{(0)}\right)\right]}{\Delta\varepsilon}\right)\frac{\Delta}{\Delta\varepsilon} \tag{5.27}$$

has the correct expression if $E\left(\|a^*\bar{a}^*b\|\right) - E\left(\Psi^{(0)}\right) = \Delta\varepsilon$. Even though such equality does not hold rigorously, the two terms can be supposed to be close, the first representing the energy difference between $\|a^*\bar{a}^*b\|$ and $\Psi^{(0)}$ computed with the full Hamiltonian, the second the same energy difference, but using the zero order Hamiltonian.

5.6.4 Conclusive remarks

This simple model allows the full rationalization of the results reported in section 5.5: the energy curve corrected to the second order using MRPTs in which the zero order Hamiltonian depends (at least partially) upon the orbital energies, shows an unphysical behavior with a "well" around the symmetric situation $\xi = 0$. Both NEVPT2 and CASPT2 are affected by this error but such behavior is expected to be common to practically all MRPTs (with a possible exception of the ones based on Epstein–Nesbet partition of the Hamiltonian [188]). However, while for NEVPT2, in which $\hat{\mathcal{H}}_0$ contains the orbital energies only for the inactive (core and virtual) orbitals the problem can be, in principle, alleviated by enlarging the active space, for CASPT2 this strategy is destined to fail, because of the monoelectronic nature of $\hat{\mathcal{H}}_0$ in all orbital spaces.

The irregularity is almost completely removed if the perturbation approach is applied up to the third order, thus restoring a regular curve. But, in the perspective of applying MRPT methods to real MV systems with a good quality basis set and reasonably large active spaces, the strategy to perform a third order calculation appears as too expensive a solution.

To this aim, this model suggests a practical strategy for limiting the calculation to the second order: indeed, if equations 5.12-5.15 are made independent of c_1 and c_2, the second order energy remains constant for all ξ and the unphysical "well" is removed. This can be obtained, for instance, by using $|c_1|^2 = |c_2|^2 = 0.5$, or equivalently by taking, for each orbital energy, the average of the two values computed at ξ and $-\xi$. In the actual calculations this results can be obtained computing, for each nuclear geometry, the orbital energies as the average between those pertaining to the ground state (GS) and to the first excited state of the same symmetry; in other terms, this "charge–averaged" MRPT2 strategy (hereafter referred to as "NEVPT2(av)"), relies on the use of state–averaged canonical molecular orbitals, obtained by diagonalization of the state–averaged Fock operator.

Finally, we note that in the NEVPT2(av) strategy, one has to give up the correct absolute value of the second order energy (notice that in this approach for $\xi = -0.5$ and $\xi = +0.5$ $E^{(2)} \neq E_{\mathrm{A}}^{(2)}$), the trade–off being a coherent evaluation of the energy along the "reaction path". This allows to get an accurate estimate of all those energy differences, such as the extent of the barrier, the energy splitting at the crossing seam as well as the excitation energy for the optically–activated ET, which are the key parameters in the study of the ET processes. Some further remarks may be addressed to the question of how general such "charge–averaged" MRPT2 approach can be. Actually, the strategy of using a zero order wavefunction as the result of an average procedure along the whole reaction path between the two charge distributions can be, in principle, extended to non–symmetrical MV systems, to MV compounds containing transition metals and also to strongly coupled systems. About the last point, it should be noted that the incorrect description of the region around the saddle point is basically related to the weak coupling between the two subunits, that brings about a sudden change in the monoelectronic energy differences as the nuclear configuration approaches the symmetrical delocalized conformation. Thus, even though the NEVPT2(av) method is well applicable to more strongly coupled compounds, in these kinds of systems the application of a standard MRPT2 approach is expected to be less problematic due to the more gradual change of the nature of the wavefunction when passing from one charge distribution to the other.

5.7 The use of state–averaged orbitals

Tabs. 5.3 and 5.4 display the CASSCF and NEVPT excitation energies obtained with the four basis sets and the two largest active spaces, CAS(7/4) and CAS(11/10) respectively. Tab. 5.5 collects the MRCI results published in Ref. [158] and here used as benchmark values to judge on the quality of those obtained at NEVPT2(av) and NEVPT3(can) levels; the comparison is made more meaningful by the use of the same basis sets (ANO-L [72] with SZ and DZ contractions) and of the same active space, CAS(7/4). The MRCI results reported here have been obtained at CAS+SD level using both an internally–contracted [48] (C-CAS+SD) and an uncontracted (CAS+SD) approach; finally, the subscript "can" indicates that canonical molecular orbitals were used. We have reported the excitation energies (kJ/mol) from the ground state, $^2A_2(1)$, at its energy minimum, taken as the value at $\xi = -0.5$, to the first excited state, $^2A_2(2)$, both at the C_{2v} ($\xi = -0.5$) and D_{2d} ($\xi = 0.0$) points; the height of the barrier for the thermal ET and the energy splitting ΔE at the crossing seam were also computed.

5.7.1 The energy barrier

As expected on the basis of the considerations reported in section 5.6, since in the NEVPT2 scheme the dependence of $\hat{\mathcal{H}}_0$ on the orbital energies is limited to the inactive (core and virtual) orbitals, the strategy of enlarging the active space alleviates the problem around the symmetric D_{2d} geometry in the standard PT2 treatment. Therefore we notice that, with the minimal basis set, the barrier goes from a slightly negative value, $\simeq$ -2.5 kJ/mol, with the CAS(7/4) to a slightly positive value, $\simeq$ 3 kJ/mol, with the largest active space; we recall that the corresponding value, computed with the minimal CAS(3/2) space (see section 5.5), amounts about to -5 kJ/mol. As shown by the energy profiles shown in Fig. 5.9, such little benefit is however made completely fruitless when the dimension of the basis is increased and, even with the DZ basis set, a negative energy barrier is again obtained with the CAS(11/10) (see Tab. 5.4). To clarify this behavior, it is worthwhile to point out that going from the minimal SZ basis to the DZ one produces a reduction in the energy gap between the occupied orbitals, which are shifted to higher energies, and the virtual orbitals, whose energies are, instead, brought down. This effect makes the system more sensitive to the change of the energy differences in proximity of the symmetric D_{2d} point, undoing, therefore, the slight improvement obtained by the enlargement of the CAS dimensions. Such phenomenon, although still present, is certainly less pronounced going from the DZ to DZP and then to the TZP basis sets.

Moreover, as shown by a first comparison between the results in Tabs. 5.3 and 5.4 and those in Tab. 5.5, the third order computation is unable to completely

Table 5.3: Spiro cation–CAS(7/4): NEVPT2(can), NEVPT3(can), NEVPT2(av) energies (kJ/mol) of the ground state, $^2A_2(1)$, at $\xi = 0.0$ and of the first excited state, $^2A_2(2)$, at $\xi = 0.0$ and $\xi = -0.5$. All the energies are computed with respect to the energy of the ground state at $\xi = -0.5$. For the sake of clarity the energy splitting (ΔE kJ/mol) between the two states at $\xi = 0.0$ is also reported.

			NEVPT(can)			NEVPT2(av)	
	States	CASSCF	SC-PT2	PC-PT2	SC-PT3	SC-PT2	PC-PT2
			SZ basis set				
$\xi = -0.5$	$^2A_2(2)$	56.69	51.50	51.49	51.32	49.63	49.50
$\xi = 0.0$	$^2A_2(1)$	8.33	-2.15	-2.89	5.03	4.98	4.76
	$^2A_2(2)$	17.37	7.56	6.79	14.23	14.67	14.42
ΔE		9.04	9.71	9.68	9.20	9.70	9.66
			DZ basis set				
$\xi = -0.5$	$^2A_2(2)$	45.82	38.82	38.71	42.94	40.53	40.36
$\xi = 0.0$	$^2A_2(1)$	5.64	-7.82	-8.57	8.33	4.68	4.45
	$^2A_2(2)$	15.63	2.69	1.91	18.33	15.04	15.03
ΔE		9.99	10.52	10.47	10.00	10.36	10.58
			DZP basis set				
$\xi = -0.5$	$^2A_2(2)$	46.38	36.47	36.34		38.00	37.73
$\xi = 0.0$	$^2A_2(1)$	6.53	-11.70	-12.53		4.96	4.85
	$^2A_2(2)$	16.19	-1.31	-2.19		15.33	15.44
ΔE		9.66	10.38	10.33		10.36	10.59
			TZP basis set				
$\xi = -0.5$	$^2A_2(2)$	46.14	36.43	36.33		38.72	38.44
$\xi = 0.0$	$^2A_2(1)$	6.75	-11.54	-12.39		6.50	6.42
	$^2A_2(2)$	16.38	-1.23	-2.17		17.15	16.99
ΔE		9.63	10.31	10.23		10.66	10.57

restore the correct shape of the curve. Indeed, one can appreciate that, while a good accordance between the NEVPT3(can) and NEVPT2(av) results is obtained when the NEVPT2(can) barrier is just slightly negative (see CAS(7/4)/SZ and CAS(11/10) values in Tabs. 5.3 and 5.4), the third order correction tends to overestimate the depth of the well when the NEVPT2(can) gives considerably wrong results. Indeed, with CAS(7/4) and DZ basis set, where the NEVPT2(can) predicts the D_{2d} point to be about 8 kJ/mol below the C_{2v} minimum, the energy barrier is estimated to be about 8 kJ/mol at NEVPT3(can) level, whereas a value amounting to $\simeq 4.5$ kJ/mol is obtained with the NEVPT2(av) approach; such value is corroborated by the MRCI

Table 5.4: Spiro cation–CAS(11/10): NEVPT2(can), NEVPT3(can), NEVPT2(av) energies (kJ/mol) of the ground state, $^2A_2(1)$, at $\xi = 0.0$ and of the first excited state, $^2A_2(2)$, at $\xi = 0.0$ and $\xi = -0.5$. All the energies are computed with respect to the energy of the ground state at $\xi = -0.5$. For the sake of clarity the energy splitting (ΔE kJ/mol) between the two states at $\xi = 0.0$ is also reported.

			NEVPT(can)			NEVPT2(av)	
	States	CASSCF	SC-PT2	PC-PT2	SC-PT3	SC-PT2	PC-PT2
			SZ basis set				
$\xi = -0.5$	$^2A_2(2)$	55.51	47.34	47.13	48.34	46.93	46.76
$\xi = 0.0$	$^2A_2(1)$	7.99	3.13	3.01	5.33	5.62	5.49
	$^2A_2(2)$	15.40	11.41	11.39	13.52	13.88	13.86
ΔE		7.41	8.28	8.38	8.19	8.27	8.37
			DZ basis set				
$\xi = -0.5$	$^2A_2(2)$	47.61	34.93	34.49	39.71	36.29	35.73
$\xi = 0.0$	$^2A_2(1)$	6.92	-1.40	-3.21	6.33	5.17	4.02
	$^2A_2(2)$	15.45	7.75	5.89	15.40	14.33	13.13
ΔE		8.53	9.15	9.10	9.07	9.16	9.11
			DZP basis set				
$\xi = -0.5$	$^2A_2(2)$	47.10	32.99	32.54		34.10	33.60
$\xi = 0.0$	$^2A_2(1)$	7.04	-4.96	-6.92		5.18	4.22
	$^2A_2(2)$	15.55	4.21	2.17		14.45	13.40
ΔE		8.51	9.18	9.10		9.27	9.18
			TZP basis set				
$\xi = -0.5$	$^2A_2(2)$	46.66	33.21	32.81		36.90	36.47
$\xi = 0.0$	$^2A_2(1)$	7.17	-4.85	-6.61		7.16	6.34
	$^2A_2(2)$	15.62	4.24	2.40		16.39	15.48
ΔE		8.45	9.09	9.01		9.22	9.15

results [158], which estimate the height of the barrier to be about 4.5 kJ/mol (see the DZ values reported in Tab. 5.5). These considerations, apart from the expensiveness of the third order calculations, that makes this strategy not efficiently applicable to large–sized MV systems, confirm the NEVPT2(av) technique as a valuable and efficient approach to study the ET process in this class of compounds. The reliability and the firmness of the new proposed perturbative strategy is further assessed by the good accordance shown by the results obtained with the two different active spaces employed: the height of the barrier is computed to be in the range 4-5 kJ/mol with the three smallest basis sets and to be $\simeq$ 6 kJ/mol with the TZP basis. These

Table 5.5: Spiro cation–CAS(7/4): CAS+SD$_{can}$ and C-CAS+SD$_{can}$ energies (kJ/mol) of the ground state, $^2A_2(1)$, at $\xi = 0.0$ and of the first excited state, $^2A_2(2)$, at $\xi = 0.0$ and $\xi = -0.5$. The values have been obtained from the values reported in Ref. [158], taking as the zero energy the that of the ground state $^2A_2(1)$ at $\xi = -0.5$. See Ref. [158] for further details.

	States	CAS+SD$_{can}$	C-CAS+SD$_{can}$	CAS+SD$_{can}$	C-CAS+SD$_{can}$
		SZ basis set		DZ basis set	
$\xi = -0.5$	$^2A_2(2)$	53.80	53.76	43.86	44.00
$\xi = 0.0$	$^2A_2(1)$	6.48	6.68	4.41	4.67
	$^2A_2(2)$	15.72	16.01	14.60	14.96
ΔE		9.25	9.32	10.19	10.29

values are in reasonable accordance with the results of the more correlated MRCI calculations (Tab. 5.5): here, with the CAS(7/4), the barrier is computed, both at the internally–contracted [48] (C-CAS+SD) and uncontracted CAS+SD level, to be about 6.5 kJ/mol (SZ) and 4.5 kJ/mol (DZ).

5.7.2 The energy splitting

As appears from the results in Tabs. 5.3 and 5.4, the energy splitting ΔE at the crossing seam, being twice the value of the electronic coupling $\mathcal{H}_{ab}$, is essentially not affected by the wrong behavior of the standard PT2 approach. One can indeed notice a remarkable agreement between the values provided by the NEVPT2(can) calculations and those attained at NEVPT3(can) and NEVPT2(av) levels. A small effect of the dynamical correlation is also evident, since a reasonable estimate of this parameter is already obtained at CASSCF level. Moreover, as also found at MRCI level [158], this energy difference shows practically no dependence on the basis set dimension (with the exception of a small underestimation with the minimal basis) since a value of $\simeq$ 9 kJ/mol is computed with the CAS(11/10) and $\simeq$ 10 kJ/mol with the CAS(7/4). These values for ΔE are in noticeable accordance with those computed in Ref. [158] and reported in Tab. 5.5, where the splitting, with the larger basis set, is calculated to be 10.2 and 10.3 kJ/mol at uncontracted CAS+SD and internally contracted C-CAS+SD levels respectively. Then, very similar values were also obtained in the previous calculations by Sanz *et al.* [176]: the splitting was computed to be 9.5 (DFT), 11.0 (UHF) and 11.9 kJ/mol (DDCI). Then, a simple way to get a first estimate of the energy splitting between the two adiabatic surfaces at the crossing seam is to apply Koopmans' theorem [8, 9]. Since, within a single–determinant approximation, the two electronic configurations corresponding to the

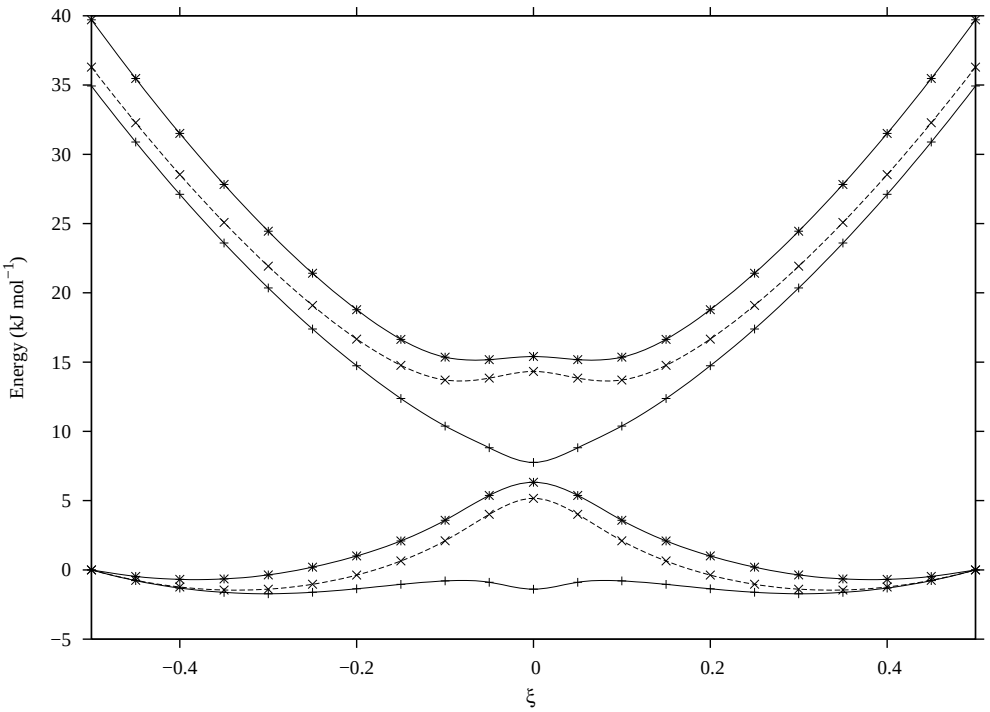

Figure 5.9: SC-NEVPT2(can), SC-NEVPT3(can) (full lines with "+" and "∗" points respectively) and SC-NEVPT2(av) (dashed lines with "×"points) energy profiles of the ground, $^2A_2(1)$, and of the first excited state, $^2A_2(2)$, of the spiro monocation. All the PES have been shifted in order to have the two C_{2v} minima at zero energy (see text for computational details).

ground state of the monocation and to its first excited state can be obtained from two appropriate ionization processes from the closed–shell configuration, ΔE can be approximated by the difference in the RHF energies of the HOMO and HOMO-1 orbitals of the neutral system at the symmetrical geometry. The values computed using such a rough approach provide results in good agreement with those obtained at higher levels of calculations: the splitting is indeed calculated to be 9.98 (SZ), 10.76 (DZ), 10.50 (DZP) and 10.24 kJ/mol (TZP).

5.7.3 Excitation energy to the $^2A_2(2)$ state

The other key parameter in the study of the ET process is the excitation energy corresponding to the optically–induced ET, namely the vertical excitation energy from the ground state at its charge-localized minimum to the first excited state. We recall that in the simple Hush's approach [169,170], for MV systems characterized by a weak electronic coupling, this quantity equals the reorganization energy λ. As is apparent from the results in Tabs. 5.3 and 5.4, this energy difference appears to be

much more sensitive to the correlation energy, as well as to the dimension of the basis set, than the above discussed ΔE. Overall, a small and progressive reduction can be observed going from the minimal basis to the largest one; while this reduction is sizable when passing from SZ to DZ (slightly less than 10 kJ/mol), it tends to become negligible proceeding up to the DZP and TZP basis sets. The same trend was found at MRCI level [158] and, as shown in Tab. 5.5, the excitation energy of the $^2A_2(2)$ state, at the C_{2v} minimum, decreases by $\simeq$ 10 kJ/mol when increasing the basis set dimension. Furthermore, one can notice that also the enlargement of the active space results in a similar small lowering in the energy, anyway not exceeding 4 kJ/mol. Finally, referring to the results obtained with the same active space and basis sets (CAS(7/4)/SZ, DZ), a good accordance, up to within 5 kJ/mol, was achieved between the MRCI computations [158] and the present NEVPT3(can) and NEVPT2(av) results.

Appendix A

PC-NEVPT2 $S_l^{(k)}$ spaces

A.0.4 The $\mathbf{S^{(0)}_{ij,rs}}$ Space

The $\hat{V}^{(0)}_{ij,rs}$ operator has the form

$$\hat{V}^{(0)}_{ij,rs} = \gamma_{ij}\gamma_{rs}\left(\langle rs|ij\rangle E_{ri}E_{sj} + \langle rs|ji\rangle E_{rj}E_{si}\right) \qquad i \leq j, r \leq s, \tag{A.1}$$

where $\gamma_{mn} = 1 - \frac{1}{2}\delta_{mn}$.
The perturbation function is written as

$$\Psi^{(0)}_{ri,sj} = \frac{\gamma_{ij}\gamma_{rs}}{\sqrt{N^{(0)}_{ij,rs}}}(\langle rs|ij\rangle\, E_{ri}E_{sj} + \langle rs|ji\rangle\, E_{si}E_{rj})\Psi^{(0)}_m \tag{A.2}$$

with the norm given by

$$N^{(0)}_{ij,rs} = 4\gamma_{ij}\gamma_{rs}(\langle rs|ij\rangle^2 + \langle rs|ji\rangle^2 - \langle rs|ij\rangle\,\langle rs|ji\rangle). \tag{A.3}$$

Finally, the perturbative coefficient $c^{(0)(1)}_{ij,rs}$ is

$$C^{(0)(1)}_{ij,rs} = -\frac{\sqrt{N^{(0)}_{ij,rs}}}{\epsilon_r + \epsilon_s - \epsilon_i - \epsilon_j}. \tag{A.4}$$

A.0.5 The $\mathbf{S^{(-1)}_{i,rs}}$ Space

This space, corresponding to an excitation of one electron from the core to the virtual space and of another electron from the active again to the virtual space, is spanned by the IC functions $\Phi_{risa} = E_{ri}E_{sa}\Psi^{(0)}_m$ and $\Phi_{sira} = E_{si}E_{ra}\Psi^{(0)}_m$ with the inactive indices $r \leq s$.
For each set of three "rsi" indices, two different orthonormal eigenfunctions (per-

turbers) corresponding to the same eigenvalue ${E_{irs,\mu}}^{(-1)}$ can be defined:

$$\Psi^{(-1)}_{ris,\mu} = \frac{1}{\sqrt{2}} \sum_{a}^{act} (\Phi_{risa} + \Phi_{sira}) c_{a,\mu} \tag{A.5}$$

$$\Psi'^{(-1)}_{ris,\mu} = \frac{1}{\sqrt{6}} \sum_{a}^{act} (\Phi_{risa} - \Phi_{sira}) c_{a,\mu} \tag{A.6}$$

The perturbative coefficients are:

$$C^{(-1)(1)}_{ris,\mu} = -\frac{(rs,\mu i)}{\epsilon_r + \epsilon_s - \epsilon_i + \epsilon_\mu} \tag{A.7}$$

and

$$C^{(-1)(1)'}_{ris,\mu} = -\frac{(rs,\mu i)'}{\epsilon_r + \epsilon_s - \epsilon_i + \epsilon_\mu} \tag{A.8}$$

respectively; the quantities indicated with $(rs,\mu i)$ and $(rs,\mu i)'$ are instead computed as

$$(rs,\mu i) = \frac{1}{\sqrt{2}} \sum_{a}^{act} (\langle rs|ia\rangle + \langle sr|ia\rangle) S_{a,\mu} \tag{A.9}$$

$$(rs,\mu i)' = \sqrt{\frac{3}{2}} \sum_{a}^{act} (\langle rs|ia\rangle - \langle sr|ia\rangle) S_{a,\mu} \tag{A.10}$$

with

$$S_{a,\mu} = \sum_{a'}^{act} c^*_{a',\mu} R^{(1)}_{a',a} \tag{A.11}$$

$R^{(1)}_{a',a}$ being the one-particle spinless density matrix.
In the case of $r = s$ one has to consider only

$$C^{(-1)(1)}_{rir,\mu} = -\frac{(rr,\mu i)}{2\epsilon_r - \epsilon_i + \epsilon_\mu} \tag{A.12}$$

with

$$(rr,\mu i) = \sum_{a}^{act} \langle rr|ia\rangle \, S_{a,\mu}. \tag{A.13}$$

A.0.6 The $\mathbf{S^{(1)}_{ij,r}}$ Space

The treatment of this subspace, where two core electrons are excited to the active and virtual spaces respectively, is analogous to the previous one. The space is defined by the functions $\Phi_{rjai} = E_{rj}E_{ai}\Psi^{(0)}_m$ and $\Phi_{riaj} = E_{ri}E_{aj}\Psi^{(0)}_m$ with $i \leq j$. The two

orthogonal functions are:

$$\Psi^{(-1)}_{rji,\mu} = \frac{1}{\sqrt{2}} \sum_{a}^{act} (\Phi_{rjai} + \Phi_{riaj}) c_{a,\mu} \tag{A.14}$$

$$\Psi'^{(-1)}_{rji,\mu} = \frac{1}{\sqrt{6}} \sum_{a}^{act} (\Phi_{rjai} - \Phi_{riaj}) c_{a,\mu}. \tag{A.15}$$

Analogously, the perturbative coefficients are defined as

$$C^{(-1)(1)}_{rji,\mu} = -\frac{(ji, r\mu)}{\epsilon_r - \epsilon_i - \epsilon_j + \epsilon_\mu} \tag{A.16}$$

$$C^{(-1)(1)'}_{rji,\mu} = -\frac{(ji, r\mu)'}{\epsilon_r - \epsilon_i - \epsilon_j + \epsilon_\mu}. \tag{A.17}$$

$(ji, r\mu)$ and $(ji, r\mu)'$ are defined exactly as in eqs.A.18 and A.19 with the replacement of a virtual index with a core index:

$$(ij, r\mu) = \frac{1}{\sqrt{2}} \sum_{a}^{act} (\langle ra|ji\rangle + \langle ra|ij\rangle) S_{a,\mu} \tag{A.18}$$

$$(ij, r\mu)' = \sqrt{\frac{3}{2}} \sum_{a}^{act} (\langle ra|ji\rangle - \langle ra|ij\rangle) S_{a,\mu} \tag{A.19}$$

with

$$S_{a,\mu} = \sum_{a'}^{act} c^*_{a',\mu} \tilde{R}^{(1)}_{a',a} \tag{A.20}$$

where $\tilde{R}^{(1)}_{a',a}$ is the one-hole spinless density matrix.
If $i = j$, as previously seen, one has only $C^{(-1)(1)}_{rii,\mu}$ with $(ii, r\mu)$.

A.0.7 The $\mathbf{S^{(-2)}_{rs}}$ Space

For the case $r < s$ the $S^{(-2)}_{rs}$ space is generated by the functions $\Phi_{rsab} = E_{rb} E_{sa} \Psi^{(0)}_m$. The perturbation functions are

$$\Psi^{(-2)}_{rs,\mu} = \sum_{ab}^{act} = \Phi_{rsab} c_{ab,\mu}. \tag{A.21}$$

and the perturbative coefficients

$$C^{(-2)(1)}_{rs,\mu} = -\frac{(rs, \mu)}{\epsilon_r + \epsilon_s + \epsilon_\mu} \tag{A.22}$$

with

$$(rs, \mu) = \sum_{ab}^{act} \langle rs|ba\rangle \, S_{ab,\mu} \tag{A.23}$$

and $S_{ab,\mu} = \sum_{a'b'} c^*_{a'b',\mu} R^{(2)}_{a'b',ab}$.

For the case $r = s$, since

$$\Psi^{(=)}_{rrab} E_{ra} E_{rb} \Psi^{(0)}_m = E_{rb} E_{ra} \Psi^{(0)}_m = \Phi_{rrba} \tag{A.24}$$

we note that the $S^{(-2)}_{rr}$ space has dimension $n_{act}(n_{act}+1)/2$ instead of n^2_{act} as in the case with $r < s$, therefore we have

$$\Psi^{(-2)}_{rr,\mu} = \sum_{a \geq b}^{act} \Phi_{rr,ab} c'_{ab,\mu}. \tag{A.25}$$

The perturbative coefficients are:

$$C^{(-2)(1)}_{rr,\mu} = -\frac{(rr,\mu)}{2\epsilon_r + \epsilon'_\mu} \tag{A.26}$$

with

$$(rr,\mu) = \sum_{ab}^{act} = \langle rr|ba\rangle \, S'_{ab,\mu} \tag{A.27}$$

and

$$S'_{ab,\mu} = \frac{1}{2} \sum_{a'b'}^{act} c^*_{a'b',\mu} (R^{(2)}_{a'b',ab} + R^{(2)}_{a'b',ba}) \tag{A.28}$$

where $R^{(2)}$ is the two-particle spinless density matrix.

A.0.8 The $S^{(2)}_{ij}$ Space

Obviously, this case is exactly analogous to the previous one, with the replacement of the two-particle spinless density matrix $R^{(2)}$ with the two-hole spinless density matrix $\tilde{R}^{(2)}$. Here, we shall limit ourselves to list the principal formulas. With $i \leq j$, one has:

$$\Psi^{(2)}_{ij,\mu} = \sum_{ab}^{act} \Phi_{ijab} c_{ab,\mu} \tag{A.29}$$

with $\Phi_{ijab} = E_{bi} E - aj \Psi^{(0)}_m$.

$$C^{(2)(1)}_{ij,\mu} = -\frac{(\mu,ij)}{\epsilon_\mu - \epsilon_i - \epsilon_j} \tag{A.30}$$

If $i = j$, instead, one has

$$\Psi^{(2)}_{ii,\mu} = \sum_{a \geq b}^{act} \Phi_{iiab} c'_{ab,\mu}. \tag{A.31}$$

with $\Phi_{iiab} = E_{bi} E_{ai} \Psi^{(0)}_m$. The coefficients are:

$$C^{(2)(1)'}_{ii,\mu} = -\frac{(\mu,ii)}{p\epsilon_\mu - 2\epsilon_i}. \tag{A.32}$$

A.0.9 The $S^{(0)}_{i,r}$ Space

This subspace is spanned by the functions $\Phi_{riab} = E_{ri}E_{ab}\Psi^{(0)}_m$ and $\Phi_{riab}{}' = E_{ai}E_{rb}\Psi^{(0)}_m$. The single excitations from the core to the virtual space $E_{ri}\Psi^{(0)}_m$ are already considered, since $\sum_a^{act} E_{ri}E_{aa}\Psi^{(0)}_m = n_{act}E_{ri}\Psi^{(0)}_m$.
The perturbation functions are:

$$\Psi^{(0)}_{ir,\mu} = \sum_{ab}^{act}(\Phi_{riab}c_{ab,\mu} + \Phi'_{riab}c'_{ab,\mu}) \tag{A.33}$$

and the coefficients:

$$C^{(0)(1)}_{ir,\mu} = -\frac{(ri,\mu) + (ri,\mu)'}{\epsilon_\mu + \epsilon_r - \epsilon_i} \tag{A.34}$$

A.0.10 The $S^{(-1)}_{r}$ Space

The $S^{(-1)}_r$ space, providing for an excitation within the active space and the promotion of an active electron to the virtual space, is generated by the functions $\Phi_{rbac} = E_{rb}E_{ac}\Psi^{(0)}_m$ and the eigenfunctions of the Dyall's Hamiltonian $\hat{\mathcal{H}}^D$ are expressed as

$$\Psi^{(-1)}_{r,\mu} = \sum_{abc}^{act}\Phi_{rbac}c_{abc,\mu} \tag{A.35}$$

and the form of the perturbative coefficients is

$$C^{(-1)(1)}_{r,\mu} = -\frac{(r,\mu)}{\epsilon_\mu + \epsilon_r} \tag{A.36}$$

A.0.11 The $S^{(1)}_{i}$ Space

The treatment of this subspace closely follows that previously seen for the $S^{(-1)}_r$ subspace. One has to consider the functions $\Phi_{iabc} = E_{bi}E_{ac}\Psi^{(0)}_m$ and by diagonalization of $\hat{\mathcal{H}}^D$ within this subspace one obtains the perturbers $\Psi^{(1)}_{i,\mu}$ written as

$$\Psi^{(1)}_{i,\mu} = \sum_{abc}^{act}\Phi_{iabc}c_{abc,\mu} \tag{A.37}$$

and from the interaction of $\Psi^{(1)}_{i,\mu}$ with $\Psi^{(0)}_m$ one can compute the coefficients $C^{(1)(1)}_{i,\mu}$ as

$$C^{(1)(1)}_{i,\mu} = -\frac{(i,\mu)}{\epsilon_\mu - \epsilon_i}. \tag{A.38}$$

Appendix B

Matrix elements of PC-NEVPT3

B.0.12 V(0)V(0) Class

Obviously, for the monodimensional $S^{(0)}_{ij,rs}$ space the "partially contracted" approach is coincident with the "strongly contracted" one and therefore the third order contribution from $V(0)V(0)$ class is

$$E^{(3)} = \sum_{i'\leq j'}^{core}\sum_{r'\leq s'}^{virt}\sum_{i\leq j}^{core}\sum_{r\leq s}^{virt} C^{(0)(1)}_{i'j',r's'} C^{(0)(1)}_{ij,rs} \left\langle \Psi^{(0)}_{i'j',r's'} \middle| \hat{\mathcal{H}} - \hat{\mathcal{H}}_0 \middle| \Psi^{(0)}_{ij,rs} \right\rangle \tag{B.1}$$

where the contribution of $\hat{\mathcal{H}}_0$ for the diagonal case is $\Delta\epsilon = \epsilon_i + \epsilon_j - \epsilon_r - \epsilon_s$. Given the form of the perturber

$$\Psi^{(0)}_{ij,rs} = (AE_{ri}E_{sj} + BE_{si}E_{rj})\Psi^{(0)}_m \tag{B.2}$$

with $A = \frac{\gamma_{ij}\gamma_{rs}}{\sqrt{N^{(0)}_{ij,rs}}} \langle rs|ij\rangle$ and $B = \frac{\gamma_{ij}\gamma_{rs}}{\sqrt{N^{(0)}_{ij,rs}}} \langle rs|ji\rangle$. The matrix element in eq.B.1 can be rewritten as follows

$$\begin{aligned}
\left\langle \Psi^{(0)}_{i'j',r's'} \middle| \hat{\mathcal{H}} \middle| \Psi^{(0)}_{ij,rs} \right\rangle = & \underbrace{\left\langle \Psi^{(0)}_m \middle| E_{j's'}E_{i'r'}\hat{\mathcal{H}}E_{ri}E_{sj} \middle| \Psi^{(0)}_m \right\rangle}_{val1} A^2 \\
& + \underbrace{\left\langle \Psi^{(0)}_m \middle| E_{j's'}E_{i'r'}\hat{\mathcal{H}}E_{si}E_{rj} \middle| \Psi^{(0)}_m \right\rangle}_{val2} A*B \\
& + \underbrace{\left\langle \Psi^{(0)}_m \middle| E_{j'r'}E_{i's'}\hat{\mathcal{H}}E_{ri}E_{sj} \middle| \Psi^{(0)}_m \right\rangle}_{val3} B*A \\
& + \underbrace{\left\langle \Psi^{(0)}_m \middle| E_{j'r'}E_{i's'}\hat{\mathcal{H}}E_{si}E_{rj} \middle| \Psi^{(0)}_m \right\rangle}_{val4} B^2
\end{aligned} \tag{B.3}$$

where the four terms $val1$, $val2$, $val3$ and $val4$ are evaluated by the subroutines `Ejpspiprp_risj` produced by FRODO.

B.0.13 V(0)V(1) Class

Since, given the i, j, r indices, two orthonormal perturbation functions are defined

$$\Psi^{(1)}_{rji,\mu} = \frac{1}{\sqrt{2}} \sum_{a}^{act} (E_{rj}E_{ai} + E_{ri}E_{aj})\Psi^{(0)}_{m} c_{a,\mu} \tag{B.4}$$

$$\Psi^{'(1)}_{rji,\mu} = \frac{1}{\sqrt{6}} \sum_{a}^{act} (E_{rj}E_{ai} - E_{ri}E_{aj})\Psi^{(0)}_{m} c_{a,\mu}. \tag{B.5}$$

two different matrix elements have to be considered. Moreover, it is necessary to distinguish the case $i = j$, for which the perturber is

$$\Psi^{(1)}_{rii\mu} = \sum_{a}^{act} E_{ri}E_{ai}\Psi^{(0)}_{m} c_{a,\mu} \tag{B.6}$$

and the perturbative coefficient $C^{(1)(1)}_{ijr}$ is different.

$$\begin{aligned}
\left\langle \Psi^{(1)}_{r'i'j'\mu} \middle| \hat{\mathcal{H}} \middle| \Psi^{(0)}_{ij,rs} \right\rangle = \frac{1}{\sqrt{2}} \sum_{a}^{act} & \underbrace{\left\langle \Psi^{(0)}_{m} \middle| E_{i'a}E_{j'r'}\hat{\mathcal{H}}E_{ri}E_{sj} \middle| \Psi^{(0)}_{m} \right\rangle}_{\mathrm{val1}} A * c_{a\mu} \\
+ \frac{1}{\sqrt{2}} \sum_{a}^{act} & \underbrace{\left\langle \Psi^{(0)}_{m} \middle| E_{j'a}E_{i'r'}\hat{\mathcal{H}}E_{ri}E_{sj} \middle| \Psi^{(0)}_{m} \right\rangle}_{\mathrm{val2}} A * c_{a\mu} \\
+ \frac{1}{\sqrt{2}} \sum_{a}^{act} & \underbrace{\left\langle \Psi^{(0)}_{m} \middle| E_{i'a}E_{j'r'}\hat{\mathcal{H}}E_{si}E_{rj} \middle| \Psi^{(0)}_{m} \right\rangle}_{\mathrm{val3}} B * c_{a\mu} \\
+ \frac{1}{\sqrt{2}} \sum_{a}^{act} & \underbrace{\left\langle \Psi^{(0)}_{m} \middle| E_{j'a}E_{i'r'}\hat{\mathcal{H}}E_{si}E_{rj} \middle| \Psi^{(0)}_{m} \right\rangle}_{\mathrm{val4}} B * c_{a,\mu}
\end{aligned} \tag{B.7}$$

and

$$\left\langle \Psi^{\prime(1)}_{r'i'j'\mu} \middle| \hat{\mathcal{H}} \middle| \Psi^{(0)}_{ij,rs} \right\rangle = \frac{1}{\sqrt{6}} \sum_{a}^{act} \underbrace{\left\langle \Psi^{(0)}_{m} \middle| E_{i'a}E_{j'r'}\hat{\mathcal{H}}E_{ri}E_{sj} \middle| \Psi^{(0)}_{m} \right\rangle}_{\mathrm{val1}} A * c_{a\mu} \tag{B.8}$$

$$- \frac{1}{\sqrt{6}} \sum_{a}^{act} \underbrace{\left\langle \Psi^{(0)}_{m} \middle| E_{j'a}E_{i'r'}\hat{\mathcal{H}}E_{ri}E_{sj} \middle| \Psi^{(0)}_{m} \right\rangle}_{\mathrm{val2}} A * c_{a\mu}$$

$$+ \frac{1}{\sqrt{6}} \sum_{a}^{act} \underbrace{\left\langle \Psi^{(0)}_{m} \middle| E_{i'a}E_{j'r'}\hat{\mathcal{H}}E_{si}E_{rj} \middle| \Psi^{(0)}_{m} \right\rangle}_{\mathrm{val3}} B * c_{a\mu}$$

$$- \frac{1}{\sqrt{6}} \sum_{a}^{act} \underbrace{\left\langle \Psi^{(0)}_{m} \middle| E_{j'a}E_{i'r'}\hat{\mathcal{H}}E_{si}E_{rj} \middle| \Psi^{(0)}_{m} \right\rangle}_{\mathrm{val4}} B * c_{a,\mu}$$

For the case $i' = j'$ one has

$$\left\langle \Psi^{(1)}_{r'i'i'\mu} \middle| \hat{\mathcal{H}} \middle| \Psi^{(0)}_{ij,rs} \right\rangle = \sum_{a}^{act} \underbrace{\left\langle \Psi^{(0)}_{m} \middle| E_{i'a}E_{i'r'}\hat{\mathcal{H}}E_{ri}E_{sj} \middle| \Psi^{(0)}_{m} \right\rangle}_{\mathrm{val1}} A * c_{a\mu} \tag{B.9}$$

$$+ \sum_{a}^{act} \underbrace{\left\langle \Psi^{(0)}_{m} \middle| E_{i'a}E_{i'r'}\hat{\mathcal{H}}E_{si}E_{rj} \middle| \Psi^{(0)}_{m} \right\rangle}_{\mathrm{val3}} B * c_{a\mu}$$

B.0.14 V(0)V(−1) Class

Obviously, the treatment of this class parallels the previous one with the two orthonormal perturbers, for the case $r \neq s$, being

$$\Psi^{(-1)}_{ris\mu} = \frac{1}{\sqrt{2}} \sum_{a}^{act} (E_{ri}E_{sa} + E_{si}E_{ra})\Psi^{(0)}_{m} c_{a,\mu} \tag{B.10}$$

$$\Psi^{\prime(-1)}_{ris\mu} = \frac{1}{\sqrt{6}} \sum_{a}^{act} (E_{ri}E_{sa} - E_{si}E_{ra})\Psi^{(0)}_{m} c_{a,\mu}. \tag{B.11}$$

Analogously to eq.B.30, when the two virtual indices are coincident ($r = s$) the perturber is

$$\Psi^{(1)}_{rir\mu} = \sum_{a}^{act} E_{ri}E_{ra}\Psi^{(0)}_{m} c_{a,\mu} \tag{B.12}$$

In the former case ($r \neq s$), two matrix elements have to be computed:

$$\left\langle \Psi^{(-1)}_{r'i's'\mu} \middle| \hat{\mathcal{H}} \middle| \Psi^{(0)}_{ij,rs} \right\rangle = \frac{1}{\sqrt{2}} \sum_a^{act} \underbrace{\left\langle \Psi^{(0)}_m \middle| E_{as'} E_{i'r'} \hat{\mathcal{H}} E_{ri} E_{sj} \middle| \Psi^{(0)}_m \right\rangle}_{\mathrm{val}1} A * c_{a\mu} \tag{B.13}$$
$$+ \frac{1}{\sqrt{2}} \sum_a^{act} \underbrace{\left\langle \Psi^{(0)}_m \middle| E_{ar'} E_{i's'} \hat{\mathcal{H}} E_{ri} E_{sj} \middle| \Psi^{(0)}_m \right\rangle}_{\mathrm{val}2} A * c_{a\mu}$$
$$+ \frac{1}{\sqrt{2}} \sum_a^{act} \underbrace{\left\langle \Psi^{(0)}_m \middle| E_{as'} E_{i'r'} \hat{\mathcal{H}} E_{si} E_{rj} \middle| \Psi^{(0)}_m \right\rangle}_{\mathrm{val}3} B * c_{a\mu}$$
$$+ \frac{1}{\sqrt{2}} \sum_a^{act} \underbrace{\left\langle \Psi^{(0)}_m \middle| E_{ar'} E_{i's'} \hat{\mathcal{H}} E_{si} E_{rj} \middle| \Psi^{(0)}_m \right\rangle}_{\mathrm{val}4} B * c_{a,\mu}$$

$$\left\langle \Psi^{(-1)}_{r'i's'\mu} \middle| \hat{\mathcal{H}} \middle| \Psi^{(0)}_{ij,rs} \right\rangle = \frac{1}{\sqrt{6}} \sum_a^{act} \underbrace{\left\langle \Psi^{(0)}_m \middle| E_{as'} E_{i'r'} \hat{\mathcal{H}} E_{ri} E_{sj} \middle| \Psi^{(0)}_m \right\rangle}_{\mathrm{val}1} A * c_{a\mu} \tag{B.14}$$
$$- \frac{1}{\sqrt{6}} \sum_a^{act} \underbrace{\left\langle \Psi^{(0)}_m \middle| E_{ar'} E_{i's'} \hat{\mathcal{H}} E_{ri} E_{sj} \middle| \Psi^{(0)}_m \right\rangle}_{\mathrm{val}2} A * c_{a\mu}$$
$$+ \frac{1}{\sqrt{6}} \sum_a^{act} \underbrace{\left\langle \Psi^{(0)}_m \middle| E_{as'} E_{i'r'} \hat{\mathcal{H}} E_{si} E_{rj} \middle| \Psi^{(0)}_m \right\rangle}_{\mathrm{val}3} B * c_{a\mu}$$
$$- \frac{1}{\sqrt{6}} \sum_a^{act} \underbrace{\left\langle \Psi^{(0)}_m \middle| E_{ar'} E_{i's'} \hat{\mathcal{H}} E_{si} E_{rj} \middle| \Psi^{(0)}_m \right\rangle}_{\mathrm{val}4} B * c_{a,\mu}$$

For $r = s$ the interaction reduces to

$$\left\langle \Psi^{(-1)}_{r'i'r'\mu} \middle| \hat{\mathcal{H}} \middle| \Psi^{(0)}_{ij,rs} \right\rangle = \sum_a^{act} \underbrace{\left\langle \Psi^{(0)}_m \middle| E_{ar'} E_{i'r'} \hat{\mathcal{H}} E_{ri} E_{sj} \middle| \Psi^{(0)}_m \right\rangle}_{\mathrm{val}1} A * c_{a\mu} \tag{B.15}$$
$$+ \sum_a^{act} \underbrace{\left\langle \Psi^{(0)}_m \middle| E_{ar'} E_{i'r'} \hat{\mathcal{H}} E_{si} E_{rj} \middle| \Psi^{(0)}_m \right\rangle}_{\mathrm{val}3} B * c_{a\mu}$$

B.0.15 V(0)V(2) Class

Two cases have to be considered:

1. $i \neq j \rightarrow \Psi^{(2)}_{ij\mu} = \sum_{ab}^{act} E_{bi}E_{aj}\Psi^{(0)}_m c_{ab\mu}$
2. $i = j \rightarrow \Psi^{(2)}_{ij\mu} = \sum_{a\leq b}^{act} E_{bi}E_{ai}\Psi^{(0)}_m c'_{ab\mu}$

Therefore, the matrix elements are

$$\begin{aligned}\left\langle \Psi^{(2)}_{i'j'\mu} \middle| \hat{\mathcal{H}} \middle| \Psi^{(0)}_{ij,rs} \right\rangle = &\sum_{ab}^{act} \underbrace{\left\langle \Psi^{(0)}_m \middle| E_{j'a}E_{i'b}\hat{\mathcal{H}}E_{ri}E_{sj} \middle| \Psi^{(0)}_m \right\rangle}_{\mathrm{val1}} A * c_{a\mu} \\ &+ \sum_{ab}^{act} \underbrace{\left\langle \Psi^{(0)}_m \middle| E_{j'a}E_{i'b}\hat{\mathcal{H}}E_{si}E_{rj} \middle| \Psi^{(0)}_m \right\rangle}_{\mathrm{val2}} B * c_{a\mu}\end{aligned} \tag{B.16}$$

and

$$\begin{aligned}\left\langle \Psi^{(2)}_{i'i'\mu} \middle| \hat{\mathcal{H}} \middle| \Psi^{(0)}_{ij,rs} \right\rangle = &\sum_{a\leq b}^{act} \underbrace{\left\langle \Psi^{(0)}_m \middle| E_{i'a}E_{i'b}\hat{\mathcal{H}}E_{ri}E_{sj} \middle| \Psi^{(0)}_m \right\rangle}_{\mathrm{val1}} A * c_{a\mu} \\ &+ \sum_{a\leq b}^{act} \underbrace{\left\langle \Psi^{(0)}_m \middle| E_{i'a}E_{i'b}\hat{\mathcal{H}}E_{si}E_{rj} \middle| \Psi^{(0)}_m \right\rangle}_{\mathrm{val2}} B * c_{a\mu}\end{aligned} \tag{B.17}$$

B.0.16 V(0)V(−2) Class

This class closely follows the $V(0)V(2)$ class previously examined. The perturbation functions are:

1. $r \neq s \rightarrow \Psi^{(-2)}_{rs\mu} = \sum_{ab}^{act} E_{rb}E_{sa}\Psi^{(0)}_m c_{ab\mu}$
2. $r = s \rightarrow \Psi^{(-2)}_{rs\mu} = \sum_{a\leq b}^{act} E_{rb}E_{ra}\Psi^{(0)}_m c'_{ab\mu}$

and the corresponding matrix elements can be written as

$$\begin{aligned}\left\langle \Psi^{(-2)}_{r's'\mu} \middle| \hat{\mathcal{H}} \middle| \Psi^{(0)}_{ij,rs} \right\rangle = &\sum_{ab}^{act} \underbrace{\left\langle \Psi^{(0)}_m \middle| E_{as'}E_{br'}\hat{\mathcal{H}}E_{ri}E_{sj} \middle| \Psi^{(0)}_m \right\rangle}_{\mathrm{val1}} A * c_{a\mu} \\ &+ \sum_{ab}^{act} \underbrace{\left\langle \Psi^{(0)}_m \middle| E_{as'}E_{br'}\hat{\mathcal{H}}E_{si}E_{rj} \middle| \Psi^{(0)}_m \right\rangle}_{\mathrm{val2}} B * c_{a\mu}\end{aligned} \tag{B.18}$$

and

$$\left\langle \Psi^{(-2)}_{r'r'\mu} \middle| \hat{\mathcal{H}} \middle| \Psi^{(0)}_{ij,rs} \right\rangle = \sum_{a\leq b}^{act} \underbrace{\left\langle \Psi^{(0)}_m \middle| E_{ar'}E_{br'}\hat{\mathcal{H}}E_{ri}E_{sj} \middle| \Psi^{(0)}_m \right\rangle}_{\text{val}1} A * c_{a\mu} + \sum_{a\leq b}^{act} \underbrace{\left\langle \Psi^{(0)}_m \middle| E_{ar'}E_{br'}\hat{\mathcal{H}}E_{si}E_{rj} \middle| \Psi^{(0)}_m \right\rangle}_{\text{val}2} B * c_{a\mu} \tag{B.19}$$

B.0.17 $\mathbf{V(0)V(0')}$ Class

For the $\bar{S}^{(0)}_{ir}$ subspace the perturbers have the form:

$$\Psi^{(0)}_{ir\mu} = \sum_{ab}^{act} E_{ri}E_{ab}\Psi^{(0)}_m c_{ab\mu} + \sum_{ab}^{act} E_a i E_r b \Psi^{(0)}_m c'_{ab\mu} \tag{B.20}$$

so, the interaction with the $\Psi^{(0)}_{ijrs}$ can be written as follows

$$\begin{aligned}\left\langle \Psi^{(0)}_{i'r'\mu} \middle| \hat{\mathcal{H}} \middle| \Psi^{(0)}_{ij,rs} \right\rangle = &\sum_{ab}^{act} \underbrace{\left\langle \Psi^{(0)}_m \middle| E_{ba}E_{i'r'}\hat{\mathcal{H}}E_{ri}E_{sj} \middle| \Psi^{(0)}_m \right\rangle}_{\text{val}1} c_{a\mu} * A \\ &+ \sum_{ab}^{act} \underbrace{\left\langle \Psi^{(0)}_m \middle| E_{br'}E_{i'a}\hat{\mathcal{H}}E_{ri}E_{sj} \middle| \Psi^{(0)}_m \right\rangle}_{\text{val}2} c'_{a\mu} * A \\ &+ \sum_{ab}^{act} \underbrace{\left\langle \Psi^{(0)}_m \middle| E_{ba}E_{i'r'}\hat{\mathcal{H}}E_{si}E_{rj} \middle| \Psi^{(0)}_m \right\rangle}_{\text{val}3} c_{a\mu} * B \\ &+ \sum_{ab}^{act} \underbrace{\left\langle \Psi^{(0)}_m \middle| E_{br'}E_{i'a'}\hat{\mathcal{H}}E_{si}E_{rj} \middle| \Psi^{(0)}_m \right\rangle}_{\text{val}4} c'_{a,\mu} * B\end{aligned} \tag{B.21}$$

B.0.18 $\mathbf{V(0)V(1')}$ Class

The perturbers belonging to the $\bar{S}^{(1)}_i$ subspace are

$$\Psi^{(1)}_{i\mu} = \sum_{abc}^{act} E_{bi}E_{ac}\Psi^{(0)}_m c_{abc\mu} \tag{B.22}$$

and the resulting matrix elements have the form

$$\left\langle \Psi^{(1)}_{i'\mu} \left| \hat{\mathcal{H}} \right| \Psi^{(0)}_{ij,rs} \right\rangle = \sum_{abc}^{act} \underbrace{\left\langle \Psi^{(0)}_{m} \left| E_{ca}E_{i'b}\hat{\mathcal{H}}E_{ri}E_{sj} \right| \Psi^{(0)}_{m} \right\rangle}_{\mathrm{val1}} A * c_{a\mu} + \sum_{abc}^{act} \underbrace{\left\langle \Psi^{(0)}_{m} \left| E_{ca}E_{i'b}\hat{\mathcal{H}}E_{si}E_{rj} \right| \Psi^{(0)}_{m} \right\rangle}_{\mathrm{val2}} B * c_{a\mu} \tag{B.23}$$

B.0.19 V(0)V(−1′) Class

Finally, the treatment of the $V(0)V(-1')$ class is analogous to that previously seen. Given the form of the perturbation functions

$$\Psi^{(-1)}_{r\mu} = \sum_{abc}^{act} E_{rb}E_{ac}\Psi^{(0)}_{m}c_{abc\mu} \tag{B.24}$$

the interaction is

$$\left\langle \Psi^{(-1)}_{r'\mu} \left| \hat{\mathcal{H}} \right| \Psi^{(0)}_{ij,rs} \right\rangle = \sum_{abc}^{act} \underbrace{\left\langle \Psi^{(0)}_{m} \left| E_{ca}E_{br'}\hat{\mathcal{H}}E_{ri}E_{sj} \right| \Psi^{(0)}_{m} \right\rangle}_{\mathrm{val1}} A * c_{a\mu} + \sum_{abc}^{act} \underbrace{\left\langle \Psi^{(0)}_{m} \left| E_{ca}E_{br'}\hat{\mathcal{H}}E_{si}E_{rj} \right| \Psi^{(0)}_{m} \right\rangle}_{\mathrm{val2}} B * c_{a\mu} \tag{B.25}$$

B.0.20 V(1)V(1) Class

The third order contribution for the $V(1)V(1)$ class is

$$E^{(3)} = \sum_{r,r'}^{virt} \sum_{ij,i'j'}^{core} \sum_{\mu,\mu'} C^{(1)(1)}_{i'j'r'\mu'} C^{(1)(1)}_{ijr\mu} \left\langle \Psi^{(1)}_{i'j'r'\mu'} \left| \hat{\mathcal{H}} - \hat{\mathcal{H}}_0 \right| \Psi^{(1)}_{ijr\mu} \right\rangle \tag{B.26}$$

For the diagonal case the contribution of $\hat{\mathcal{H}}_0$ is

$$E^{(3)} = \epsilon_\mu + \epsilon_r - \epsilon_i - \epsilon_j \tag{B.27}$$

For the $S^{(1)}_{ijr}$ subspace the perturbers are expressed as

$$\Psi^{(11)}_{rji,\mu} = \frac{1}{\sqrt{2}} \sum_{a}^{act} (E_{rj}E_{ai} + E_{ri}E_{aj}) \Psi^{(0)}_{m} c_{a,\mu} \tag{B.28}$$

$$\Psi^{'(11)}_{rji,\mu} = \frac{1}{\sqrt{6}} \sum_{a}^{act} (E_{rj}E_{ai} - E_{ri}E_{aj}) \Psi^{(0)}_{m} c_{a,\mu}. \tag{B.29}$$

and, for the case $i = j$, as

$$\Psi^{(1)}_{rii\mu} = \sum_{a}^{act} E_{ri}E_{ai} \Psi^{(0)}_{m} c_{a,\mu} \tag{B.30}$$

All the possible matrix elements have to be considered.

$$\begin{aligned}
\left\langle \Psi^{(1)}_{r'i'j'\mu'} \middle| \hat{\mathcal{H}} \middle| \Psi^{(1)}_{rij\mu} \right\rangle = & \frac{1}{2} \sum_{aa'}^{act} c_{a'\mu'} c_{a\mu} \underbrace{\left\langle \Psi^{(0)}_{m} \middle| E_{i'a'}E_{j'r'i} \hat{\mathcal{H}} E_{rj}E_{ai} \middle| \Psi^{(0)}_{m} \right\rangle}_{\text{val1}} \\
& + \frac{1}{2} \sum_{aa'}^{act} c_{a'\mu'} c_{a\mu} \underbrace{\left\langle \Psi^{(0)}_{m} \middle| E_{i'a'}E_{j'r'} \hat{\mathcal{H}} E_{ri}E_{aj} \middle| \Psi^{(0)}_{m} \right\rangle}_{\text{val2}} \\
& + \frac{1}{2} \sum_{aa'}^{act} c_{a'\mu'} c_{a\mu} \underbrace{\left\langle \Psi^{(0)}_{m} \middle| E_{j'a'}E_{i'r'} \hat{\mathcal{H}} E_{rj}E_{ai} \middle| \Psi^{(0)}_{m} \right\rangle}_{\text{val3}} \\
& + \frac{1}{2} \sum_{aa'}^{act} c_{a'\mu'} c_{a\mu} \underbrace{\left\langle \Psi^{(0)}_{m} \middle| E_{j'a'}E_{i'r'} \hat{\mathcal{H}} E_{ri}E_{aj} \middle| \Psi^{(0)}_{m} \right\rangle}_{\text{val4}}
\end{aligned} \tag{B.31}$$

$$\begin{aligned}
\left\langle \Psi^{'(1)}_{r'i'j'\mu'} \middle| \hat{\mathcal{H}} \middle| \Psi^{'(1)}_{rij\mu} \right\rangle = & \frac{1}{6} \sum_{aa'}^{act} c_{a'\mu'} c_{a\mu} \underbrace{\left\langle \Psi^{(0)}_{m} \middle| E_{i'a'}E_{j'r'i} \hat{\mathcal{H}} E_{rj}E_{ai} \middle| \Psi^{(0)}_{m} \right\rangle}_{\text{val1}} \\
& - \frac{1}{6} \sum_{aa'}^{act} c_{a'\mu'} c_{a\mu} \underbrace{\left\langle \Psi^{(0)}_{m} \middle| E_{i'a'}E_{j'r'} \hat{\mathcal{H}} E_{ri}E_{aj} \middle| \Psi^{(0)}_{m} \right\rangle}_{\text{val2}} \\
& - \frac{1}{6} \sum_{aa'}^{act} c_{a'\mu'} c_{a\mu} \underbrace{\left\langle \Psi^{(0)}_{m} \middle| E_{j'a'}E_{i'r'} \hat{\mathcal{H}} E_{rj}E_{ai} \middle| \Psi^{(0)}_{m} \right\rangle}_{\text{val3}} \\
& + \frac{1}{6} \sum_{aa'}^{act} c_{a'\mu'} c_{a\mu} \underbrace{\left\langle \Psi^{(0)}_{m} \middle| E_{j'a'}E_{i'r'} \hat{\mathcal{H}} E_{ri}E_{aj} \middle| \Psi^{(0)}_{m} \right\rangle}_{\text{val4}}
\end{aligned} \tag{B.32}$$

$$\begin{aligned}\left\langle \Psi^{(1)}_{r'i'j'\mu'} \middle| \hat{\mathcal{H}} \middle| \Psi'^{(1)}_{rij\mu} \right\rangle = &\frac{1}{2\sqrt{3}} \sum_{aa'}^{act} c_{a'\mu'} c_{a\mu} \underbrace{\left\langle \Psi^{(0)}_m \middle| E_{i'a'} E_{j'r'i} \hat{\mathcal{H}} E_{rj} E_{ai} \middle| \Psi^{(0)}_m \right\rangle}_{\mathrm{val1}} \\ &- \frac{1}{2\sqrt{3}} \sum_{aa'}^{act} c_{a'\mu'} c_{a\mu} \underbrace{\left\langle \Psi^{(0)}_m \middle| E_{i'a'} E_{j'r'} \hat{\mathcal{H}} E_{ri} E_{aj} \middle| \Psi^{(0)}_m \right\rangle}_{\mathrm{val2}} \\ &+ \frac{1}{2\sqrt{3}} \sum_{aa'}^{act} c_{a'\mu'} c_{a\mu} \underbrace{\left\langle \Psi^{(0)}_m \middle| E_{j'a'} E_{i'r'} \hat{\mathcal{H}} E_{rj} E_{ai} \middle| \Psi^{(0)}_m \right\rangle}_{\mathrm{val3}} \\ &- \frac{1}{2\sqrt{3}} \sum_{aa'}^{act} c_{a'\mu'} c_{a\mu} \underbrace{\left\langle \Psi^{(0)}_m \middle| E_{j'a'} E_{i'r'} \hat{\mathcal{H}} E_{ri} E_{aj} \middle| \Psi^{(0)}_m \right\rangle}_{\mathrm{val4}}\end{aligned} \tag{B.33}$$

$$\begin{aligned}\left\langle \Psi'^{(1)}_{r'i'j'\mu'} \middle| \hat{\mathcal{H}} \middle| \Psi^{(1)}_{rij\mu} \right\rangle = &\frac{1}{2\sqrt{3}} \sum_{aa'}^{act} c_{a'\mu'} c_{a\mu} \underbrace{\left\langle \Psi^{(0)}_m \middle| E_{i'a'} E_{j'r'i} \hat{\mathcal{H}} E_{rj} E_{ai} \middle| \Psi^{(0)}_m \right\rangle}_{\mathrm{val1}} \\ &+ \frac{1}{2\sqrt{3}} \sum_{aa'}^{act} c_{a'\mu'} c_{a\mu} \underbrace{\left\langle \Psi^{(0)}_m \middle| E_{i'a'} E_{j'r'} \hat{\mathcal{H}} E_{ri} E_{aj} \middle| \Psi^{(0)}_m \right\rangle}_{\mathrm{val2}} \\ &- \frac{1}{2\sqrt{3}} \sum_{aa'}^{act} c_{a'\mu'} c_{a\mu} \underbrace{\left\langle \Psi^{(0)}_m \middle| E_{j'a'} E_{i'r'} \hat{\mathcal{H}} E_{rj} E_{ai} \middle| \Psi^{(0)}_m \right\rangle}_{\mathrm{val3}} \\ &- \frac{1}{2\sqrt{3}} \sum_{aa'}^{act} c_{a'\mu'} c_{a\mu} \underbrace{\left\langle \Psi^{(0)}_m \middle| E_{j'a'} E_{i'r'} \hat{\mathcal{H}} E_{ri} E_{aj} \middle| \Psi^{(0)}_m \right\rangle}_{\mathrm{val4}}\end{aligned} \tag{B.34}$$

Furthermore, other five cases have to be considered:

- $i = j \quad \text{and} \quad i' = j'$

$$\left\langle \Psi^{(1)}_{r'i'i'\mu'} \middle| \hat{\mathcal{H}} \middle| \Psi^{(1)}_{rii\mu} \right\rangle = \sum_{aa'}^{act} \underbrace{\left\langle \Psi^{(0)}_m \middle| E_{i'a'} E_{i'r'} \hat{\mathcal{H}} E_{ri} E_{ai} \middle| \Psi^{(0)}_m \right\rangle}_{\mathrm{val1}} c_{a'\mu'} c_{a\mu} \tag{B.35}$$

- $i = j \quad \text{and} \quad i' \neq j'$

$$\begin{aligned}\left\langle \Psi'^{(1)}_{r'i'j'\mu'} \middle| \hat{\mathcal{H}} \middle| \Psi^{(1)}_{rii\mu} \right\rangle = &\frac{1}{\sqrt{6}} \sum_{aa'}^{act} c_{a'\mu'} c_{a\mu} \underbrace{\left\langle \Psi^{(0)}_m \middle| E_{i'a'} E_{j'r'} \hat{\mathcal{H}} E_{ri} E_{ai} \middle| \Psi^{(0)}_m \right\rangle}_{\mathrm{val1}} \\ &- \frac{1}{\sqrt{6}} \sum_{aa'}^{act} c_{a'\mu'} c_{a\mu} \underbrace{\left\langle \Psi^{(0)}_m \middle| E_{j'a'} E_{i'r'} \hat{\mathcal{H}} E_{ri} E_{ai} \middle| \Psi^{(0)}_m \right\rangle}_{\mathrm{val3}}\end{aligned} \tag{B.36}$$

$$\begin{aligned}\left\langle \Psi^{(1)}_{r'i'j'\mu'} \middle| \hat{\mathcal{H}} \middle| \Psi^{(1)}_{riia} \right\rangle = \frac{1}{\sqrt{2}} \sum_{aa'}^{act} c_{a'\mu'} c_{a\mu} \underbrace{\left\langle \Psi^{(0)}_m \middle| E_{i'a'} E_{j'r'} \hat{\mathcal{H}} E_{ri} E_{ai} \middle| \Psi^{(0)}_m \right\rangle}_{val1} \\ + \frac{1}{\sqrt{2}} \sum_{aa'}^{act} c_{a'\mu'} c_{a\mu} \underbrace{\left\langle \Psi^{(0)}_m \middle| E_{j'a'} E_{i'r'} \hat{\mathcal{H}} E_{ri} E_{ai} \middle| \Psi^{(0)}_m \right\rangle}_{val3}\end{aligned} \tag{B.37}$$

- $i \neq j \quad \& \quad i' = j'$

$$\begin{aligned}\left\langle \Psi^{(1)}_{r'i'i'\mu'} \middle| \hat{\mathcal{H}} \middle| \Psi'^{(1)}_{rij\mu} \right\rangle = \frac{1}{\sqrt{6}} \sum_{aa'}^{act} c_{a'\mu'} c_{a\mu} \underbrace{\left\langle \Psi^{(0)}_m \middle| E_{i'a'} E_{i'r'} \hat{\mathcal{H}} E_{rj} E_{ai} \middle| \Psi^{(0)}_m \right\rangle}_{val1} \\ - \frac{1}{\sqrt{6}} \sum_{aa'}^{act} c_{a'\mu'} c_{a\mu} \underbrace{\left\langle \Psi^{(0)}_m \middle| E_{i'a'} E_{i'r'} \hat{\mathcal{H}} E_{ri} E_{aj} \middle| \Psi^{(0)}_m \right\rangle}_{val2}\end{aligned} \tag{B.38}$$

$$\begin{aligned}\left\langle \Psi^{(1)}_{r'i'i'\mu'} \middle| \hat{\mathcal{H}} \middle| \Psi^{(1)}_{rij\mu} \right\rangle = \frac{1}{\sqrt{2}} \sum_{aa'}^{act} c_{a'\mu'} c_{a\mu} \underbrace{\left\langle \Psi^{(0)}_m \middle| E_{i'a'} E_{i'r'} \hat{\mathcal{H}} E_{rj} E_{ai} \middle| \Psi^{(0)}_m \right\rangle}_{val1} \\ + \frac{1}{\sqrt{2}} \sum_{aa'}^{act} c_{a'\mu'} c_{a\mu} \underbrace{\left\langle \Psi^{(0)}_m \middle| E_{i'a'} E_{i'r'} \hat{\mathcal{H}} E_{ri} E_{aj} \middle| \Psi^{(0)}_m \right\rangle}_{val2}\end{aligned} \tag{B.39}$$

B.0.21 V(1)V(−1) Class

For the $S^{(-1)}_{ris}$ subspace the perturbers have the following form

$$\Psi^{(-1)}_{ris,\mu} = \frac{1}{\sqrt{2}} \sum_{a}^{act} (E_{ri}E_{sa} + E_{si}E_{ra}) \Psi^{(0)}_m c_{2_{a,\mu}} \tag{B.40}$$

$$\Psi'^{(-1)}_{ris,\mu} = \frac{1}{\sqrt{6}} \sum_{a}^{act} (E_{ri}E_{sa} - E_{si}E_{ra}) \Psi^{(0)}_m c_{2_{a,\mu}}. \tag{B.41}$$

and, for the case $r = s$, they are expressed as

$$\Psi^{(1)}_{rir\mu} = \sum_{a}^{act} E_{ri}E_{ra} \Psi^{(0)}_m c_{2_{a,\mu}} \tag{B.42}$$

As in the previous case, all the possibilities must be examined:

$$\begin{aligned}
\left\langle \Psi^{(-1)}_{r'i's'\mu'} \left| \hat{\mathcal{H}} \right| \Psi^{(1)}_{rij\mu} \right\rangle = \frac{1}{2} \sum_{aa'}^{act} c_{2_{a'\mu'}} c_{a\mu} \underbrace{\left\langle \Psi^{(0)}_m \left| E_{a's'} E_{i'r'} \hat{\mathcal{H}} E_{rj} E_{ai} \right| \Psi^{(0)}_m \right\rangle}_{\mathrm{val1}} \\
+ \frac{1}{2} \sum_{aa'}^{act} c_{2_{a'\mu'}} c_{a\mu} \underbrace{\left\langle \Psi^{(0)}_m \left| E_{a's'} E_{i'r'} \hat{\mathcal{H}} E_{ri} E_{aj} \right| \Psi^{(0)}_m \right\rangle}_{\mathrm{val2}} \\
+ \frac{1}{2} \sum_{aa'}^{act} c_{2_{a'\mu'}} c_{a\mu} \underbrace{\left\langle \Psi^{(0)}_m \left| E_{a'r'} E_{i's'} \hat{\mathcal{H}} E_{rj} E_{ai} \right| \Psi^{(0)}_m \right\rangle}_{\mathrm{val3}} \\
+ \frac{1}{2} \sum_{aa'}^{act} c_{2_{a'\mu'}} c_{a\mu} \underbrace{\left\langle \Psi^{(0)}_m \left| E_{a'r'} E_{i's'} \hat{\mathcal{H}} E_{ri} E_{aj} \right| \Psi^{(0)}_m \right\rangle}_{\mathrm{val4}}
\end{aligned} \tag{B.43}$$

$$\begin{aligned}
\left\langle \Psi'^{(-1)}_{r'i's'\mu'} \left| \hat{\mathcal{H}} \right| \Psi'^{(1)}_{rij\mu} \right\rangle = \frac{1}{6} \sum_{aa'}^{act} c_{2_{a'\mu'}} c_{a\mu} \underbrace{\left\langle \Psi^{(0)}_m \left| E_{a's'} E_{i'r'} \hat{\mathcal{H}} E_{rj} E_{ai} \right| \Psi^{(0)}_m \right\rangle}_{\mathrm{val1}} \\
- \frac{1}{6} \sum_{aa'}^{act} c_{2_{a'\mu'}} c_{a\mu} \underbrace{\left\langle \Psi^{(0)}_m \left| E_{a's'} E_{i'r'} \hat{\mathcal{H}} E_{ri} E_{aj} \right| \Psi^{(0)}_m \right\rangle}_{\mathrm{val2}} \\
- \frac{1}{6} \sum_{aa'}^{act} c_{2_{a'\mu'}} c_{a\mu} \underbrace{\left\langle \Psi^{(0)}_m \left| E_{a'r'} E_{i's'} \hat{\mathcal{H}} E_{rj} E_{ai} \right| \Psi^{(0)}_m \right\rangle}_{\mathrm{val3}} \\
+ \frac{1}{6} \sum_{aa'}^{act} c_{2_{a'\mu'}} c_{a\mu} \underbrace{\left\langle \Psi^{(0)}_m \left| E_{a'r'} E_{i's'} \hat{\mathcal{H}} E_{ri} E_{aj} \right| \Psi^{(0)}_m \right\rangle}_{\mathrm{val4}}
\end{aligned} \tag{B.44}$$

$$\begin{aligned}
\left\langle \Psi^{(-1)}_{r'i's'\mu'} \left| \hat{\mathcal{H}} \right| \Psi'^{(1)}_{rij\mu} \right\rangle = \frac{1}{12} \sum_{aa'}^{act} c_{2_{a'\mu'}} c_{a\mu} \underbrace{\left\langle \Psi^{(0)}_m \left| E_{a's'} E_{i'r'} \hat{\mathcal{H}} E_{rj} E_{ai} \right| \Psi^{(0)}_m \right\rangle}_{\mathrm{val1}} \\
- \frac{1}{12} \sum_{aa'}^{act} c_{2_{a'\mu'}} c_{a\mu} \underbrace{\left\langle \Psi^{(0)}_m \left| E_{a's'} E_{i'r'} \hat{\mathcal{H}} E_{ri} E_{aj} \right| \Psi^{(0)}_m \right\rangle}_{\mathrm{val2}} \\
+ \frac{1}{12} \sum_{aa'}^{act} c_{2_{a'\mu'}} c_{a\mu} \underbrace{\left\langle \Psi^{(0)}_m \left| E_{a'r'} E_{i's'} \hat{\mathcal{H}} E_{rj} E_{ai} \right| \Psi^{(0)}_m \right\rangle}_{\mathrm{val3}} \\
- \frac{1}{12} \sum_{aa'}^{act} c_{2_{a'\mu'}} c_{a\mu} \underbrace{\left\langle \Psi^{(0)}_m \left| E_{a'r'} E_{i's'} \hat{\mathcal{H}} E_{ri} E_{aj} \right| \Psi^{(0)}_m \right\rangle}_{\mathrm{val4}}
\end{aligned} \tag{B.45}$$

$$\begin{aligned}\left\langle \Psi^{\prime(-1)}_{r'i's'\mu'} \middle| \hat{\mathcal{H}} \middle| \Psi^{(1)}_{rij\mu} \right\rangle = &\frac{1}{12}\sum_{aa'}^{act} c_{2_{a'\mu'}} c_{a\mu} \underbrace{\left\langle \Psi^{(0)}_m \middle| E_{a's'}E_{i'r'}\hat{\mathcal{H}}E_{rj}E_{ai} \middle| \Psi^{(0)}_m \right\rangle}_{\text{val1}} \\ &+ \frac{1}{12}\sum_{aa'}^{act} c_{2_{a'\mu'}} c_{a\mu} \underbrace{\left\langle \Psi^{(0)}_m \middle| E_{a's'}E_{i'r'}\hat{\mathcal{H}}E_{ri}E_{aj} \middle| \Psi^{(0)}_m \right\rangle}_{\text{val2}} \\ &- \frac{1}{12}\sum_{aa'}^{act} c_{2_{a'\mu'}} c_{a\mu} \underbrace{\left\langle \Psi^{(0)}_m \middle| E_{a'r'}E_{i's'}\hat{\mathcal{H}}E_{rj}E_{ai} \middle| \Psi^{(0)}_m \right\rangle}_{\text{val3}} \\ &- \frac{1}{12}\sum_{aa'}^{act} c_{2_{a'\mu'}} c_{a\mu} \underbrace{\left\langle \Psi^{(0)}_m \middle| E_{a'r'}E_{i's'}\hat{\mathcal{H}}E_{ri}E_{aj} \middle| \Psi^{(0)}_m \right\rangle}_{\text{val4}}\end{aligned} \tag{B.46}$$

Then, analogously, we have

- $i = j \quad \text{and} \quad r' = s'$

$$\left\langle \Psi^{(-1)}_{r'i'r'\mu'} \middle| \hat{\mathcal{H}} \middle| \Psi^{(1)}_{rii\mu} \right\rangle = \sum_{aa'}^{act} \underbrace{\left\langle \Psi^{(0)}_m \middle| E_{a'r'}E_{i'r'}\hat{\mathcal{H}}E_{ri}E_{ai} \middle| \Psi^{(0)}_m \right\rangle}_{\text{val1}} c_{2_{a'\mu'}} c_{a\mu} \tag{B.47}$$

- $i = j \quad \text{and} \quad r' \neq s'$

$$\begin{aligned}\left\langle \Psi^{\prime(1)}_{r'i's'\mu'} \middle| \hat{\mathcal{H}} \middle| \Psi^{(1)}_{rii\mu} \right\rangle = &\frac{1}{\sqrt{6}}\sum_{aa'}^{act} c_{2_{a'\mu'}} c_{a\mu} \underbrace{\left\langle \Psi^{(0)}_m \middle| E_{a's'}E_{i'r'}\hat{\mathcal{H}}E_{ri}E_{ai} \middle| \Psi^{(0)}_m \right\rangle}_{\text{val1}} \\ &- \frac{1}{\sqrt{6}}\sum_{aa'}^{act} c_{2_{a'\mu'}} c_{a\mu} \underbrace{\left\langle \Psi^{(0)}_m \middle| E_{a'r'}E_{i's'}\hat{\mathcal{H}}E_{ri}E_{ai} \middle| \Psi^{(0)}_m \right\rangle}_{\text{val3}}\end{aligned} \tag{B.48}$$

$$\begin{aligned}\left\langle \Psi^{(-1)}_{r'i's'\mu'} \middle| \hat{\mathcal{H}} \middle| \Psi^{(1)}_{rii\mu} \right\rangle = &\frac{1}{\sqrt{2}}\sum_{aa'}^{act} c_{2_{a'\mu'}} c_{a\mu} \underbrace{\left\langle \Psi^{(0)}_m \middle| E_{a's'}E_{i'r'}\hat{\mathcal{H}}E_{ri}E_{ai} \middle| \Psi^{(0)}_m \right\rangle}_{\text{val1}} \\ &+ \frac{1}{\sqrt{2}}\sum_{aa'}^{act} c_{2_{a'\mu'}} c_{a\mu} \underbrace{\left\langle \Psi^{(0)}_m \middle| E_{a'r'}E_{i's'}\hat{\mathcal{H}}E_{ri}E_{ai} \middle| \Psi^{(0)}_m \right\rangle}_{\text{val3}}\end{aligned} \tag{B.49}$$

- $i \neq j \quad \text{and} \quad r' = s'$

$$\left\langle \Psi^{(1)}_{r'i'r'\mu'} \middle| \hat{\mathcal{H}} \middle| \Psi'^{(1)}_{rij\mu} \right\rangle = \frac{1}{\sqrt{6}} \sum_{aa'}^{act} c_{2_{a'\mu'}} c_{a\mu} \underbrace{\left\langle \Psi^{(0)}_m \middle| E_{a'r'} E_{i'r'} \hat{\mathcal{H}} E_{rj} E_{ai} \middle| \Psi^{(0)}_m \right\rangle}_{\mathrm{val1}} - \frac{1}{\sqrt{6}} \sum_{aa'}^{act} c_{2_{a'\mu'}} c_{a\mu} \underbrace{\left\langle \Psi^{(0)}_m \middle| E_{a'r'} E_{i'r'} \hat{\mathcal{H}} E_{ri} E_{aj} \middle| \Psi^{(0)}_m \right\rangle}_{\mathrm{val2}} \tag{B.50}$$

$$\left\langle \Psi^{(1)}_{r'i'r'\mu'} \middle| \hat{\mathcal{H}} \middle| \Psi^{(1)}_{rij\mu} \right\rangle = \frac{1}{\sqrt{2}} \sum_{aa'}^{act} c_{2_{a'\mu'}} c_{a\mu} \underbrace{\left\langle \Psi^{(0)}_m \middle| E_{a'r'} E_{i'r'} \hat{\mathcal{H}} E_{rj} E_{ai} \middle| \Psi^{(0)}_m \right\rangle}_{\mathrm{val1}} + \frac{1}{\sqrt{2}} \sum_{aa'}^{act} c_{2_{a'\mu'}} c_{a\mu} \underbrace{\left\langle \Psi^{(0)}_m \middle| E_{a'r'} E_{i'r'} \hat{\mathcal{H}} E_{ri} E_{aj} \middle| \Psi^{(0)}_m \right\rangle}_{\mathrm{val2}} \tag{B.51}$$

B.0.22 V(1)V(2) Class

If $i \neq j$, for the $S^{(2)}_{ij}$ space the perturbers are given by:

$$\Psi^{(2)}_{ij\mu} = \sum_{a,b}^{act} E_{bi} E_{aj} \Psi^{(0)}_m c_{2_{ab,\mu}} \tag{B.52}$$

whereas, for the case $i = j$ they are

$$\Psi^{(2)}_{ii\mu} = \sum_{a \geq b}^{act} E_{bi} E_{aj} \Psi^{(0)}_m c'_{2_{ab,\mu}} \tag{B.53}$$

The matrix elements that have to be computed are:

$$\left\langle \Psi^{(2)}_{i'j'\mu'} \middle| \hat{\mathcal{H}} \middle| \Psi^{(1)}_{rij\mu} \right\rangle = \frac{1}{\sqrt{2}} \sum_{aa'b'}^{act} c_{2_{a'b'\mu'}} c_{a\mu} \underbrace{\left\langle \Psi^{(0)}_m \middle| E_{j'a'} E_{i'b'} \hat{\mathcal{H}} E_{rj} E_{ai} \middle| \Psi^{(0)}_m \right\rangle}_{\mathrm{val1}} + \frac{1}{\sqrt{2}} \sum_{aa'b'}^{act} c_{2_{a'b'\mu'}} c_{a\mu} \underbrace{\left\langle \Psi^{(0)}_m \middle| E_{j'a'} E_{i'b'} \hat{\mathcal{H}} E_{ri} E_{aj} \middle| \Psi^{(0)}_m \right\rangle}_{\mathrm{val2}} \tag{B.54}$$

$$\left\langle \Psi^{(2)}_{i'j'\mu'} \middle| \hat{\mathcal{H}} \middle| \Psi'^{(1)}_{rij\mu} \right\rangle = \frac{1}{\sqrt{6}} \sum_{aa'b'}^{act} c_{2_{a'b'\mu'}} c_{a\mu} \underbrace{\left\langle \Psi^{(0)}_m \middle| E_{j'a'} E_{i'b'} \hat{\mathcal{H}} E_{rj} E_{ai} \middle| \Psi^{(0)}_m \right\rangle}_{\mathrm{val1}} - \frac{1}{\sqrt{6}} \sum_{aa'b'}^{act} c_{2_{a'b'\mu'}} c_{a\mu} \underbrace{\left\langle \Psi^{(0)}_m \middle| E_{j'a'} E_{i'b'} \hat{\mathcal{H}} E_{ri} E_{aj} \middle| \Psi^{(0)}_m \right\rangle}_{\mathrm{val2}} \tag{B.55}$$

$$\begin{aligned}\left\langle \Psi^{(2)}_{i'i'\mu'} \middle| \hat{\mathcal{H}} \middle| \Psi^{(1)}_{rij\mu} \right\rangle = &\frac{1}{\sqrt{2}} \sum_{a'\geq b'}^{act} \sum_{a}^{act} c'_{2_{a'b'\mu'}} c_{a\mu} \underbrace{\left\langle \Psi^{(0)}_m \middle| E_{j'a'} E_{i'b'} \hat{\mathcal{H}} E_{rj} E_{ai} \middle| \Psi^{(0)}_m \right\rangle}_{\text{val1}} \\ &+ \frac{1}{\sqrt{2}} \sum_{a'\geq b'}^{act} \sum_{a}^{act} c'_{2_{a'b'\mu'}} c_{a\mu} \underbrace{\left\langle \Psi^{(0)}_m \middle| E_{j'a'} E_{i'b'} \hat{\mathcal{H}} E_{ri} E_{aj} \middle| \Psi^{(0)}_m \right\rangle}_{\text{val2}}\end{aligned} \tag{B.56}$$

$$\begin{aligned}\left\langle \Psi^{(2)}_{i'i'\mu'} \middle| \hat{\mathcal{H}} \middle| \Psi'^{(1)}_{rij\mu} \right\rangle = &\frac{1}{\sqrt{6}} \sum_{a'\geq b'}^{act} \sum_{a}^{act} c'_{2_{a'b'\mu'}} c_{a\mu} \underbrace{\left\langle \Psi^{(0)}_m \middle| E_{j'a'} E_{i'b'} \hat{\mathcal{H}} E_{rj} E_{ai} \middle| \Psi^{(0)}_m \right\rangle}_{\text{val1}} \\ &- \frac{1}{\sqrt{6}} \sum_{a'\geq b'}^{act} \sum_{a}^{act} c'_{2_{a'b'\mu'}} c_{a\mu} \underbrace{\left\langle \Psi^{(0)}_m \middle| E_{j'a'} E_{i'b'} \hat{\mathcal{H}} E_{ri} E_{aj} \middle| \Psi^{(0)}_m \right\rangle}_{\text{val2}}\end{aligned} \tag{B.57}$$

B.0.23 V(1)V(0′) Class

We recall that the perturbation functions belonging to the $\bar{S}^{(0)}_{ir}$ space can be written as

$$\Psi^{(2)}_{ir\mu} = \left(\sum_{a,b}^{act} E_{ri} E_{ab} c_{2_{ab,\mu}} + \sum_{a,b}^{act} E_{ai} E_{rb} c'_{2_{ab,\mu}} \right) \Psi^{(0)}_m \tag{B.58}$$

therefore, the interaction elements are

$$\begin{aligned}\left\langle \Psi^{(0)}_{i'r'\mu'} \middle| \hat{\mathcal{H}} \middle| \Psi^{(1)}_{rij\mu} \right\rangle = &\frac{1}{\sqrt{2}} \sum_{a'b'a}^{act} c_{2_{a'b'\mu'}} c_{a\mu} \underbrace{\left\langle \Psi^{(0)}_m \middle| E_{b'a'} E_{i'r'} \hat{\mathcal{H}} E_{rj} E_{ai} \middle| \Psi^{(0)}_m \right\rangle}_{\text{val1}} \\ &+ \frac{1}{\sqrt{2}} \sum_{a'b'a}^{act} c_{2_{a'\mu'}} c_{a\mu} \underbrace{\left\langle \Psi^{(0)}_m \middle| E_{b'a'} E_{i'r'} \hat{\mathcal{H}} E_{ri} E_{aj} \middle| \Psi^{(0)}_m \right\rangle}_{\text{val2}} \\ &+ \frac{1}{\sqrt{2}} \sum_{a'b'a}^{act} c'_{2_{a'\mu'}} c_{a\mu} \underbrace{\left\langle \Psi^{(0)}_m \middle| E_{b'r'} E_{i'a'} \hat{\mathcal{H}} E_{rj} E_{ai} \middle| \Psi^{(0)}_m \right\rangle}_{\text{val3}} \\ &+ \frac{1}{\sqrt{2}} \sum_{a'b'a}^{act} c'_{2_{a'\mu'}} c_{a\mu} \underbrace{\left\langle \Psi^{(0)}_m \middle| E_{b'r'} E_{i'a'} \hat{\mathcal{H}} E_{ri} E_{aj} \middle| \Psi^{(0)}_m \right\rangle}_{\text{val4}}\end{aligned} \tag{B.59}$$

$$\begin{aligned}\left\langle \Psi^{(0)}_{i'r'\mu'} \middle| \hat{\mathcal{H}} \middle| \Psi'^{(1)}_{rij\mu} \right\rangle = &\frac{1}{\sqrt{6}} \sum_{a'b'a}^{act} c_{2_{a'b'\mu'}} c_{a\mu} \underbrace{\left\langle \Psi^{(0)}_m \middle| E_{b'a'} E_{i'r'} \hat{\mathcal{H}} E_{rj} E_{ai} \middle| \Psi^{(0)}_m \right\rangle}_{\text{val1}} \\ &- \frac{1}{\sqrt{6}} \sum_{a'b'a}^{act} c_{2_{a'\mu'}} c_{a\mu} \underbrace{\left\langle \Psi^{(0)}_m \middle| E_{b'a'} E_{i'r'} \hat{\mathcal{H}} E_{ri} E_{aj} \middle| \Psi^{(0)}_m \right\rangle}_{\text{val2}} \\ &+ \frac{1}{\sqrt{6}} \sum_{a'b'a}^{act} c'_{2_{a'\mu'}} c_{a\mu} \underbrace{\left\langle \Psi^{(0)}_m \middle| E_{b'r'} E_{i'a'} \hat{\mathcal{H}} E_{rj} E_{ai} \middle| \Psi^{(0)}_m \right\rangle}_{\text{val3}} \\ &- \frac{1}{\sqrt{6}} \sum_{a'b'a}^{act} c'_{2_{a'\mu'}} c_{a\mu} \underbrace{\left\langle \Psi^{(0)}_m \middle| E_{b'r'} E_{i'a'} \hat{\mathcal{H}} E_{ri} E_{aj} \middle| \Psi^{(0)}_m \right\rangle}_{\text{val4}}\end{aligned} \tag{B.60}$$

Finally, one has to consider the case $i = j$, in which the perturbers of the $\bar{S}^{(1)}_{iir}$ have the form

$$\Psi^{(1)}_{riii\mu} = \sum_{a}^{act} E_{ri} E_{ai} c_{a,\mu} \Psi^{(0)}_m \tag{B.61}$$

The interaction becomes:

$$\begin{aligned}\left\langle \Psi^{(0)}_{i'r'\mu'} \middle| \hat{\mathcal{H}} \middle| \Psi^{(1)}_{riii\mu} \right\rangle = &\sum_{a'b'a}^{act} c_{2_{a'b'\mu'}} c_{a\mu} \underbrace{\left\langle \Psi^{(0)}_m \middle| E_{b'a'} E_{i'r'} \hat{\mathcal{H}} E_{ri} E_{ai} \middle| \Psi^{(0)}_m \right\rangle}_{\text{val1}} \\ &+ \sum_{a'b'a}^{act} c'_{2_{a'\mu'}} c_{a\mu} \underbrace{\left\langle \Psi^{(0)}_m \middle| E_{b'r'} E_{i'a'} \hat{\mathcal{H}} E_{ri} E_{ai} \middle| \Psi^{(0)}_m \right\rangle}_{\text{val3}}\end{aligned} \tag{B.62}$$

B.0.24 $\mathbf{V(1)V(-1')}$ Class

The perturbers of the $\bar{S}^{(-1)}_{r}$ space are

$$\Psi^{(-1)}_{r\mu} = \sum_{a,b,c}^{act} E_{rb} E_{ac} c_{abc,\mu} \Psi^{(0)}_m \tag{B.63}$$

Thus, the matrix elements have the form

$$\begin{aligned}\left\langle \Psi^{(-1)}_{r'\mu'} \middle| \hat{\mathcal{H}} \middle| \Psi^{(1)}_{rij\mu} \right\rangle = &\frac{1}{\sqrt{2}} \sum_{a'b'c'a}^{act} c_{2_{a'b'c'\mu'}} c_{a\mu} \underbrace{\left\langle \Psi^{(0)}_m \middle| E_{c'a'} E_{b'r'} \hat{\mathcal{H}} E_{rj} E_{ai} \middle| \Psi^{(0)}_m \right\rangle}_{\text{val1}} \\ &+ \frac{1}{\sqrt{2}} \sum_{a'b'c'a}^{act} c_{2_{a'b'c'\mu'}} c_{a\mu} \underbrace{\left\langle \Psi^{(0)}_m \middle| E_{c'a'} E_{b'r'} \hat{\mathcal{H}} E_{ri} E_{aj} \middle| \Psi^{(0)}_m \right\rangle}_{\text{val2}}\end{aligned} \tag{B.64}$$

$$\begin{aligned}\left\langle \Psi^{(-1)}_{r'\mu'} \middle| \hat{\mathcal{H}} \middle| \Psi'^{(1)}_{rij\mu} \right\rangle = &\frac{1}{\sqrt{6}} \sum_{a'b'c'a}^{act} c_{2_{a'b'c'\mu'}} c_{a\mu} \underbrace{\left\langle \Psi^{(0)}_m \middle| E_{c'a'} E_{b'r'} \hat{\mathcal{H}} E_{rj} E_{ai} \middle| \Psi^{(0)}_m \right\rangle}_{\mathrm{val1}} \\ &- \frac{1}{\sqrt{6}} \sum_{a'b'c'a}^{act} c_{2_{a'b'c'\mu'}} c_{a\mu} \underbrace{\left\langle \Psi^{(0)}_m \middle| E_{c'a'} E_{b'r'} \hat{\mathcal{H}} E_{ri} E_{aj} \middle| \Psi^{(0)}_m \right\rangle}_{\mathrm{val2}}\end{aligned} \tag{B.65}$$

Then, when $i = j$, the interaction simply reduces to

$$\left\langle \Psi^{(-1)}_{r'\mu'} \middle| \hat{\mathcal{H}} \middle| \Psi^{(1)}_{rii\mu} \right\rangle = \sum_{a'b'c'a}^{act} c_{2_{a'b'c'\mu'}} c_{a\mu} \underbrace{\left\langle \Psi^{(0)}_m \middle| E_{c'a'} E_{b'r'} \hat{\mathcal{H}} E_{ri} E_{ai} \middle| \Psi^{(0)}_m \right\rangle}_{\mathrm{val1}} \tag{B.66}$$

B.0.25 V(1)V(1′) Class

The treatment of this class is close to that previously examined. The perturbation functions for the $\bar{S}^{(1)}_i$ are

$$\Psi^{(1)}_{i\mu} = \sum_{a,b,c}^{act} E_{bi} E_{ac} c_{abc,\mu} \Psi^{(0)}_m \tag{B.67}$$

and the interaction elements become

$$\begin{aligned}\left\langle \Psi^{(1)}_{i'\mu'} \middle| \hat{\mathcal{H}} \middle| \Psi^{(1)}_{rij\mu} \right\rangle = &\frac{1}{\sqrt{2}} \sum_{a'b'c'a}^{act} c_{2_{a'b'c'\mu'}} c_{a\mu} \underbrace{\left\langle \Psi^{(0)}_m \middle| E_{c'a'} E_{i'b'} \hat{\mathcal{H}} E_{rj} E_{ai} \middle| \Psi^{(0)}_m \right\rangle}_{\mathrm{val1}} \\ &+ \frac{1}{\sqrt{2}} \sum_{a'b'c'a}^{act} c_{2_{a'b'c'\mu'}} c_{a\mu} \underbrace{\left\langle \Psi^{(0)}_m \middle| E_{c'a'} E_{i'b'} \hat{\mathcal{H}} E_{ri} E_{aj} \middle| \Psi^{(0)}_m \right\rangle}_{\mathrm{val2}}\end{aligned} \tag{B.68}$$

$$\begin{aligned}\left\langle \Psi^{(1)}_{i'\mu'} \middle| \hat{\mathcal{H}} \middle| \Psi'^{(1)}_{rij\mu} \right\rangle = &\frac{1}{\sqrt{6}} \sum_{a'b'c'a}^{act} c_{2_{a'b'c'\mu'}} c_{a\mu} \underbrace{\left\langle \Psi^{(0)}_m \middle| E_{c'a'} E_{i'b'} \hat{\mathcal{H}} E_{rj} E_{ai} \middle| \Psi^{(0)}_m \right\rangle}_{\mathrm{val1}} \\ &- \frac{1}{\sqrt{6}} \sum_{a'b'c'a}^{act} c_{2_{a'b'c'\mu'}} c_{a\mu} \underbrace{\left\langle \Psi^{(0)}_m \middle| E_{c'a'} E_{i'b'} \hat{\mathcal{H}} E_{ri} E_{aj} \middle| \Psi^{(0)}_m \right\rangle}_{\mathrm{val2}}\end{aligned} \tag{B.69}$$

and, finally, for the case $i = j$ one has

$$\left\langle \Psi^{(1)}_{i'\mu'} \middle| \hat{\mathcal{H}} \middle| \Psi^{(1)}_{rii\mu} \right\rangle = \sum_{a'b'c'a}^{act} c_{2_{a'b'c'\mu'}} c_{a\mu} \underbrace{\left\langle \Psi^{(0)}_m \middle| E_{c'a'} E_{i'b'} \hat{\mathcal{H}} E_{ri} E_{ai} \middle| \Psi^{(0)}_m \right\rangle}_{\mathrm{val1}} \tag{B.70}$$

Bibliography

[1] N. Ben-Amor, S. Evangelisti, D. Maynau, and E. Rossi. *Chem. Phys. Lett.*, 288:348, 1998.

[2] E. Rossi, GL. Bendazzoli, S. Evangelisti, and D.Maynau. *Chem. Phys. Lett.*, 310:530, 1999.

[3] P. Jørgensen and J. Simon. *Second-Quantization-Based Methods in Quantum Chemistry*. Academic Press, New York, 1981.

[4] T. Helgaker, P. Jørgensen, and J. Olsen. *Molecular Electronic-Structure Theory*. Wiley, 2000.

[5] Attila Szabo and Neil S. Ostlund. *Modern Quantum Chemistry*. McGraw-Hill, 1989.

[6] L. Brillouin. *Actualités scientifiques et Industrielles*, 71, 1933.

[7] L. Brillouin. *Actualités scientifiques et Industrielles*, 159, 1934.

[8] Koopmans. *T. Physica*, 1:104–113, 1933.

[9] C. Angeli. *J. Chem. Edu.*, 75:1494, 1998.

[10] R. McWeeny. *Proc. R. Soc. Lond.*, A223:63, 1954.

[11] R. McWeeny. *Proc. R. Soc. Lond.*, A233:306, 1954.

[12] R. McWeeny. *Rev. Mod. Phys.*, 32:335, 1960.

[13] P.-O. Löwdin. *Phys. Rev.*, 97:1474, 1955.

[14] B. Levy and G. Berthier. *Int. J. Quant. Chem.*, 2:307, 1968.

[15] B. O. Roos, P. R. Taylor, and P. E. M. Siegbahn. *Chem. Phys.*, 48:157, 1980.

[16] B. Huronand, J.-P. Malrieu, and P. Rancurel. *J. Chem. Phys.*, 58:5745, 1973.

[17] K. Andersson, P. Malmqvist, B. O. Roos, A. J. Sadlej, and K. Wolinski. *J. Phys. Chem.*, 94:5483, 1990.

[18] K. Andersson, P. Malmqvist, and B. O. Roos. *J. Chem. Phys.*, 96:1218, 1992.

[19] K. G. Dyall. *J. Chem. Phys.*, 102:4909, 1995.

[20] C. Angeli, R. Cimiraglia, S. Evangelisti, T. Leininger, and J.-P. Malrieu. *J. Chem. Phys.*, 114:10252–10264, 2001.

[21] C. Angeli, R. Cimiraglia, and J.-P Malrieu. *Chem. Phys. Lett.*, 350:297–305, 2001.

[22] C. Angeli, R. Cimiraglia, and J.-P Malrieu. *J. Chem. Phys.*, 117:9138, 2002.

[23] C. Angeli, S. Borini, M. Cestari, and R. Cimiraglia. *J. Chem. Phys.*, 121:4043, 2004.

[24] C. Angeli, B. Bories, A. Cavallini, and R. Cimiraglia. *J. Chem. Phys.*, 124:054108, 2006.

[25] C. Angeli, M. Pastore, and R. Cimiraglia. *Theor. Chem. Acc.*, 117:743, 2007.

[26] C. Møller and M. S. Plesset. *Phys. Rev.*, 46:618–622, 1934.

[27] W. Meyer. *Modern theoretical chemistry*, volume 3. Plenum, New York, 1977.

[28] P.E.M. Sieg. *Int. J. Quantum. Chem.*, 18:1229, 1980.

[29] M. Pastore, C. Angeli, and R. Cimiraglia. *Chem. Phys. Lett.*, 422:522, 2006.

[30] M. Pastore, C. Angeli, and R. Cimiraglia. *Chem. Phys. Lett.*, 426:445, 2006.

[31] M. Pastore, C. Angeli, and R. Cimiraglia. *Theor. Chem. Acc.*, 118:35, 2007.

[32] N. Forsberg and P. Malmqvist. *Chem. Phys. Lett.*, 274:196, 1997.

[33] C. Bloch. *Nucl. Phys.*, 6:329, 1958.

[34] B.H. Brandow. *Rev. Mod. Phys.*, 39:771, 1967.

[35] I. Lindgren. *J. Phys. B*, 7:2441, 1974.

[36] A.Zaitsevskii and J.-P. Malrieu. *Chem. Phys. Lett.*, 223:597, 1995.

[37] J. des Cloizeaux. *Nucl. Phys.*, 20:321, 1960.

[38] H.-J. Werner. *Mol. Phys.*, 89:645, 1996.

[39] C. Angeli, C. J. Calzado, R. Cimiraglia, and J.-P. Malrieu. *J. Chem. Phys.*, 124:234109, 2006.

[40] C. Angeli, A. Cavallini, and R. Cimiraglia. *J. Chem. Phys.*, 127:074306, 2007.

[41] C. Angeli, A. Cavallini, and R. Cimiraglia. *J. Chem. Phys.*, 128:244319, 2008.

[42] M. Pastore, W. Helal, C. Angeli, R. Cimiraglia, S. Evangelisti, T. Leninger, D. Maynau, and J. P. Malrieu. *J. Chem. Phys.*, 128:174102, 2008.

[43] M. Pastore, W. Helal, C. Angeli, S. Evangelisti, T. Leninger, and R. Cimiraglia. *J. Mol. Struct. (THEOCHEM)*, in press, 2008.

[44] C. Angeli. *J. Comp. Chem.*, in press, 2008.

[45] B. Fuchssteiner and W. Oevel. Mupad version 2.5.3 for linux. Mupad research group, University of Paderborn. http://www.mupad.de.

[46] C. Angeli and R.Cimiraglia. *Comp. Phys. Com.*, 166:53, 2005.

[47] C. Angeli and R.Cimiraglia. *Comp. Phys. Com.*, 171:63, 2005.

[48] H.-J. Werner and P. J. Knowles. *J. Chem. Phys.*, 89:5803–5814, 1988.

[49] J. Olsen, P. Jørgensen, H. Koch, and A. Balkova. *J. Chem. Phys.*, 104:8007, 1996.

[50] L. M. Abrams and C. D. Sherril. *J. Chem. Phys.*, 121:9211, 2004.

[51] C. D. Sherril and P. Piecuch. *J. Chem. Phys.*, 122:124104, 2005.

[52] A. G. Taube and R. J. Bartlett. *J. Chem. Phys.*, 128:044110, 2008.

[53] U. S. Mahapatra, S. Chattopadhyay, and R. K. Chaudhuri. *J. Chem. Phys.*, 129:024108, 2008.

[54] A. Van Orden and R. J. Saykally. *Chem. Rev.*, 98:2313, 1998.

[55] J. W. Hehre, R. Ditchfield, and J. A. Pople. *J. Chem. Phys.*, 56:2257, 1972.

[56] *MOLPRO is a package of ab initio programs written by* H.J. Werner, P.J. Knowles with contribution from Almlöf, R.D. Amos, A. Berning, M.J.O. Deegan, F. Eckert, S.T. Elbert, C. Hampel, R. Lindh, W. Meyer, A. Nicklass, K. Peterson, A.J. Stone R. Pitzer, P.R. Taylor, M.E. Mura, P. Pulay, M. Schütz, H. Stoll, T. Thorsteinsson, and D.L. Cooper. Molpro2008.2, 2008.

[57] K.P. Huber and G. Herzberg. *Constants of diatomic molecules.* Van Nostrand Reinhold, New York, 1979.

[58] L. M. Abrams and C. D. Sherril. *J. Chem. Phys.*, 118:1604, 2003.

[59] Y. Luo, C. K. Wang, and Y. Fu. *Phys. Lett. A*, 326:412, 200 4.

[60] P. O. Astrand, P. Sommer-Larsen, S. Hvilsted, P. S. Ramanujam, and K. L. Bak S. P. A. Sauer. *Chem. Phys. Lett.*, 325:115, 2000.

[61] R. Pariser and G. Parr. *J. Chem. Phys.*, 49:1375, 1953.

[62] J. A. Pople. *Trans. Faraday Soc.*, 49:1375.

[63] J. Koutecky. *J. Chem. Phys.*, 44:3702, 1966.

[64] J. Cizek, J. Paldus, and I. Hubac. *Intern. J. Quantum Chem.*, 70:5414, 1974.

[65] L. Serrano-Andrés, M. Merchán, I. Nebot-Gill, B. O. Roos, and M. Fülscher. *J. Am. Chem. Soc.*, 115:6184, 1993.

[66] P.-Å. Malmqvist, A. Rendell, , and B. O. Roos. *J. Phys. Chem.*, 94:5477, 1990.

[67] M. H. Palmer, I. C. Walker, and M. F. Guest. *Chem. Phys.*, 241:275, 1999.

[68] L. Nygaard, J. T. Nielsen, J. Kirchheiner, G. Maltesen, J. Rastrup-Andersen, and G. O. Sørensen. *J. Mol. Struct.*, 3:491, 1969.

[69] F. Mata, M. C. Martin, and G. O. Sorensen. *J. Mol. Struct.*, 48:157, 1978.

[70] B. Bak, D. Christensen, L. Hansen-Nygaard, and J. Rastrup-Anderson. *J. Mol. Spectr.*, 7:58, 1961.

[71] E.R. Davidson and A. A. Jarzecki. *Chem. Phys. Lett.*, 285:155.

[72] P.-O. Widmark, P.Å. Malmqvist, and B. O. Roos. *Theor. Chim. Acta*, 77:291–306, 1990.

[73] L. Serrano-Andrés, M. Merchán, I. Nebot-Gill, R. Lindh, and B. O. Roos. *J. Chem. Phys.*, 98:3151, 1993.

[74] B. O. Roos, K. Anderson, M .P. Fülsher, P. Å. Malmqvist, L. Serrano-Andrés, K. Pierloot, and M. Merchán. *Advances in Chemical Physics: New Methods in Computational Quantum Mechanics*, volume XCIII. Wiley & Sons, New York, 1996.

[75] K. Kaufmann, W. Baumeister, and M. Jungen. *J. Phys. B: At. Mol. Opt. Phys.*, 22:2223, 1989.

[76] *MOLCAS is a package of ab initio programs written by* M. Andersson, A. Barysz, M. Bernhardsson, R .A. Blomberg, D. L. Cooper, M. P. Fülscher, C. de Graaf, B. A. Hess, G. Karlström, R. Lindh, P.-Å. Malmqvist, T. Nakajima, P. Neogrády, J. Olsen, B. O. Roos, B. Schimmelpfennig, M. Schütz, L. Seijo, L. Serrano-Andrés, P. E. M. Siegbahn, J. Stålringand T. Thorsteinsson, V. Veryazov, and P.-O. Widmark. Molcas5.4, 2002.

[77] P. J. Derrick, L. Asbring, O. Edqvist, B. O. Jonsson, and E. Lindholm. *Int. J. Mass. Spectrom. Ion. Phys.*, 6:161, 1971.

[78] M. H. Palmer, I. C. Walker, and M. F.Guest. *Chem. Phys.*, 238:179, 1998.

[79] B. O. Roos, P. Å. Malmqvist, V. Molina, L. Serrano-Andrés, and M. Merchán. *J. Chem. Phys.*, 116:7526, 2002.

[80] A. B. Trofimov and J. Schirmer. *Chem. Phys.*, 214:153, 1997.

[81] J. Wan, J. Meller, M. Hada, M. Ehara, and H. Nakatsuji. *J. Chem. Phys.*, 113:7853, 2000.

[82] H. Nakatsuji, O. Kitao, and T. Yonezawa. *J. Chem. Phys.*, 83:723, 1985.

[83] O. Christiansen, J. Gauss, J. F. Stanton, and P. Jørgensen. *J. Chem. Phys.*, 111:525, 1999.

[84] R. Burcl, R. D. Amos, and N. C. Handy. *Chem. Phys. Lett.*, 355:8, 2002.

[85] P. Celani and H.-J. Werner. *J. Chem. Phys.*, 119:5044, 2003.

[86] M. H. Palmer and P. J. Wilson. *Mol. Phys.*, 101:2391, 2003.

[87] T. Hashimoto, H. Nakano, and K.Hirao. *J. Chem. Phys.*, 104:6244, 1996.

[88] S. Z. Menczel. *Phys. Chem.*, 125:161, 1927.

[89] G. Scheibe and H. Z. Grieneisen. *Phys. Chem.*, B25:52, 1934.

[90] J. R. Platt. *J. Chem. Phys.*, 19:101, 1951.

[91] P. A. Mullen and M. K. Orloff. *J. Chem. Phys.*, 51:2276, 1969.

[92] M. B. Robin. *Higher Excited States in Polyatomic Molecules*, volume 2. Academic Press, New York, 1975.

[93] M. Bavia, F. Bertinelli, C. Taliani, and C. Zauli. *Mol. Phys.*, 31:479, 1976.

[94] E. H. Van Veen. *Chem. Phys. Lett.*, 41:535, 1976.

[95] W. M. Flicker, O. A. Mosher, and A. Kuppermann. *J. Chem. Phys.*, 64:1315, 1976.

[96] C. D. Cooper, A. D. Williamson, J. C. Miller, and R. N. Compton. *J. Chem. Phys.*, 73:1527, 1980.

[97] H.-H. Perkampus and T. H. Braunschweig. *UV-VIS Atlas of Organic Compounds*, page 740. VCH, Weinheim, 1992.

[98] W. C. Price and D. Walsh. *Proc. R. Soc. London, Ser. A*, 179:201, 1941.

[99] L. W. Pickett, N. J. Hoeflich, and T. C. Liu. *J. Am. Chem. Soc.*, 73:4865, 1951.

[100] K. Watanabe and T. Nakyama. *J. Chem. Phys*, 29:48, 1958.

[101] J. L. Roebber, D. P. Gerrity, R. Hemley, and V. Vaida. *Chem. Phys. Lett.*, 75:104, 1980.

[102] M. B. Robin. *Higher Excited States in Polyatomic Molecules*, volume 2. Academic Press, New York, 1985.

[103] M. H. Palmer, I. C. Walker, C. C. Ballard, and M. F. Guest. *Chem. Phys.*, 192:111, 1995.

[104] L. Nyulaszi. *J. Mol. Struct.*, 273:133, 1992.

[105] H. Nakano, T. Tsuneda, T. Hashimoto, and K. Hirao. *J. Chem. Phys.*, 104:2312, 1996.

[106] A. B. Trofimov and J. Schirmer. *Chem. Phys.*, 224:175, 1997.

[107] O. Christiansen and P. Jørgensen. *J. Chem. Am. Soc.*, 120:3423, 1998.

[108] E. V. Gromov, A. B. Trofimov, M. N. Vitkovskaya, J. Schirmer, and H. Köppel. *J. Chem. Phys.*, 119:737, 2003.

[109] E. V. Gromov, A. B. Trofimov, M. N. Vitkovskaya, H. Köppel, J. Schirmer, H.-D. Meyer, and L. S. Cederbaum. *J. Chem. Phys.*, 121:4585, 2004.

[110] O. Christiansen, H. Koch, and P. Jørgensen. *Chem. Phys. Lett.*, 243:409, 1995.

[111] O. Christiansen, P. Jørgensen, and C. Hättig. *Int. J. Quantum Chem.*, 68:1, 1998.

[112] Dalton, a molecular electronic structure program, Release 2.0, 2005. see http://www.kjemi.uio.no/software/dalton/dalton.html.

[113] P.-Å. Malmqvist and B. O. Roos. *Chem. Phys. Lett.*, 155:189, 1989.

[114] G. L. Bendazzoli, F. Bertinelli, P. Palmieri, A. Brillante, and C. Taliani. *J. Chem. Phys.*, 69:5077, 1978.

[115] L. Serrano-Andrés, M. Mercán, B. O. Roos, and M. Fülscher. *Chem. Phys. Lett.*, 211:125, 1993.

[116] J. Wan, M. Hada, M. Ehara, and H. Nakatsuji. *J. Chem. Phys.*, 114:842, 2001.

[117] D. J. Tozer, R. D. Amos, N. C. Handy, B. O. Roos, and L. Serrano-Andrés. *Mol. Phys.*, 97:859, 1999.

[118] H. Köppel, E. V. Gromov, and A. B. Trofimov. *Chem. Phys.*, 304:35, 2004.

[119] K. Tanaka, T. Nomura, T. Noro, H. Tatewaki, T. Takada, H. Kashiwagi, F. Sasaki, and K. Ohno. *J. Chem. Phys.*, 67:5738, 1977.

[120] W. Butscher and K.-H. Thunemann. *Chem. Phys. Lett.*, 57:224, 1978.

[121] K.-H. Thunemann, R. J. Buenker, and W. Butscher. *J. Chem. Phys.*, 47:313, 1993.

[122] D. C. Rawlings and E. R. Davidson. *Chem. Phys. Lett.*, 98:424, 1983.

[123] L. Nyulaszi and T. Veszpremi. *J. Mol. Struct.*, 140:353, 1986.

[124] L. Nyulaszi and T. Veszpremi. *J. Mol. Struct.*, 140:253, 1986.

[125] L. Nyulaszi and T. Veszpremi. *Chemica Scripta*, 28:331, 1988.

[126] R. Håkansson, B. Norden, and E. N. Thulstrup. *Chem. Phys. Lett.*, 50:305, 1977.

[127] B. Norden, R. Håkansson, P. B. Pedersen, and E. N. Thulstrup. *Chem. Phys.*, 33:355, 1978.

[128] N. Igarashi, A. Tajiri, and M. Hatano. *Bull. Chem. Soc. Jpn.*, 54:1511, 1981.

[129] G. Di Lonardo, G. Galloni, A. Trombetti, and C. Zauli. *J. Chem. Soc. Faraday Trans. II*, 69:2009, 1972.

[130] W. M. Flicker, O. A. Mosher, and A. Kuppermann. *Chem. Phys. Lett.*, 38:489, 1976.

[131] D. Dolphin. *The Porphyrins*, volume 1-7, page 740. Academic, New York, 1978-1979.

[132] B. Minaev and H. Ågren. *Chem. Phys.*, 315:215, 2005.

[133] J. Hasegawa, K. Takata, T. Miyahara, S. Neya, M. J. Frisch, and H. Nakatsuji. *J. Phys. Chem. A*, 109:3187, 2005.

[134] H. Nakatsuji, J.-Y. Hasegawa, and M. Hada. *J. Chem. Phys.*, 104:2321, 1996.

[135] Y. Tokita, J.-Y. Hasegawa, and H. Nakatsuji. *J. Phys. Chem. A*, 102:1843, 1998.

[136] O. Kitao, H. Ushiyama, and N. Miura. *J. Chem. Phys.*, 110:2936, 1999.

[137] M. Nooijen and R. J. Bartlett. *J. Chem. Phys.*, 107:6812, 1997.

[138] S. R. Gwaltney and R. J. Bartlett. *J. Chem. Phys.*, 108:6790, 1998.

[139] L. Serrano-Andrés, M. Merchán, M. Rubio, and B. O. Roos. *Chem. Phys. Lett*, 295:195, 1998.

[140] P.Celani and H.-J. Werner. *J. Chem. Phys.*, 112:5546, 2000.

[141] T. Hashimoto, E. Choe, H. Nakano, and K. Hirao. *J. Phys. Chem. A*, 103:1894, 1999.

[142] R. Bauernschmitt and R. Ahlrichs. *Chem. Phys. Lett.*, 256:454, 1996.

[143] R. Stratmann, G. Scuseria, and M. Frisch. *J. Chem. Phys.*, 109:8218, 1998.

[144] S. van Gisbergen, A. Rosa, G. Ricciardi, and E. Baerends. *J. Chem. Phys.*, 111:2499, 1999.

[145] D. Sundholm. *Phys. Chem. Chem. Phys.*, 2:2275, 2000.

[146] C. Rimington, S. F. Mason, and O. Kennard. *Spectrochim. Acta*, 12:65, 1958.

[147] B. G. Anex and R. S. Umans. *J. Am. Chem. Soc*, 86:5026, 1964.

[148] L. Edwards, D. H Dolphin, M. Gouterman, and A. D. Adler. *J. Mol. Spectrosc.*, 38:16, 1971.

[149] M. Gouterman. *J. Chem. Phys.*, 30:1139, 1959.

[150] M. Gouterman, G. Wagnière, and L. C. Snyder. *J. Mol. Spectrosc.*, 11:108, 1963.

[151] C. Weiss, H. Kobayashi, and M. Gouterman. *J. Mol. Spectrosc.*, 16:415, 1965.

[152] J. Almöf, T. H. Fischer, P. G. Gassman, A. Gosh, and M. Häser. *J. Phys. Chem.*, 97:10964, 1993.

[153] M. Merchán, E. Orti, and B. O. Roos. *Chem. Phys. Lett.*, 221:136, 1994.

[154] B. F. Kim and J. Bohandy. *J. Mol. Spectrosc.*, 73:332, 1978.

[155] U. Nagashima, T. Takada, and K. Ohono. *J. Chem. Phys.*, 85:4524, 1986.

[156] M. Merchán, E. Orti, and B. O. Roos. *Chem. Phys. Lett.*, 226:27, 1994.

[157] Abbas Farazdel, Michel Dupuis, Enrico Clementi, and Ari Aviram. *J. Am. Chem. Soc.*, 112:4206–4214, 1990.

[158] W. Helal, S. Evangelisti, T. Leninger, and D. Maynau. *J. Comp. Chem.*, page DOI 10.1002/jcc20982.

[159] C. Creutz. *Progr. Inorg. Chem.*, 30:1–73, 1983.

[160] N. Sutin. *Progr. Inorg. Chem.*, 30:441–498, 1983.

[161] R. J. Crutchley. *Adv. Inorg. Chem.*, 41:273–325, 1994.

[162] P. F. Barbara, T. J. Meyer, and M. A. Ratner. *J. Phys. Chem.*, 100:13148–13168, 1996.

[163] S. F. Nelsen, R. F. Ismagilov, and D. A. Trieber. *Science*, 278:846–849, 1997.

[164] J.-P. Launay. *Chem. Soc. Rev.*, 30:386–397, 2001.

[165] C. Creutz and H. Taube. *J. Am. Chem. Soc.*, 91:3988–3989, 1969.

[166] C. Joachim, J. K. Jimzewski, and A. Aviram. *Nature*, 408:541, 2000.

[167] C. Lambert and G. Nöll. *J. Am. Chem. Soc.*, 121:8434–8442, 1999.

[168] M. Robin and P. Day. *Adv. Inorg. Chem. Radiochem.*, 10:247, 1967.

[169] N. S. Hush. *Prog. Inorg. Chem.*, 8:391–444, 1967.

[170] N. S. Hush. *Coord. Chem. Rev.*, 64:135–157, 1985.

[171] B. S. Brunschwig, C. Creutz, and N. Sutin. *Chem. Soc. Rev.*, 31:168–184, 2002.

[172] V. Coropceanu, N. E. Gruhn, S. Barlow, C. Lambert, T. G. Bill J. C. Durivage, G. Nöll, S. R. Marder, and J.-L Brédas. *J. Am. Chem. Soc.*, 126:2727–2731, 2004.

[173] Deanna M. D'Alessandro and F. Richard Keene. *Chem. Soc. Rev.*, 35:424–440, 2006.

[174] M. D. Newton. *Chem. Rev.*, 91:767–792, 1991.

[175] J. F. Sanz and J.-P. Malrieu. *J. Phys. Chem.*, 97:99–106, 1992.

[176] Javier Fernández Sanz, Carmen Jiménez Calzado, and Antonio Márquez. *Int. J. Quantum Chem.*, 76:458–463, 2000.

[177] D. Dehareng, G. Dive, and A. Moradpour. *Int. J. Quantum Chem.*, 76:552–573, 2000.

[178] M. Malagoli and J. L. Brédas. *Chem. Phys. Lett.*, 327:13–17, 2000.

[179] R. C. Johnson and J. P. Hupp. *J. Am. Chem. Soc.*, 123:2053–2057, 2001.

[180] V. Coropceanu, M. Malagoli, J. M. André, and J. L. Brédas. *J. Chem. Phys.*, 115:10409–10416, 2001.

[181] V. Coropceanu, M. Malagoli, J. M. André, and J. L. Brédas. *J. Am. Chem. Soc.*, 124:10519–1053, 2002.

[182] C. Lambert and G. Nöll. *Chem. Eur. J.*, 8:3467, 2002.

[183] C. Lambert, S. Amthor, and J. Schelter. *J. Chem. Phys. A*, 108:6474–6486, 2004.

[184] A. V. Szeghalmi, M. Erdmann, V. Engel, M. Schmitt, S. Amthor, V. Kriegisch, G. Nöll, R. Stahl, C. Lambert, D. Leusser, D. Stalke, M. Zabel, and J. Popp. *J. Am. Chem. Soc.*, 126:7834–7845, 2004.

[185] S. F. Nelsen, A. E. Kondradsson, and J. P. Telo. *J. Am. Chem. Soc.*, 127:920–925, 2005.

[186] W. Helal, B. Bories, S. Evangelisti, T. Leninger, and D. Maynau. *Lect. Notes Comp. Sci.*, 3980:744, 2006.

[187] C. Calzado and J.-P. Malrieu. *Chem. Phys. Lett.*, 317:404–413, 2000.

[188] B. Huronand, J.-P. Malrieu, and P. Rancurel. *J. Chem. Phys.*, 317:404, 1973.

[189] C. Angeli, R. Cimiraglia, and J.-P. Malrieu. *Chem. Phys. Lett.*, 317:462, 2000.